New Nanomaterials for Photovoltaic Applications: A Study on the Chemistry and Photophysics of II-VI Semiconductor Nanostructures

Author: Chad Johnathan Dooley

Boston College

The Graduate School of Arts and Sciences

Department of Chemistry

NEW NANOMATERIALS FOR PHOTOVOLTAIC APPLICATIONS: A STUDY ON THE CHEMISTRY AND PHOTOPHYSICS OF II-VI SEMICONDUCTOR NANOSTRUCTURES

a dissertation by

CHAD J DOOLEY

Advisor: Prof. Torsten Fiebig

Submitted in partial fulfillment of the requirements

for the degree of

Doctor of Philosophy

May 2009

NEW NANOMATERIALS FOR PHOTOVOLTAIC APPLICATIONS: A STUDY ON THE CHEMISTRY AND PHOTOPHYSICS OF II-VI SEMICONDUCTOR NANOSTRUCTURES

by

Chad J Dooley

Advisor: Prof. Torsten Fiebig

Abstract:

This dissertation examines the chemistry and photophysics of semiconductor quantum dots with the intent of studying their capabilities and limitations as they pertain to photovoltaic technologies. Specifically, experiments are presented detailing the first time-resolved measurements of electron transfer in electronically coupled quantum rods. Electron transfer from the conduction band of CdTe was measured to occur on the 400 fs timescale (k_{ET} = 2.5 x 10^{12} s^{-1}), more than 500x faster than previously believed. Additionally, the direct optical promotion of an electron from the valence band of CdTe was observed, occurring on the timescale of the pump pulse (~50 fs). Based on the determined injection rates, a carrier separation efficiency of > 90% has been calculated suggesting these materials are sufficient for use in solar energy capture applications where efficient carrier separation is critical. To this end, model photovoltaic cells were fabricated, and their power conversion efficiency and photon-to-current generation efficiency characterized. In devices based of CdSe and heteromaterial quantum rods we

observed fill-factors on the order of 10-20% though with power conversion efficiencies of < 0.02%. It was discovered that using a high temperature annealing step, while critical to get electrochemically stable photoelectrodes, was detrimental to quantum confinement effects and likely removed any hQR specific capabilities.

Additionally, a detailed study on the role of nucleotide triphosphate chemistry in stabilizing emissive CdS nanoparticles is presented. Specifically it was observed that in a neutral pH environment, GTP selectively stabilizes CdS quantum dots with diameters of ~4 nm while the other naturally occurring ribonucleotides do not yield emissive product. The selectivity is dependent on the presence of the nucleophilic N-7 electrons near a triphosphate pocket for Cd^{2+} complexation as well as an exocyclic amine to stabilize the resulting product particles. However, in an elevated pH environment, the nucleobase specificity is relaxed and all NTPs yield photo-emissive quantum dots with PLQEs as high as 10%.

Acknowledgements

The work presented in this dissertation is only possible because of the efforts and help of a number of people.

Firstly, my advisors Torsten Fiebig and Shana Kelley deserve special recognition for all their work and efforts on my behalf, especially for the many conversations, inspirations and council. Torsten I am especially grateful to, for listening to my ideas, being keen on considering new directions, for always being free to offer suggestions and being full of insight on how to consider a problem from another point of view.

My efforts into characterizing photovoltaic cells, while only a small section of this dissertation were some of the most meaningful studies and important to wrapping up some of the thoughts on the materials I have studied. This work would not have been successful without help from Prof. Dunwei Wang and his group who I have enjoyed working with and getting to know since he joined BC faculty a couple years ago. They are a great group and I am grateful for the many helpful conversations I have had with Stafford and Yongjin specifically.

The other members of the Fiebig group have made the work presented in Chapter 3 possible. To Stoichko specifically I am grateful for working with me closely over the past 3 years on this work. He was instrumental in our analysis of the charge separation dynamics experiments. Perhaps more importantly, I am grateful that Stoihcko has become such a close friend. I am thankful to Anton for his willingness to share his laser expertise over the last 3 years. He was very patient and always willing to take the time to

teach me the most fundamental components of an experiment. Such attention to detail is a quality I admire when it comes to teaching.

Lastly, and perhaps most importantly, I want to note the efforts and strength offered by my friends and family as I have spent the better part of 5 years on this work. I am grateful to my family for their constant encouragement and curiosity in the work that I do. I am especially thankful for my great grandmother, Ellen Keyes, with whom I am fortunate to be able to share the completion of this dissertation. It is an understatement to say that she has been the center and strength of our family, and I will be forever grateful for her support and her love. The rest of my friends and family all deserve special recognition but would it would take a separate document to sufficiently express my gratitude. Therefore, to the new friends I have made in graduate school, and to the old friends and family who have been there to support me as I have grown, Thank You.

Table of Contents

Table of Figures

Table of Tables

List of Abbreviations

ATP	adenosine triphosphate
BBO	ß-Barium Borate
CB	conduction band
CCD	charge-coupled device
CS	carrier separation
CT	charge transfer
CTP	cytidine triphosphate
DCC	N,N'-dicyclohexylcarbodiimide
DFG	difference-frequency generation
DIC	N,N'-diisopropylcarbodiimide
EDC	1-ethyl-3(3-dimethylaminopropyl) carbodiimide
EDS	Energy dispersive x-ray spectroscopy
FF	fill-factor
FRET	Förster resonance energy transfer
fs	femtosecond
FWHM	full-width at half maximum
G	guanine

GSH	glutathione
GTP	guanosine triphosphate
hNR	heteromaterial nanorod
HOMO	highest occupied molecular orbital
HR-TEM	high-resolution transmission electron microscope
IR	infrared
ITP	inosine triphosphate
LUMO	lowest unoccupied molecular orbital
MEA	ß-mercaptoethylamine
MPA	mercaptopropionic acid
NIR	near-infrared
NOPA	non-collinear optical parametric amplifier
ns	nanosecond
NTP	nucleotide triphosphate
OD	optical density
OPA	optical parametric amplifier
OPO	optical parametric oscillator
PLQE	photoluminescence quantum efficiency
ps	picosecond
QD	quantum dot

QR	quantum rod
SEM	scanning electron microscope
SFG	sum-frequency generation
SHG	second harmonic generation
TEM	transmission electron microscope
TGA	thioglycolic acid
UTP	uridine triphosphate
VB	valence band
WLC	white-light continuum
XPM	cross-phase modulation

List of Publications

1. Hinds, S.; Taft, B. J.; Levina, L.; Sukhovatkin, V.; Dooley, C. J.; Roy, M. D.; MacNeil, D. D.; Sargent, E. H.; Kelley, S. O., Nucleotide-Directed Growth of Semiconductor Nanocrystals. *J. Am. Chem. Soc.* **2006,** *128* (1), 64-65.

2. Ma, N.; Dooley, C. J.; Kelley, S. O., RNA-Templated Semiconductor Nanocrystals. *J. Am. Chem. Soc.* **2006,** *128* (39), 12598-12599.

3. Dooley, C. J.; Rouge, J.; Ma, N.; Invernale, M.; Kelley, S. O., Nucleotide-stabilized cadmium sulfide nanoparticles. *J. Mater. Chem.* **2007,** *17* (17), 1687-1691.

4. Dooley, C. J.; Dimitrov, S. D.; Fiebig, T., Ultrafast Electron Transfer Dynamics in CdSe/CdTe Donor-Acceptor Nanorods. *J. Phys. Chem. C* **2008,** *112* (32), 12074-12076.

5. Dimitrov, S. D.; Dooley, C. J.; Trifonov, A. A.; Fiebig, T., Femtosecond Probing of Optical Phonon Dynamics in Quantum-Confined CdTe Nanocrystals. *J. Phys. Chem. C* **2009,** *113* (10), 4198-4201.

1 Introduction

Behind every complete piece of work is an interesting history and underlying motivation. The work that encompasses the experiments and data presented here is no different. The intention has been to study and explore a novel class of colloidal semiconductor materials in context of their use as a renewable energy platform. This chapter serves to introduce the motivation of solar energy conversion and how it pertains to semiconductor quantum dots. A more detailed discussion of the underlying motivation, including an examination of the projected global energy demand over the next 40 years and the capabilities of renewable energy to provide this energy is presented in the Appendix.

1.1 Solar energy harvesting

At 120,000 TW of accessible solar power incident on the surface of the earth at any given time, there is more than 8200 times the amount of energy available from the sun annually than is currently consumed. In fact, most all other forms of renewable energy, including biomass, wind, and hydroelectric, can all be considered solar based (exceptions are geothermal and tidal). Accordingly, the logical step would be to develop a way to collect that energy directly. Indeed this is where valuable research and development efforts have been directed for the last 40-50 years. Modern commercially available silicon photovoltaic cells can have a power conversion efficiency of ~15-20%, significantly better than biofuel production.[1] But they are still about 10 times more costly

than using fossil fuels per unit energy.[2] Therefore, in order to make direct solar energy capture a suitable power source for the modern economy, significant improvements need to be made, not only in efficiency, but also in the cost of production. It is this motivation that supports the work presented in this dissertation where quantum confined semiconductor materials, with novel and interesting optoelectronic properties, are studied and their capabilities for use in photovoltaic cells assessed.

Interest in semiconductor quantum dots for applications in solar cell applications has been extensive for the last 5-10 years as a result of their inherent bandgap energy tunability. With bandgaps that can be tuned through the entire solar spectrum, quantum dot based solar cells can potentially access the single-sun theoretical power conversion efficiency limit of 66% (i.e. an infinite layered multi-junction cell).[3] Current single bandgap solar cells have a theoretical limit of 31% which, assuming a solar radiation temperature of 6000 K, is obtainable with a bandgap of 1.1 eV, the same as silicon.[4] If the same relative yield is achieved with quantum dot based cells as with current silicon technology, that is 20%/31%, then maybe these devices will help to improve the overall cost of solar energy conversion through higher efficiency cells based on materials that are relatively inexpensive to produce compared with single crystal silicon devices.

To be complete in the analysis of solar energy's inherent capabilities, it is important to point out that the use of photovoltaic cells or solar-thermal generators is limited by the fact that solar energy is very diffuse and differs in intensity and availability depending on your location in the world, the season and time of day. For these reasons, even if direct solar energy capture is improved to the point where it is more than competitive with fossil fuels, nuclear, wind turbines, etcetera, a second problem becomes how to store and

transport this energy to move it from locations with excess sun and small populations to those with less sun light and dense populations. Thus, a complete global energy solution will also require research into the science of energy storage. Perhaps the most promising direction of attack on this problem is the catalytic splitting of water into molecular hydrogen and oxygen which when used as a fuel forms a closed loop and is capable of powering most modern technologies. Consistent with this observation, research into this component of the global problem is currently being heavily pursued by the scientific community.[5-18]

1.2 Introduction to quantum dots

1.2.1 Quantum confinement in semiconductors

Semiconductor quantum dots (QDs) have received considerable attention since the pioneering work of Louis Brus in the early 1980s.[19, 20] They continue to fascinate scientists from both theoretical and application driven fields as a result of size induced quantum confinement effects on exciton behavior. Specifically, the typical rainbow of emission profiles showing the tunability of the emission spectrum of CdSe or CdTe QDs have become familiar images throughout the field. Such a plot is shown below in Figure 1.1. The tunability is the result of the increased confinement of the exciton wavefunction by the surface of the crystal once the radius of the crystal is below the material's inherent Bohr exciton radius, a_0. In this sense, the particle behaves like a simple particle-in-a-box where the size of the particle constricts the carrier wavefunction.

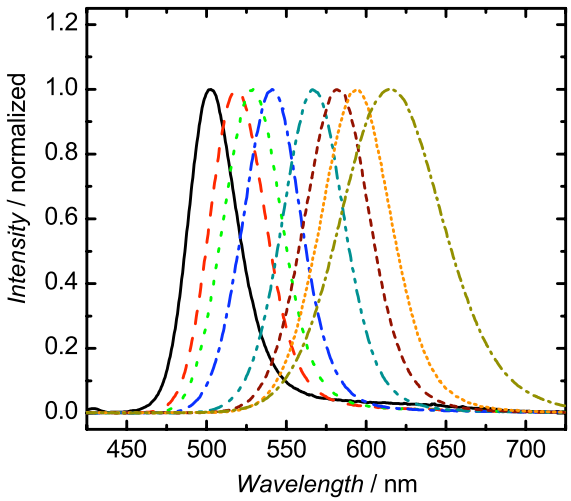

Figure 1.1: Emission spectra of aqueous soluble CdTe showing tunability from 490-640 nm for particles ranging in size from 2.64 to 4.1 nm.

Specifically, the confinement is the result of constraining the hydrogenic electron-hole wavefunction – an exciton – to a volume smaller than the radius of the bulk material wavefunction, which is dictated by the periodic potential of the lattice structure. This bulk radius of this Wannier exciton, defined as the Bohr exciton radius, can be calculated as:

$$a = a_0\left(m_e / M_{ex}\right)\left(\varepsilon/\varepsilon_0\right) = \frac{4\pi\varepsilon\hbar^2}{M_{ex}e_c^2} \tag{1.1}$$

where a_0 is the standard hydrogen Bohr radius (0.53 Å), e_c is the unit electric charge, ε is the semiconductor dielectric constant, and m_e is the free-electron mass. M_{ex} is the traditional exciton reduced mass, calculated for CdSe as:

$$M_{ex,CdSe} = \left(\frac{1}{m_{e,CdSe}} + \frac{1}{m_{h,CdSe}}\right)^{-1} \tag{1.2}$$

where $m_{h,CdSe}$ and $m_{e,CdSe}$ are the effective masses of the CdSe hole and electron respectively.

In an effort to understand the specific effects of spatial confinement of an exciton, Louis Brus worked out nearly 3 decades ago a simple correction to the bulk band gap of direct band gap semiconductors. Using a particle in a confined sphere approximation he found that[21, 22]

$$E_{g,QD} = E_{g,bulk} + \frac{\hbar^2\pi^2}{2r^2}\left(\frac{1}{m_e} + \frac{1}{m_h}\right) - \frac{1.8e^2}{\varepsilon \cdot r} + P(r) \qquad (1.3)$$

where *r* is the radius of the particle, $m_{e/h}$ is the electron/hole effective mass, ε is the semiconductor dielectric constant and $P(r)$ is a surface polarizability term. This last term is usually small and is neglected in the 1s-1s approximation.[22] The first term in equation 1.3 is simply the kinetic energy of the respective charge carriers while the second term is their coulombic interaction through the dielectric medium of the material. The simplicity of this correction along with the relative accuracy of the resulting predictions is illustrative of the ideality of the materials from a theoretical viewpoint.

In addition to the increase in the band gap, discrete band edge states emerge giving rise to defined optical transitions in the absorbance and emission spectra. This effect is illustrated below in Figure 1.2 showing the defined electron and hole states that emerge from quantum confinement of the carriers at a reduced size. Electron states usually show more confinement induced separation than holes as a result of having smaller effective masses (e.g. $m_{e,CdSe} \approx 0.1 \cdot m_{free\text{-}electron}$ while $m_{h,CdSe} \approx 0.9 \cdot m_{free\text{-}electron}$). Typically, electron states exhibit a gap on the order of 0.2-0.4 eV between the 1S(e) and 1P(e)

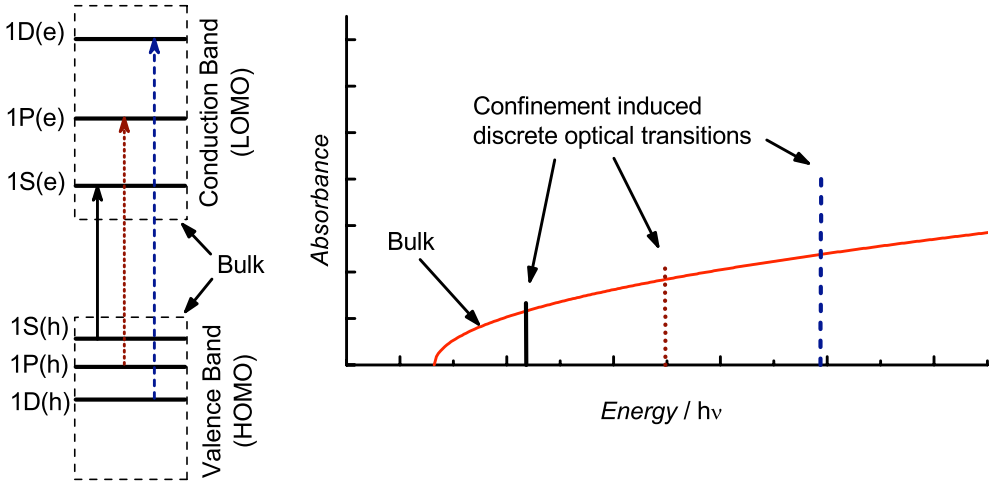

Figure 1.2: Energy level diagram and schematic of optical spectra showing the breakdown of the bulk material band structure to discrete electron and hole states as well as the resulting increase in the material's band gap. The energy level diagram neglects spin-orbit interactions in hole states.

states. The band edge hole states are additionally complicated by spin-orbit interactions (not shown in the diagram). Accounting for these interactions, the 1S, 1P and 1D states shown in the energy diagram are also split into a large number of different spin states with the $1S_{3/2}(h)$ being lowest in energy. As a result of the weakly split spin-orbitals and already closely spaced levels, the spin-orbit hole levels are very densely packed with energy differences on the order of 0.1 eV and smaller with substantial overlap between S and P states. Because of the relatively large effective masses and spin-orbit interaction, hole states can often be considered as a quasi-continuum of states.

A typical absorbance spectrum of an organic soluble CdSe is presented below showing well-defined absorbance bands from four transitions. The four bands are identified by the hole and electron states involved and are typically abbreviated according to the angular momentum quantum number of the participating hole state. For

example, the lowest energy transition, analogous to the HOMO-LUMO gap, between the $1S_{3/2}$(h) and 1S(e) levels is usually identified as the 1S transition. Likewise, the neighboring $2S_{3/2}$(h)-1S(e) transition is labeled as 2S. Using this nomenclature, the first four transitions in the optical spectra are the 1S, 2S, 1P and 3S transitions in succession. As a consequence of the strong dependence on the 1S transition on the radius (see equation 1.3), the absorption profile contains information on particle size as well as a rough indication of particle size distribution. For the sample shown, the narrow and symmetric 1S feature is indicative of a monodisperse sample, typically with variance in size of < 5%, and a diameter of 3.5 nm. The relative change in energy of the 2S, 1P,

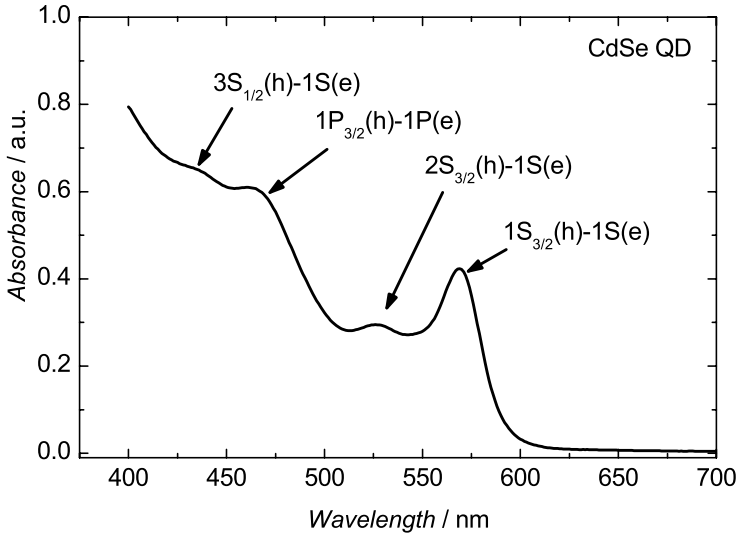

Figure 1.3: Absorbance spectrum of 3.5 nm CdSe QDs showing well-defined electron and hole states. The first four transitions – 1S, 2S, 1P and 3S – are identified by the 2 carriers created after photon absorption.

and other higher levels contributing to the absorbance profile all have different derivatives with respect to the particle radius and accordingly the absorbance lineshape will change with increasing or decreasing size.[23, 24]

1.2.2 Brief history of quantum dots

Research in the nanotechnology field has enjoyed extremely rapid growth over the last 30 years since work on semiconductor nanoparticles first began. A large number of reviews and perspectives have been written detailing some of the salient properties of semiconductor quantum dots as well as their applications to lasers, optoelectronics, and medicinal and biological chemistry.[22, 25-35] As quantum dots and nanoparticles are ported to many other research fields, it is beneficial to highlight some of the specific work published in a brief history as it pertains to optoelectronic applications and this dissertation.

Much of the early development in semiconductor quantum dots, specifically of direct bandgap metal chalcogenide materials, was done in the lab of Louis Brus at Bell Laboratories, who published the first paper on the size dependence of the reduction potentials for very small copolymer stabilized aqueous CdS crystallites.[20] The synthesis of these materials was reported earlier by Kalyanasundaram *et al.*[36, 37] but quantum confinement effects remained elusive until Brus' seminal work.

The aqueous materials, made throughout the 1980's by Brus and others, first identified as quantum dots by Bawendi in 1990,[22] were stabilized by weak binding copolymers. Because of these weak interactions, they suffered from stability problems from deleterious continued growth under ambient conditions,[38, 39] and inhomogeneous

broadening.[40] This limited the study and potential applications of the materials until 1993 when the high temperature organometallic synthesis of CdS, CdSe and CdTe was first reported by Murray and Bawendi.[41] When synthesized with ligands that strongly bind to the surface atoms of the crystals, such as long-chain alkylphosphine oxides and alkyl acids, the particles showed significantly improved shelf lives. Additionally, the high-temperature synthesis yielded monodisperse crystals allowing the size dependent properties to be studied more thoroughly. Provided with a suitable synthesis of stable particles showing high photoluminescence quantum efficiencies (PLQE) and a high degree of homogeneity, the nanoscience field embraced these materials and further developments have rapidly emerged.

In 1997 the first syntheses of core/shell heterostructures were published[42, 43] with CdSe/ZnS becoming the most popular material for photoemission applications as it showed significantly improved PLQEs, approaching efficiencies competitive to organic dyes typically used for cell labeling. In contrast to organic dyes, however, these materials were significantly (>100-fold) more photostable.[34] Additionally, aqueous syntheses of CdTe materials in water were dramatically improved by Weller with the use of thioglycolic acid as a stabilizing ligand.[44] The last major breakthrough in synthetic methodology was made in 2000 when Peng *et al.* reported that the pyrophoric and acutely toxic $Cd(Me)_2$ precursor used for organic syntheses could be replaced in most cases by CdO making the synthesis accessible to conventional Schlenk techniques.

With facile and reproducible synthetic methods for the preparation of semiconductor quantum dots, the report of more fundamental carrier behavior and applications have rapidly emerged. Klimov and others have studied the behavior of photogenerated

excitons on the femtosecond timescales elucidating the role of electron-hole coupling in rapid carrier thermalization.[45-47] Recently multiple exciton generation has been observed in CdSe quantum dots[48] as well as carrier multiplication in CdSe and PbSe nanocrystals,[49, 50] stirring increased interest in laser and photovoltaic cell applications. In the latter process, a single high energy photon is absorbed by the material and instead of a single high energy exciton forming followed by phonon assisted thermalization (i.e. internal conversion), a number of lower energy excitons are created. For example, if the incident photon is twice the band gap ($2 \cdot E_g$) of the material, two band edge excitons can be generated under certain conditions. Up to eight excitons have been reported from a single photon.[51, 52] Within the last year, some of these results have been called into question by the Bawendi group[53] but the effect is still receiving substantial investigation.

A number of other important findings have emerged from studies on these materials over the past decade but the ones highlighted above are some of the most important leading to the work presented in this dissertation as well as many other published works in the area. Below a basic timeline summarizes these events and the brief but full history of quantum dots over the past 30 years. This dissertation adds to the discussion by presenting our findings on carrier separation dynamics in heteromaterial quantum rods. These experiments were the first report of time-resolved studies capable of resolving the electron transfer event with sub-ps resolution.

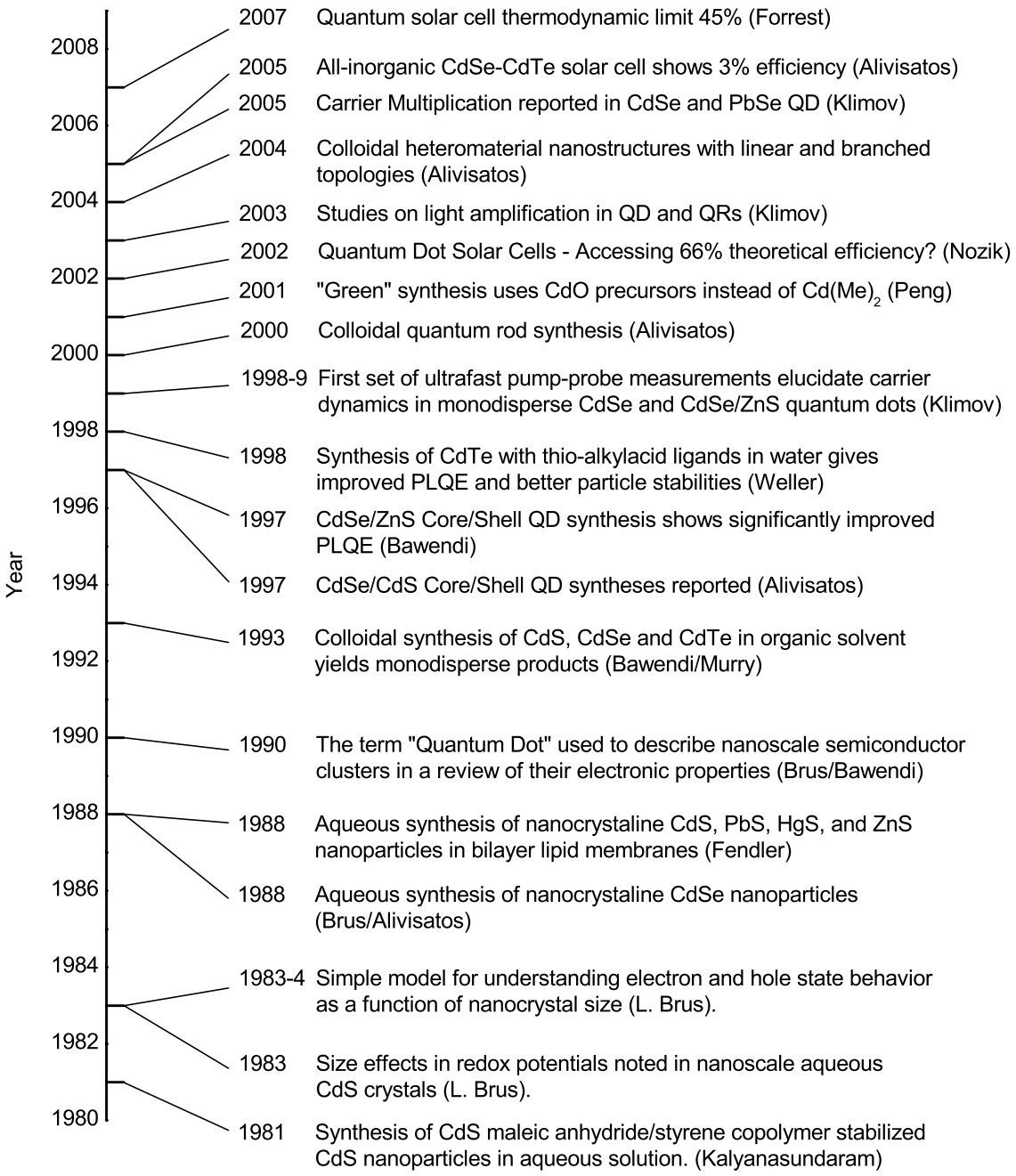

Figure 1.4: Timeline highlighting the history of quantum dots over the past 30 years showing some of the most important findings as they pertain to the work presented in this dissertation.[3, 19-22, 27, 37-47, 49-52, 54-59]

1.3 Charge carrier separation in quantum dots

Nanostructured semiconductor materials have been explored and discussed extensively in the scientific community as a new class of materials ideally suited for photonic applications yet no commercially viable devices have emerged. Photovoltaic devices based on direct band gap II-VI and IV-VI quantum dot (QD) and quantum rod (QR) materials specifically have received great attention.[3, 32, 60-64] Because of the ease of synthetic control over bandgap energies as a function of material geometries,[22] quantum rods are a stable photosensitizer that can easily be tuned for optimal power conversion efficiency over most of the solar spectrum.[3] Such control over band structure is expected to allow improvements to device efficiency beyond the 31% Shockley-Queisser theoretical limit for silicon technologies[3] and yet, to date, all reported devices based on quantum dots or quantum rods have power conversion efficiencies almost an order of magnitude below what is attainable from standard p-n junction technologies at less than 3%.[58, 65, 66] With such a vast discrepancy between theoretical efficiency limits and actually obtained efficiencies from so many devices, there are a large number of questions that need to be answered before any improvements are to be realized, many of which are practically important and others which are theoretically important.

To identify these questions, the operation of a PV can be broken down in to three basic steps. First is the generation of photocarriers by the photon absorption. Secondly, there needs to be a drift driven or diffusion driven charge carrier separation event where the hole and electron of the photocarrier are spatially separated. This process has a finite probability and must compete with many other energy redistribution pathways. Lastly, the separated charge carriers need to be transported away from the

photosensitive material and moved to working electrodes where they can be shuttled through a resistive load before recombining. Similar to the second step, the carrier transport process also has to compete with electron-hole recombination mechanisms. Presumably the failure to achieve efficient power conversion in quantum rod based devices can be explained by either poor carrier separation or/and carrier transport. Yet little is known about the specifics of the dynamics involved in such devices. By studying the last two steps, this dissertation sets out to discuss the fundamental capabilities and limitations of these proposed QR device motifs. Specifically, the carrier separation process is examined in detail using time-resolved spectroscopy offering new efficiency of the event as well as fundamental insights into the effects of quantum confinement and band structure control.

In order to effect charge separation, donor and acceptor materials need to be chosen such that their band structure have a specific alignment. Figure 1.5 introduces the energy layout of two interacting quantum rods with band energies chosen to align in a type-II structure. By having its band edge electron and hole states below the same

Figure 1.5: Schematic representation of the band edge energy structure of two interacting semiconductor quantum rods showing type-II band alignment. Following photoexcitation, an electron in CdTe can either (a) transfer to the conduction band of CdSe, which is lower in energy, or (b) relax back to the ground state.

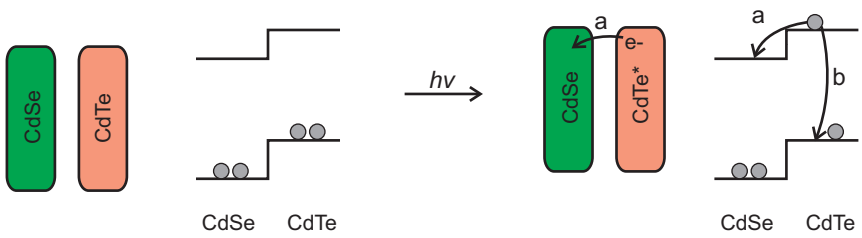

respective states in CdTe, CdSe is a suitable electron acceptor (and hole donor). If put in close enough proximity and if there is sufficient coupling between the two valence band states, then an electron will spontaneously transfer across the interface of the two materials, process (a) in Figure 1.5, following carrier generation. Perhaps not surprisingly, the chemistry joining the two materials at this junction therefore plays a critical role in the dynamics of charge separation. If there are organic ligands and solvent molecules at the interface, then a large reorganization energy is likely as well as potentially weak electronic coupling. In such a situation, electron transfer would be rather slow and have difficulty competing with other cooling pathways, process (b) in Figure 1.5. Conversely, if the two materials can be placed in atomically close proximity without surface ligands separating the materials, then charge separation should be very efficient. Indeed, the findings in Chapter 3 and the results we have recently published on the work[67] support these hypotheses.

As mentioned, the electron transfer event must also compete with charge carrier cooling in order to render the material suitable for photon energy conversion. In quantum confined structures with good photoemission, exciton recombination has a typical lifetime of more than 2 ns. This is the case for materials such as aqueous synthesized CdTe or traditional organic syntheses of CdSe. Organic pathways to CdTe quantum dots and rods, however, typically show very rapid exciton recombination, often as fast as 20 – 50 ps. In this case, the rate of charge separation has to be on the order of 50 ps or faster to give high separation efficiencies and render the material a viable candidate for photon energy conversion.

Ultrafast broadband pump-probe spectroscopy, the primary time-resolved technique used to characterize this process, is able to interrogate the electron and hole states of interest by probing the band edge absorbance features in the visible region. As such, the technique is ideal for studying the dynamics in such systems, which are expected to be on the ps timescale, and understanding their fundamental capabilities.

1.4 Ligand chemistry and additional applications

In addition to the time-resolved studies on heteromaterial quantum confined structures presented in Chapter 3, we have also studied the effects of less conventional ligand systems in stabilizing quantum dots. The motivation is to gain improved control over material processing and macro-particle structure fabrication. To this end, nucleic acids offer a unique ligand scaffold for nanoparticle growth as they posses a wide range of functional group chemistries that are suitable for binding to particle surfaces as well as that can be used for directing assembly into larger arrayed structures though sequence specific complexation.[68, 69] Additionally, one of the only currently marketed applications of quantum dots is for biological labeling and imaging.[34] Biological ligand stabilized quantum dots are ideally suited as biologically amenable structures that do not require extensive post synthesis processing or large bulky secondary ligand structures to render the particles soluble in aqueous environments.

Inorganic semiconductor nanoparticles are a promising material for the development of novel luminescent biological probes as they exhibit comparable quantum yields and a higher degree of spectral tunability than organic dyes typically used for biological labeling.[34] By choosing between different inorganic materials ranging from larger band-

gap II-VI materials such as ZnS, to smaller band gap IV-VI materials, such as PbS and PbSe, the photoemission from nanometer sized particles can be localized anywhere from the near ultra-violet to the near-infrared. The latter emission range is ideal for shallow tissue imaging in the near-infrared spectral region.[70-72]

Motivated by the potential uses for both biological imaging chemistries as well as directed macro-particle array assembly, we have examined the chemistry of nucleotide triphosphates (NTP) for stabilizing CdS nanoparticles. Chapter 4 highlights the findings of this work including our published findings on the pH dependence of nucleotide specific CdS stabilization.[73] Additionally, it details unpublished experiments done to optimize the synthetic procedure. The optimization followed our preliminary findings on the role of nucleic acid functional groups in stabilizing PbS quantum dots.[74]

2 Ultrafast broadband pump-probe spectroscopy

2.1 Introduction

Femtosecond broadband pump-probe spectroscopy is the critical experimental method used to characterize carrier dynamics in heteromaterial quantum rods in this dissertation. The details of the technique, as implemented in our lab, are described here. In addition, I have prepared a MATLAB analysis suite that is presented in the second half of this chapter. This toolset allows the data from pump-probe experiments to be easily processed and analyzed which has significantly aided the data exploration processes in contrast to previous suites written by past members of our group.

Compared to traditional two-color pump-probe spectroscopy, the broadband technique used for these experiments is more capable of resolving multiple states simultaneously. This is because a probe pulse covering a wide spectral range is used instead of a single wavelength to interrogate the sample at varying times after an excitation event. Secondly, as an important consequence of the “white-light” continuum (WLC) broadband probe pulse, not only does the technique allow the kinetics at multiple wavelengths to be measured and compared simultaneously but it also facilitates the study of complex spectral changes including spectral shifts, changes in lineshape and band width changes.[75] In a two-color experiment, such fine detail is not accessible.

In a broadband pump-probe spectrum a number of different bands are expected to be seen. Excited state absorption transitions, i.e. the transition from an excited state

(e.g. S_1) to a higher excited state (S_n) by a probe photon, are the most commonly characterized in traditional chromophores. Additionally, two other contributions may be observed depending on the probe range used. Negative signals may originate from stimulated emission transitions (from the same excited states as above), as well as ground state bleaching signals. Below, Figure 2.1 shows how a transient pump-probe spectrum might appear relative to the ground state absorption signal.

Semiconductor nanostructures have a slightly more complicated and dense band structure compared to organic molecules. Nanocrystals exhibit allowed optical transitions throughout the near-UV and visible spectrum. The transitions spread from the tunable band edge 1S transition, usually observed in the visible region, through to the UV for deeper hole states and higher electron states. The result is that transient absorption

Figure 2.1: Illustration showing expected transitions visible in a pump-probe spectrum (solid line). Ground state bleaching signals dominate in semiconductor quantum confined materials examined in this work.

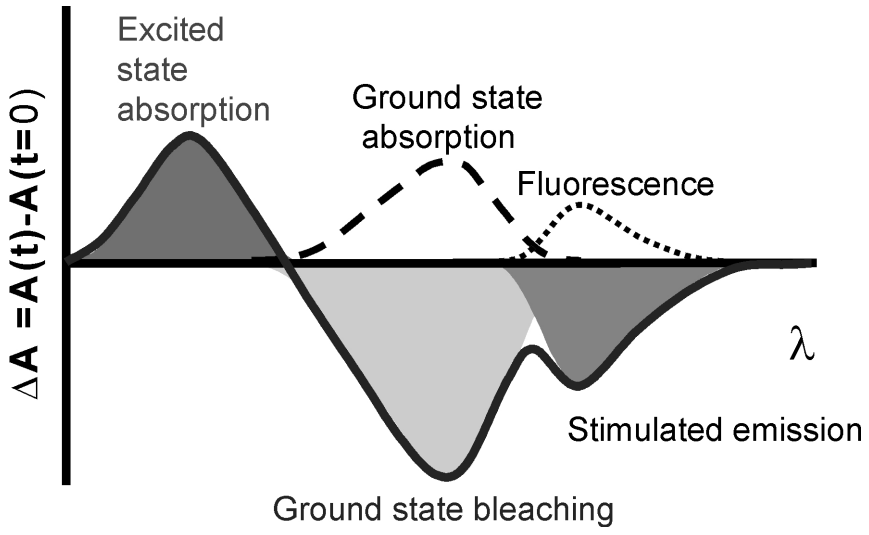

signals, following photoexcitation, are dominated by the bleaching of the ground state allowed optical transitions.

2.2 Experimental setup

A schematic representation of our experimental setup is presented below in Figure 2.2.[76] The experiment is powered by a CPA-2010 Clark-MXR Ti:Sapphire regenerative amplifier which provides a train of 150 fs 775 nm pulses at 1 kHz with a total power of ~1 W (~1 mJ per pulse). The output beam is divided using beam splitters to

Figure 2.2: Schematic representation of the broadband pump-probe experimental setup. The output of the NOPA is used as a pump pulse and is tunable from 470nm to 700nm with 30-45 fs pulses after compression. A "white" light probe pulse is generated by focusing the output pulse of the Ti:Sapphire laser into a CaF_2 crystal.

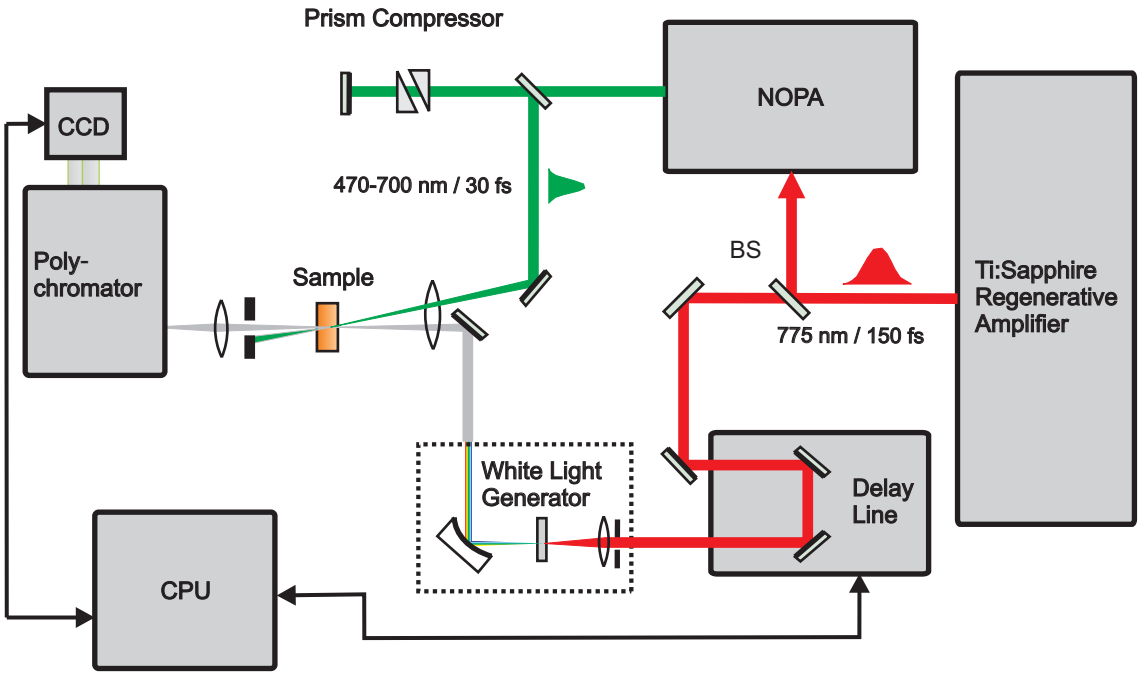

power the experiment, sending 250 mW to power the home built non-collinear optical parametric amplifier (NOPA) for pump pulse generation and 5 mW for white light generation using a rotating CaF_2 disk. Our NOPA is a dual stage non-collinear optical parametric amplifier capable of giving 10-15 µJ of output energy per pulse, tunable from 470-700 nm and compressible to 20-50 fs. Pump pluses beyond 700 into the NIR are also obtainable by either direct amplification of the very weak NIR component of the sapphire generated broadband seed pulse, or by using the idler output pulse, which can be extend to greater than 2000 nm. As a result of group velocity dispersion from the optics in the NOPA, a prism pair is required to compress the output pulse from >150 fs to 20-50 fs as measured by autocorrelation. For a pump-probe measurement, the

Figure 2.3: Detailed schematic of the two-stage non-collinear optical parametric amplifier (NOPA) used to generate a tunable pump pulse for our broadband pump-probe experiments. The NOPA can be tuned from ~470 nm to >2000 nm.

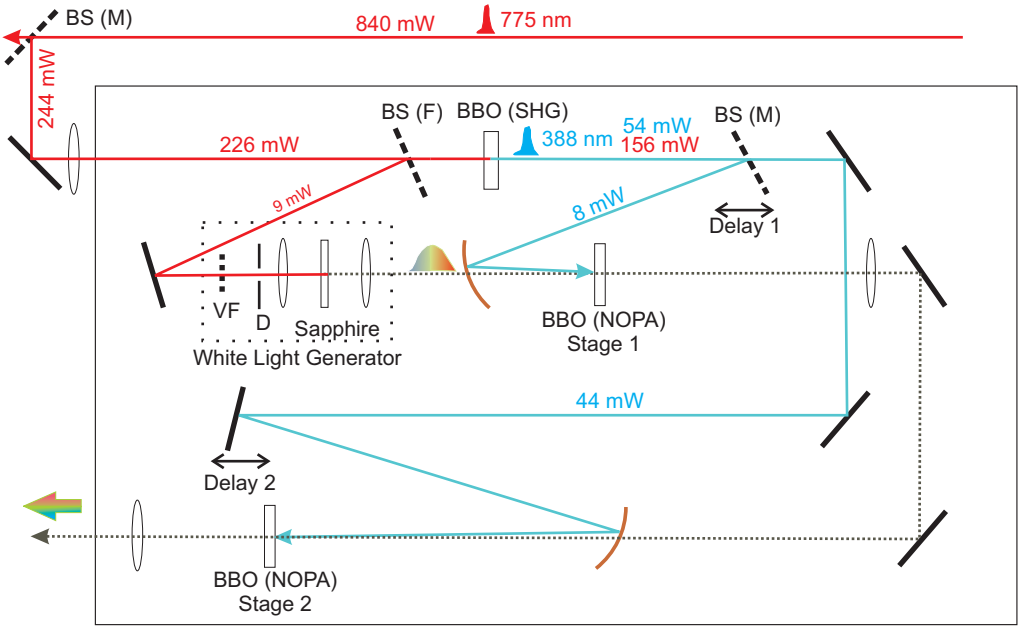

compressed pump pulse is then attenuated to the desired pump intensity using variable apertures and focused to 100-300 μm through the sample, off-angle to the white light probe pulse.

Traditionally in our lab we have used a second harmonic generation (SHG) stage to increase our pump pulse frequency into the near-UV. This can be accomplished by focusing the compressed output from the NOPA into a 100 μm ß-Barium Borate (BBO) type-I phase-matching crystal. This allows us to access pump wavelengths in the 240-400 nm range without much additional work. Furthermore, the SHG efficiency is highly sensitive to the pump flux, increasing in efficiency and therefore intensity with shorter input pulse lengths. Consequently, monitoring the intensity of the SHG signal allows a facile method to optimize pump pulse compression without needing to align the autocorrelator.

The WLC probe pulse is generated by tightly focusing a small fraction of the laser output into a 3 mm CaF_2 plate. Care must be taken that the disk is rotating, or otherwise moving, as the highly focused input pulse can easily damage the crystal under continuous exposure. The output of the crystal is dependent on the frequency of the input pulse and can range from ~350 to 750 nm when pumped by the 775 nm output of our commercial laser. The range can be moved to the UV or further into the IR by moving the pulse further to the blue or red respectively (see discussion about Figure 2.4 below). For measuring the transient absorption spectrum the white light pulse is split into two spatially separated pulses, a reference and a probe pulse, before being focused through the sample. The probe pulse is aligned to pass through the pump pulse from the NOPA described above while the reference pulse passes through an unexcited portion

of the sample. The two beams are spectrally dispersed by an Oriel spectrograph (Model 77400) imaging polychromator and simultaneously detected on a CCD sensor (Hamamatsu S7031, 1044x128 pixels) cooled to -10 °C using a multistate thermo-electrical cooling system with the probe signal recorded on the lower 64 pixels and the signal on upper 64 pixels.

To correct for the positively chirped WLC in the measured transient spectra, an independent measurement of the chirp is carried out and used to correct the pump-probe spectra for time-zero differences. The measurement of the chirp in the probe pulse was done using a cross-phase modulation (XPM) artifact signal which is generated by the interaction of the pump and probe pulse in the sample medium.[77-79] In practice, most any solvent can be used though we have found the magnitude of the artifact to be strongest in THF. This XPM artifact is convenient as the measurement can be done in the same experimental arrangement as is used for measuring a sample and does not require an additional non-linear mixing crystal (typically BBO). The XPM artifact can be rather complicated but this method offers the benefit that the measured chirp accounts for any additional positive dispersion from the sample solvent and cell used for the experiment. We have previously studied such effects on the WLC chirp and published our findings in detail.[76] To mathematically compensate for the chirp in the measured spectra, the time vector of the measured data is shifted for each wavelength according to the measured chirp. For the new time points, the OD values are linearly interpolated between the OD values of the corresponding nearest neighbor points. This correction is used when displaying spectral variations over time, but for single kinetics analysis the raw data is used. The overall time resolution of our system is on the 50-200 fs timescale

assuming Gaussian line shape measured by the cross-correlation function of the pump and probe pulses and with a spectral resolution of ~7 nm. Lastly, a magic angle polarization difference ($\tan^{-1}(2^{1/2}) = 54.7°$) was maintained between the pump and probe pulses to avoid contributions from orientational relaxation effects.[75]

One of the core components of our broadband system is the white light generation step. The broadband pulse is generated within the CaF_2 crystal where the 775 nm pulse is most tightly focused. It is well known that the interaction of intense laser pulses with transparent media, not just CaF_2, can results in vast spectral broadening ranging from the infrared to the ultraviolet spectral region.[80-82] While the use of this method is fundamentally important to many applications such as broadband probe generation and optically parametric amplifiers, the mechanism of how the white light is created is not very well understood. Typically the process is believed to involve several nonlinear processes including self-phase modulation (SPM),[81] optical "shock-wave" formation,[83, 84] space-time focusing[85] and plasma generation by multiphoton ionization.[86] Our group has recently published a detailed examination of the polarization properties of the WLC generated in a CaF_2 plate used for our pump-probe experiments and explored the corresponding implications on the generation mechanism.[87]

Importantly, by controlling the input pump pulse wavelength for the WLC generation, the spectral window can be adjusted across a very broad range. This has important implications on what spectral transitions can be interrogated. For semiconductor quantum dots, where excited state absorbance transitions are further into the IR, and ground state bleaching signals can extend to the red of 700 nm, it would be beneficial to probe further into the NIR. In Figure 2.4 is shown the WLC from pumping CaF_2 and a

sapphire plate pumped with a NIR pulse generated in our NOPA. Consistent with what is observed when pumped at 775 nm, the WLC from the NIR-pumped CaF_2 plate extends further into the blue than the signal from the sapphire plate. Importantly, the CCD detector is not sensitive beyond 1100 nm so examination further into the IR was not possible. As mentioned, our NOPA can be tuned well into the NIR to generate pulses out to 2000 nm, which should extend the broadband pulse considerably. Also shown in Figure 2.4 is the WLC typically obtained from pumping CaF_2 with the 775 nm fundamental pulse showing a signal from ~300-700 nm as a comparison.

Figure 2.4: Broadband continuum extending into the NIR from sapphire (dash) and CaF_2 (solid) plates generated by pumping each crystal with 1300nm and 1200 nm light respectively. The continuum can be extended further if pumped at a longer wavelength. For comparison, the broadband pulse generated from 775 nm in CaF_2 (dot) is shown.

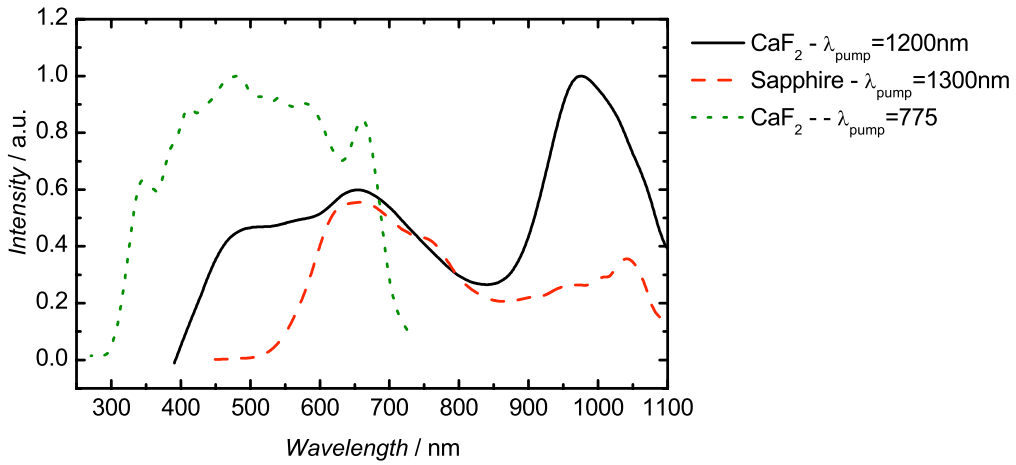

2.3 Data analysis software

2.3.1 Mathematical background

After chirp correction by time-vector shifting as described above, the transient data are processed by a self-written analysis software suite described in detail in Section 2.3.2. The output of a pump-probe experiment is typically represented as a rainbow of spectra, indicating the progression of the transient signals over time, as presented in Figure 2.5, allowing for specific bands of interest to be identified and qualitative observations made before being analyzed at single wavelengths. One important function of the software is to do a Levenberg-Marquardt least-squares nonlinear curve fit of the decay kinetics at a single wavelength of interest. The details of the coding allow for a

Figure 2.5: Typical plot of transient absorbance signals measured from 0-1900 ps showing bands of interest at 450 nm, 500 nm, 586 nm and 600 nm. The early time spectra are shown in blue (highest intensity) and later times in red (lowest intensity). Note: When printed in black and white, the blue appears darkest, transitions through light gray and back to a dark gray for the red.

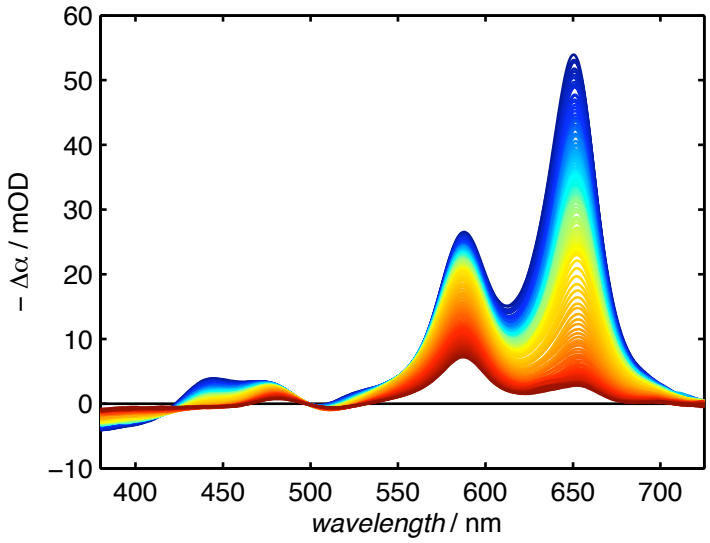

sum of unlimited exponentials, however typically a fit is done with the sum of five or fewer, as has been previously introduced by our group.[75, 76, 88, 89]

The single wavelength kinetics can be modeled by convolution of the product of an instantly rising exponential component $F_\lambda(t)$ at a specific wavelength with the instrument response function of the experimental setup, $g(t)$. The response function is assumed to be Gaussian and is represented in eq. 2.1, properly normalized, as:

$$g(t) = \frac{1}{\sqrt{2\pi}\sigma}\exp\left[\frac{-(t-\tau_0)^2}{\sqrt{2}\sigma^2}\right] \tag{2.1}$$

where σ is the standard deviation of the instrument response and τ_0 the actual time-zero. $F_\lambda(t)$ is the sum of up to *n* exponentials, having the form:

$$F_\lambda(t-\tau) = \sum_i^n c_i e^{-(t-\tau)/\tau_i} \tag{2.2}$$

for $(t-\tau) \geq 0$. The resulting time-dependent signals $S_\lambda(t)$ is thus:

$$S_\lambda(t) = \int_{-\infty}^{t} g(\tau)F_\lambda(t-\tau)d\tau \tag{2.3}$$

which can be solved analytically to give the time-dependent form of the single wavelength signal as:

$$S_\lambda(t) = \sum_i^n \frac{c_i}{2}\exp\left[-\frac{1}{\tau_i}\left(t-\tau_0-\frac{\sigma^2}{2\tau_i}\right)\right]\cdot\left\{\mathrm{erfc}\left[-\frac{1}{2\sigma^2}\left(t-\tau_0-\frac{\sigma^2}{\tau_i}\right)\right]\right\} \tag{2.4}$$

In equation 2.4, τ_i is the decay time component with corresponding amplitude c_i; $\mathrm{erfc}(x)$ is the complementary error function; the full-width at half maximum duration of

the experimental response (*FWHM*) is related to σ by $FWHM = 2\sigma\sqrt{2\ln(2)}$ and τ_0 is the time shift used to determine the absolute time-zero.

2.3.2 MATLAB data analysis suite

After acquisition, chirp correction and averaging of multiple scans, the output of a experiment is a large matrix of transient spectra, often with 200-400 spectra per array. Traditionally the data are first processed, plotted, and preliminarily analyzed using a Spectrum Analyzing Software package written by our group.[88] While this package was extensive and very capable, it was difficult to use, required a lot of computational time to execute, often taking minutes to successfully process data and give a merged table for further kinetic analysis, required the user to manipulate a set of configuration files to control the output of the program and did not offer a user-interface or any control while executing. Furthermore, the output of the program was a vast array of image, configuration and data files, most of which were not needed, consuming large amounts of space and making extraction and manipulation of the data a cumbersome process. Lastly, after processing, the user still required the use of an Origin® data processing package to plot single wavelength traces on a single axis and analyze them by fitting the dynamics to equation 2.4 above.

In light of the difficulties in processing the large amounts of data obtained from a set of experiments, a more comprehensive data processing suite was written in the MATLAB® programming language offering a graphical user interface (GUI) that allows users to easily view and manipulate data, including easily performing a least-squares fit on single wavelength kinetic traces with a user definable tolerances and number of

exponents. The program was critical to the processing of the acquired data presented in Chapter 3 and is aimed at replacing our older processing software. Accordingly, I will describe in detail the use of the three basic functions here as well as important scripts. The three programs include a simple kinetics and transient spectral viewer, a program for plotting and extracting single wavelength kinetics traces including the ability to directly compare up to three traces allowing for user-defined normalization, and a single wavelength signal fitting package.

The analysis suite is a self-contained directory and is installed by simply adding it to the MATLAB® Path. To execute a command that operates on the exported data, the user first sets the current working directory to where the unique data set is saved, as exported from the spectrometer program, and execute one of the main functions from the MATLAB command-line.

kineticsPlot – A simple transient signal viewer

The purpose of this program is to provide a simple means to quickly look at the transient spectra and compare up to 6 decay signals in a format that can be exported to a high resolution image file or printed directly and provides the important information about the experiment allowing for easy reviewing. This is typically the first report that we generate to evaluate an experiment as it gives a good overview of the data. The function is activated and GUI displayed by executing “kineticsPlot” at the MATLAB® command-line. The program will search for a set of data in the current working directory and run. If more than one set of data is present, it will operate on which ever set comes first alphabetically. Typically, only one set of data is contained per directory. A screenshot of

the program is shown in Figure 2.6 below. The specific features and user-interface controls are detailed here.

- The main screen is divided into three sections, one showing the transient absorbance spectra, another presenting single wavelength signal vs. time plots for user defined wavelengths and the last presenting the important variables regarding the experiment. This last portion provides the user with the directory where the data is located for easy referencing once plotted, and the parameters set at the time of the experiment on the data acquisition software. These parameters include the sample name, CCD array integration time, pump wavelength, duration and energy, as well as any comments entered by the user regarding the experiment.
- The program provides facile user control over the plotted single wavelength kinetic traces with up to 6 traces displayable at a time. The user selects the desired wavelengths to display by entering the wavelength along the top of the transient spectra after which the corresponding kinetic trace is displayed to the right side of the GUI. The timescale of the displayed kinetics are controlled by a single variable in the top right-hand corner. This offers the benefit of allowing the user to easily set the resolution desired. By default this is set to 5 ps as most of the dynamics of interest in the current experiments occur on the single picosecond time scale. Importantly, if there are fewer than 6 wavelengths of interest, the user simply has to enter something other than a number, leave a cell blank, or enter “0” and the program will interpret and hide the axis the cell is tied to.
- The largest axis displays the transient signals over a user specified range. By default this is set to display all measured spectra. To change the range of displayed

transients, the t_{min} and t_{max} cells are changed and the program responds accordingly. Additionally, the user can change the spectral range and the absorbance range by changing the values in the corresponding cells on the axis of interest. This feature allows the user easy control over the appearance of the displayed signals, which are instantly updated when a cell is changed.

- In order to plot or save the displayed report the user has three options. The first is to simply print it to their local printer using the default “Print…” dialog in MATLAB®. This is accessed by pressing the “Print…” button or through the pull down menu. This can be also used to export the figure as an image file. However, this latter process has been automated through two other buttons in the GUI. The user can export the figure in either a 300 dpi jpeg format or a vector graphics encapsulated postscript file to the current working directory. The file name is automatically generated as the function name with a number index, which starts at 1 and automatically increments (e.g. kineticsPlot1.eps). The index of the next export is displayed next to the function calling buttons so the user can automatically control the option if overwriting a previous file is desired. This process allows for very rapid report generation and facile data sharing.
- Lastly the program provides buttons to easily call the TAViewer2 function or plotRainbow function, which are both discussed below. This allows for easy translation between different functions in the analysis suite.

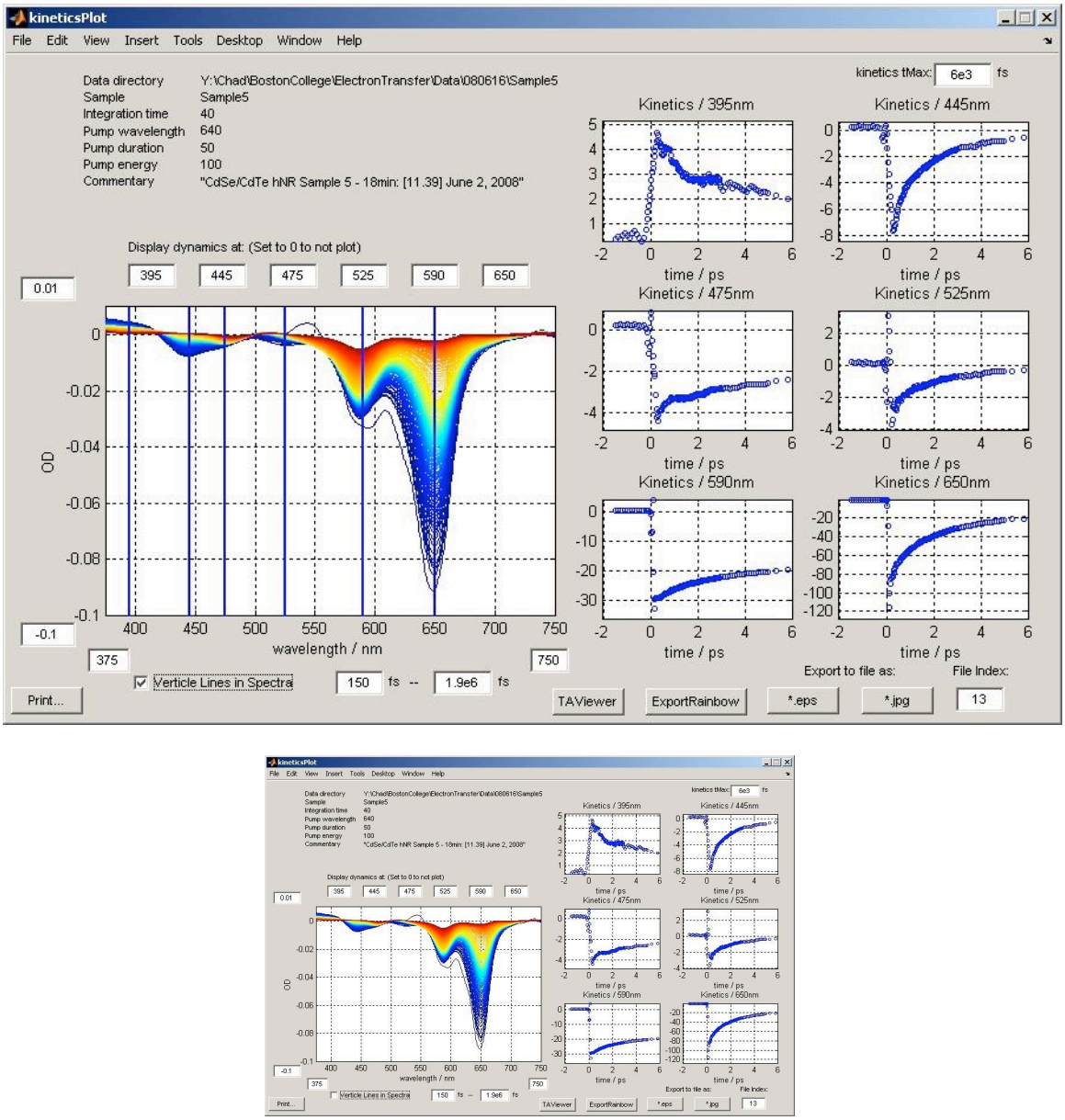

Figure 2.6: Representative screenshot of kineticsPlot GUI showing the processing of the data shown in Figure 2.5. The lower inset shows the same program without vertical lines in the transient spectra window, a feature that can be easily toggled on or off.

TAViewer2 – A transient signal viewer and analyzer

The TAViewer2 function is a new tool for processing and exploring the data quickly allowing for easy comparison of multiple single-wavelength signals over time as well as easily view single transients at specific times. Originally, TAViewer was written to perform this last feature and can still be used. The program was later updated and in its current form as TAViewer2 has a number of additional functionalities. Like the rest of primary functions in this suite, the GUI is activated by executing "TAViewer2" from the command-line of MATLAB® or alternatively from an external call from the kineticsPlot GUI. The program searches the current working directory for a data set, selecting the first set alphabetically.

This interface's primary function is to allow the user to easily explore single-wavelength decays and export the data, as either the complete data matrix, single transients or single-wavelength signals, in ASCII formats easily imported in other analysis programs. Additionally, this program offers an easy interface to the data fitting function described below significantly increasing the speed of data processing. A screenshot of the program is shown in Figure 2.7 to give a sense of the GUI setup. The specific functions and options of interest are described here:

- The GUI is divided into two sections, one showing the transient spectra and one showing the measured absorbance as a function of time for a given wavelength. Below each of these axes the user is presented with a number of interfacing tools to control the output.

- The axis on the left can display the transient spectral data either as single spectrum, or as a series of spectra between a user-defined range. The interchange between the two modes is controlled by a single checkbox. As in the kineticsPlot GUI, the x and y-axis scales are controlled by textboxes arranged at the extremes of each axis and are updated automatically. In single transient mode the user can scroll through the data using the slider bar or can type in a specific value in the corresponding text box.
- The axis on the right is used to display the signal vs. time at a specified wavelength. By default, the program only displays a single kinetic trace, the wavelength of which is set by the slider bar or cell directly below the axis. The selected wavelength is also indicated in the spectral window by a color coordinated vertical bar through the spectrum. This bar can be disabled if desired by the appropriate checkbox. Additionally, a second and third trace can be plotted by activating the appropriate checkboxes. Each trace is plotted using a different color and maker for clarity. Often the amplitudes of different bands are different but need to be normalized for careful comparison. This feature is made available by dividing the signal by a set value with the default normalization values set to the maximum amplitude of the selected wavelength. This normalization is automatically updated when the user changes the indicated wavelength but can be set manually and held fixed if necessary.
- As with the other primary interfaces the program offers the ability to export the GUI as an image or printed as a report. The image is saved with the prefix TAViewer and the indicated index. Both 300 dpi jpeg and vector graphics encapsulated postscript

(EPS) formats are made available. Typically the EPS format is used because of the higher resolution when printing.

- The interface offers a number of ways to export the data to formats that can be used by other data processing software. The first is presented in the center of the GUI that allows the user to export the data as a comma-separated table of transient spectra. This was a traditional export format for the older Spectral Analysis Software and is included for backwards compatibility. However usually only a few transient spectra or signal decays are necessary so TAViewer2 offers an easy means to simply export the displayed single wavelength signals as text files, named according to their wavelength, or single transient spectra, named according to their recorded time. Often the user may wish to manually set the “actual” time value for the spectrum to be exported to account for the appropriate t_0 or to round the time to an appropriate time. This can be done by the indicated checkbox and data cell.
- The last feature, and probably the most useful feature, is the interfacing of the GUI with the TAFit function which allows the user to quickly and easily do a least-squares fit of the selected signal. Each of the three wavelength selectors has a button to call this function and passes of the selected data for analysis. This offers a very easy means of choosing a signal of interest and doing a full characterization without having to call TAFit from the command-line.

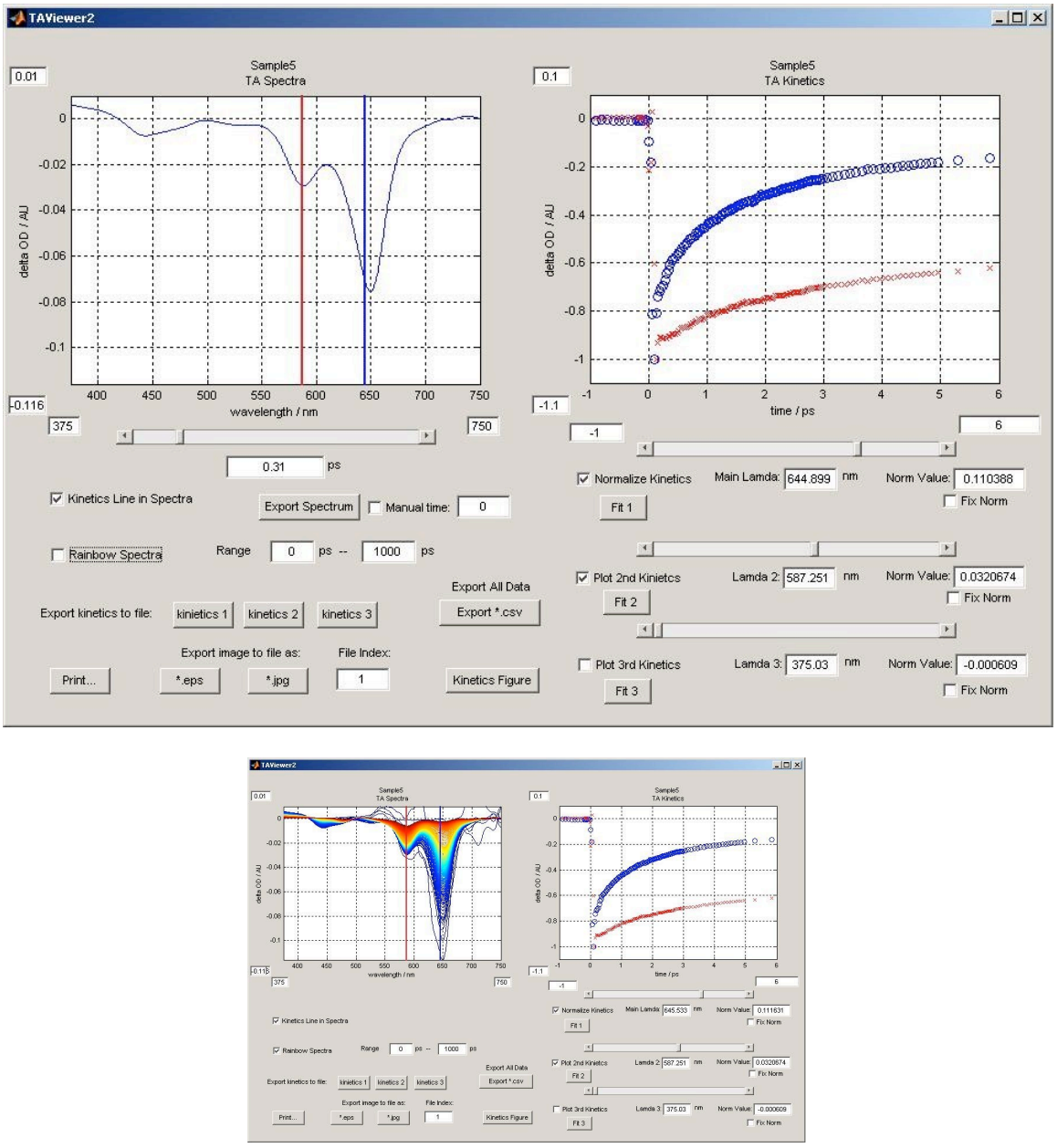

Figure 2.7: TAViewer2 screenshots showing the manipulation of the transient signals from the representative experiment in Figure 2.6. The small inset below shows the same figure with a traditional “rainbow” plot instead of the single transient spectrum.

TAFit – Signal least-squares fitting

The TAFit tool was written to replace the process of exporting data and importing single wavelength signal dynamics into Origin® for fitting using equation 2.4. This time-consuming step was inhibited by the multiple manipulations necessary to get data ready to be fit as well as the cumbersome user-interface. Originally, the TAViewer2 tool was used to help speed this up by facilitating simple exports of single traces which could be quickly imported and fit. However, y including a separate set of fitting tools as part of the analysis suite allows the data to be quickly and easily processed in a more complete manner. In this way fits of multiple wavelengths can be quickly made and figures plotted for rapid report generation.

The TAFit program does not scan for a set of data, but instead data is passed to the function as input variables. The data must be arranged as either a two-column input array [x, y] or as a cell structure containing the data in a cell named “data” (e.g. [x, y] = *structure_name.data*) though typically the former is used. The latter is helpful as it can directly read the input data structure created from the importdata.m function built into MATLAB®. A second variable can also be passed to set the title of the plot in the figure, identifying the sample being characterized, e.g. TAFit(data_array, title_string). When called from the TAViewer2 GUI, the TAFit is passed the current x-y data of the selected signal trace along with the title of the current sample being examined. However, it can also easily be called from the command-line to fit any signal.

The heart of the program is made of the interplay between the coded representation of equation 2.4 and the Levenberg-Marquardt least-squares nonlinear curve-fit function lsqcurvefit.m built into MATLAB®. Equation 2.4 is constructed as function pumpprobefun2.m and interfaced with the recursive curve-fitting tool by pumpprobefitfun2.m. The subtleties of this interfacing is complicated by the fact that not all the set variables are necessarily going to be varied requiring two sets of input variables be included in the fitting function, one being a complete set of variables from which a curve can be generated, and the other being the input that will be manipulated by the curve-fit script. A separate “fit-function” is used in conjunction with a basic curve generation function to facilitate user manipulation and processing of the data outside of the fitting process. This might include manually changing specific input variables and wanting to see the effect on the output curve, later workup and processing of fitted data, as well as simple plotting functions built into the TAFit GUI. This basic function that represents equation 2.4 takes as its only input a single array containing all the required variables and the independent variable vector. Based on the input variables array, the function determines the number of exponents to use and then evaluates and outputs the corresponding signal vector *S(t)*. For example, given a vector of input variables *var* = [A_0 t_0 *FWHM* A_1 t_1] corresponding to a single exponential decay with an amplitude and lifetime A_1 and t_1, a time-zero t_0, an instrument response function (IRF) corresponding to *FWHM*, and a background signal of A_0, the kinetics signal may be calculated as: *S(t)* = pumpprobefun2(*var*).

The GUI offers a user-friendly interface and a number of smaller or subtle features that should be highlighted, which provide additional control to the user. Some of these

features can be seen in the screenshot of the GUI in Figure 2.8. The main window is composed of a single axis on which the data and a fit line are plotted surrounded by the input variables at the bottom and the fitting tolerances and settings to the right. The variables are set by changing their values in the corresponding cells and they are set to be varied in the recursive nonlinear fitting process by selecting the indicated checkbox. By default when the GUI is first activated the A_0, t_0, and IRF values are set to be fitted along with a single exponential decay curve. After setting the variables that are to be used for the data fitting, the "Fit…" button is pressed to begin the recursive least-squares fitting algorithm. Typically, if multiple exponentials are expected to be necessary it is better to add the exponential pairs one at a time. Otherwise, as is typical with the nonlinear searching algorithms, it can be difficult, if not impossible for the program to find the appropriate minimum.

In some instances, the user may wish to set a variable manually and see the effect on the generated curve. This may be performed by using the "Plot…" button, which simply reads the input variables and plots the corresponding curve. This is particularly helpful if the user wants to "direct" the fitting algorithm toward the solution by attempting to place it near a relative minimum. It can be particularly useful if the data has a strongly shifted t_0 and the program attempts to use the *IRF* to account for it when trying to get a first approximation. Alternatively the user can set some variables manually, checking with the "Plot…" button if they are close, select them not to be fit, and then use the fitting function to approximate the remaining variables. This often helps find the appropriate minimum.

A second added feature that the program offers is the ability to manually remove data points that should not be considered when performing a curve-fit. Often near t_0 there is a lot of noise in the measured transient from the XPM and a few data points should be removed when searching for a suitable fit. This can be accomplished by clicking the “Edit Points” button which will activate a crosshairs selector with which the user can select the specific data points to be omitted. Clicking on a data point toggles its current status, selected/omitted. When tagged to be omitted the data are plotted as green points by default. They can also be hidden from the display by unselecting the appropriate checkbox on the right hand side. This feature is particularly helpful when fitting data with multiple exponents and the program adds a very fast sub-fs component to account for an artificially strong signal point. Similarly, noise around the t_0 area causes the fitting process to slow down as the program tries to vary A_0, t_0, *IRF* and an exponent to account for the data in that region. Removing suspect points will often speed this process up substantially. If necessary, clicking on them again in the edit mode can reset hidden data, or all data can be reset using the “Reset Points” button.

The data to be fit can also be normalized by dividing by a constant, the default taken to be the amplitude of the curve, by activating the assigned checkbox. This is particularly handy when comparing data from different experiments or when interested in the relative amplitude of different components. For most of the experiments presented in this work the data are normalized in this fashion.

Often some of the variables being used in the TAFit, particularly the raw data and the fitted variables, need to be exported to the command-line for further data processing or figure manipulation. This is helpful for publishable figure generation and passing off the

data to other plotting software. This can be achieved by using the “Export” button, which saves some important variables to a global variable “TAFitData.” At some point an import feature along the same lines that reads either this or a different global variable will be included.

Lastly, as with the other programs in the suite, this GUI has print and save-as-image features. The filename is usually automatically generated but can be manually set by entering a string in the bottom textbox. Both the manual name and the default name are appended with the file index number and the corresponding format suffix.

Figure 2.8: TAFit screenshot showing the analysis of the single wavelength signal changes at 646 nm of the sample shown in Figure 2.6.

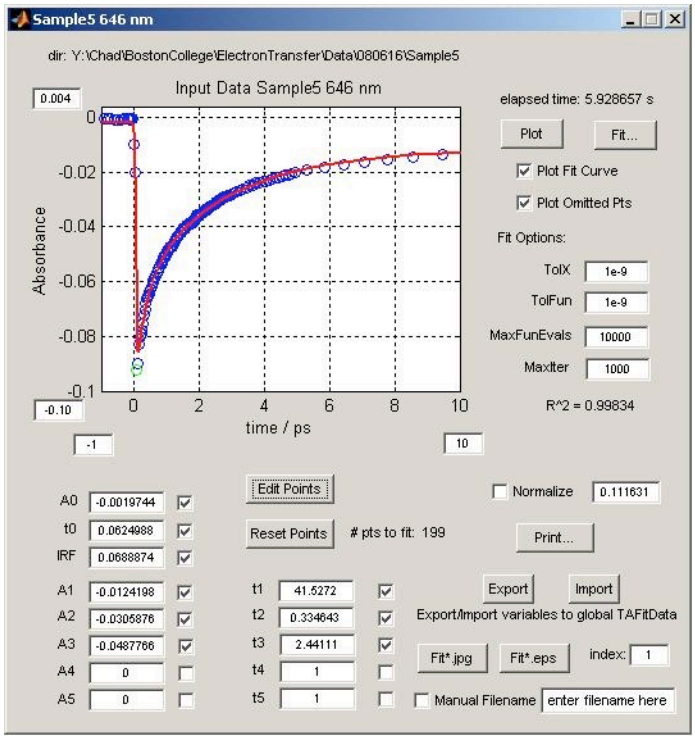

Other Scripts – plotRainbow

A number of additional support functions and scripts have been written that are part of this analysis suite. A last one that should be highlighted, as it is important for generating the classic “rainbow” plots like that shown in Figure 2.5 in a publication quality format is the plotRainbow script and the corresponding rainbowCleanup script. Both of these can be called from the kineticsPlot GUI by selecting the “PlotRainbow” button.

The plotRainbow script reads through the current directory the same way as is implemented in the GUI programs described above. It then generates a plot of all transients in the ranges specified by the user in the script. Accordingly, to interact with this program the user must edit the script directly to enter the required values for important variables. The rainbowCleanup script operates on the generated figure and resizes it to the precisely desired dimensions and scales. Again, these values must be set directly within the script. Also, text entry statements are present that can be uncommented to label important peaks or add arrows and lines if desired. The in-script editing was chosen, as apposed to passing important variables to called functions, to keep the figures and important variables accessible in the current workspace.

By leaving these programs as scripts, their execution leaves all used and generated variables in the current workspace giving the user access to the axes and plots thus. For example, if the user needs to add additional data to the generated transient spectra figure, or wants to manipulate text on the axes manually, these variables and the axes

handle need to be accessible from the command-line. Keeping these functions as directly editable scripts facilitates this control. The use of these two scripts demands a more developed background in the use of MATLAB® as a data processing system and is not intended for “turn-key” use like the GUI programs above are. However, each script is thoroughly “commented” to allow a user to easily understand what can be changed to manipulate the output.

3 Electron transfer in heteromaterial quantum rods

3.1 Introduction and motivation

The increase in demand for consumable energy and rising cost of fossil fuels, both pecuniary and environmental, have presented a formidable challenge to the scientific and engineering communities to develop alternative sources of energy capable of scaling with continued economic and industrial development. The increasing consumer demand for energy and its potential impacts on the world is highlighted in the Appendix (Section 6) and is the motivation behind the work detailed in this dissertation. The work presented here is fundamentally interested in the chemistry and capabilities of the relatively new class of semiconductor quantum confined materials for harnessing solar energy and converting it to usable energy.

Research into the development and improvement of photovoltaic technologies has started to explore the promise of improved efficiency[3, 54] and an increased spectral sensitivity offered by semiconductor nanomaterial based devices and organic/semiconductor hybrid designs[32, 65, 90-93] while continuing to explore the capabilities of carbon based organic devices.[94-96] In 2005 the Alivisatos group published a paper on a semiconductor quantum rod based photovoltaic cell made from a mixture of CdTe and CdSe materials showing a ~3% power conversion effieciency.[58] A large number of other groups have published similar findings, some using a more traditional Grätzel-cell structure[32] and others focusing on an all-inorganic structure.[60, 61, 66] Furthermore, for more than a decade these materials have been implicated for use in

photoelectronic applications and been the motivation behind innumerable peer-reviewed scientific publications on semiconductor quantum confined materials. Yet very little work has come out on evaluating their over all capabilities built on a fundamental understanding of their photoelectronic properties. It was this observation that motivated the work presented here where efforts to measure charge carrier separation dynamics in semiconductor nanostructures are presented.

All solar cells rely on three basic steps to operate: (1) Charge carrier generation by photoexcitation, (2) charge carrier spatial separation, and (3) carrier transport through the photoactive medium to the rest of the circuit. Thus, effecting efficient charge separation and carrier mobility is critical for efficient photocurrent generation in photovoltaic devices, and therefore of target for operational improvement. From these three steps, the key photophysical process in photocurrent generation is effective charge separation after a photon absorption event. The charge separation event has to compete with the nanosecond scale exciton recombination event and a number of potential picosecond timescale relaxation pathways. A more complete understanding of these competing pathways for energy redistribution is critical to the improvement process and engineering of photovoltaic devices based on these nanostructures and to help move their development beyond a blind search through different structures to an intelligent design motif. To this end, the time-resolved ultrafast capabilities of the Fiebig group are ideally suited to perform charge separation dynamics measurements. Such experiments allow us to begin to understand the fundamental capabilities and limitations of semiconductor nanoparticles for application to photon energy conversion by allowing us

to study charge transfer, the key first step in solar energy capture, as a function nanoparticle chemistry.

A nontrivial challenge to this work was to get an electron donor (CdTe) in very close proximity to an electron acceptor (CdS or CdSe) in solution so that it could be monitored by a transmission based broadband pump-methodology. In solution, the two constituents are isolated not only by solvent but also by long-chain hydrocarbons from organic syntheses or a charged shell of short organic acids in aqueous syntheses. Section 3.2 below details studies that were performed to determine how best to give good electronic coupling suitable for the transmission absorbance experimental methodology.

3.2 Colloidal heteromaterial structures

When first designing this project to measure carrier separation dynamics in II-VI semiconductor heterojunctions, the key chemical challenge immediately presented was how to create these heterojunctions in a sample that was soluble in aqueous or organic solvents and that had a donor and acceptor that were both electronically accessible. Many researchers have worked on core/shell quantum dot structures with the idea of studying charge separation as it relates to photovoltaic devices.[97, 98] The problem with core/shell structures is that while they give improved material properties (less toxic) and higher emission quantum yields, either the hole or the electron is isolated from the outside environment thus prohibiting a ground-up use of these materials in photovoltaic devices. In an attempt to keep the materials that were characterized in solution as close to those that might be used on a solid-state photovoltaic device, core/shell materials were avoided.

3.2.1 Ligand directed coupling of aqueous quantum dots

The aqueous synthesis of CdE (E = S, Se, Te) nanoparticles offers a number of benefits over conventional organometallic approaches, including inexpensive ligand systems, access to strongly quantum confined nanoparticles with diameters <4 nm, relatively simple reaction conditions with nucleation and growth temperatures at <100 °C, shorter precursor preparation time, and less stringent requirements on an inert atmosphere. For these reasons, we started exploring means of coupling particles in aqueous solutions. Furthermore, the ligands used in aqueous syntheses are usually significantly shorter than those used in organometallic approaches. In Figure 3.1 below, typical ligands used in nanoparticle syntheses are highlighted. Aqueous ligands are usually short-chain thiol containing ligands that are less than 5 Å long vs. ligands typically used in organometallic methods which are often >15 Å long. For these reasons, aqueous soluble nanoparticles were chosen to first try and examine donor-acceptor coupling chemistry.

Experimental – Aqueous CdE (E=S, Se, Te) synthesis

A large amount of work has been published on the aqueous synthesis of CdTe nanoparticles.[36, 44, 99-101] The procedure detailed here has been adapted from many different sources and modified as was found to work best in our hands. A detailed optimization based on emission quantum efficiency was not undertaken as it was

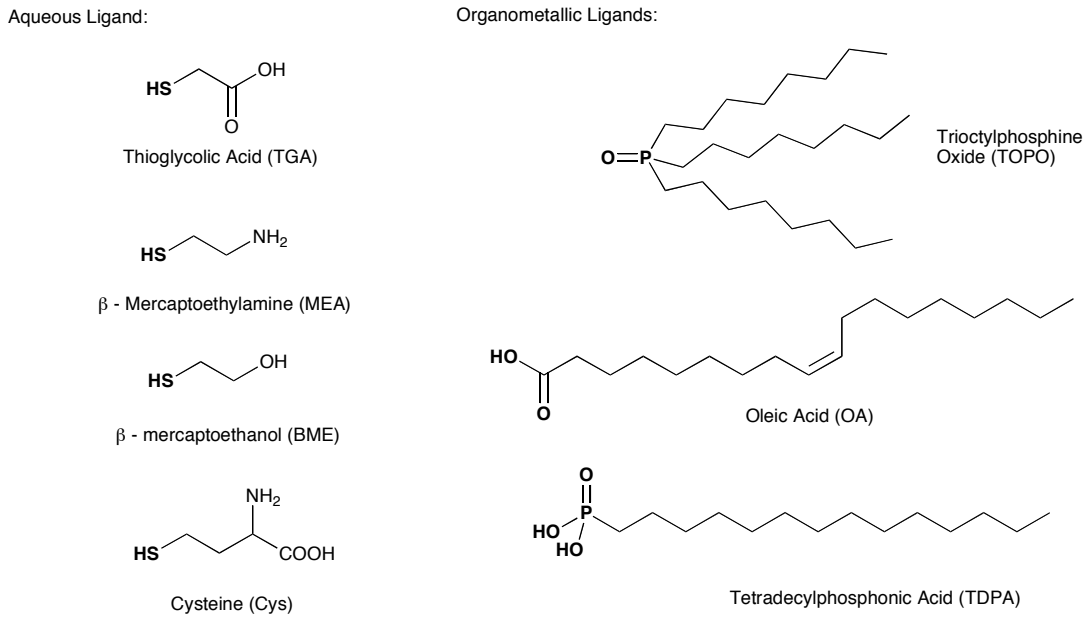

Figure 3.1: Typical ligands used in (left) aqueous and (right) organometallic syntheses of II-VI semiconductor nanoparticles. The surface-binding component for each ligand is highlighted in bold.

beyond the scope of the project. However, such work has been detailed by Guo elsewhere.[101] Below is the detailed protocol used for CdTe synthesis. This is directly extendable to both CdSe and CdS which both have a diminished O_2 sensitivity.

Briefly, the chalcogenide precursor NaHTe is prepared by the reduction of Te metal using $NaBH_4$. This is accomplished by first charging a 25 mL oven-dried and N_2-flushed round-bottom flask with a stir bar and the desired amount of Te powder (~200 mesh) to be reduced, typically ~25 mg. After adding the Te, the flask is then quickly sealed with a rubber septum. Any trace-O_2 that drifted into the flask during this step is reduced in the next step so additional N_2 flushing is not necessary. Subsequently, a 5-10x mole ratio of $NaBH_4$ to Te metal is measured (~60-70 mg $NaBH_4$ usually) in a 2 mL eppendorf tube

and dissolved in 1mL DI water. The solution is mixed and then injected into the sealed flask. The eppendorf tube can then be rinsed with an additional 1 mL of DI H_2O and added to the reaction. The sealed vessel is then weakly heated on an ~70 °C oil bath with moderate stirring. Care needs to be taken to vent the evolved H_2 from the reaction of $NaBH_4$ with water during the reduction.

Over about 15 minutes, the black Te metal powder is reduced and a light purple and then clear solution is formed. The reaction is complete when no more solid is visible in the flask and a transparent clear solution of aqueous NaHTe remains. Any purple color is indicative of a Te^{1-} precursor and if it remains after >1 hr, it is likely that O_2 is getting into the reaction. The heating step is optional; it serves to speed up the reaction and is not necessary further once completed. This precursor is extremely sensitive to oxygen and therefore must be carefully sealed during the reduction. The purple intermediate serves as an easily identifiable indicator of the reaction progress. If necessary, additional $NaBH_4$ can be added to help push the reaction to completion. Once the NaHTe precursor is formed, the solution is then diluted with N_2-degassed H_2O to give the desired stock concentration (10 mL H_2O - ~18 mM NaHTe), again keeping the reaction sealed. If excess $NaBH_4$ is still present, any dissolved O2 that causes the reaction to turn purple will be reduced and the solution will again clear up.

A solution of the ligand of choice (thioglycolic acid – TGA) and the cadmium salt of choice ($CdCl_2$) are dissolved in ~18 mL H_2O and the pH adjusted to 8-9. The quantities are chosen such that the final concentrations of ligand, cadmium and telluride precursors after injection of the NaHTe are 6.25 mM, 2.5 mM and 0.625 mM respectively (usually ~10 mg $CdCl_2$ and 11 µL of MPA are used). During the pH adjustment, the solution turns

cloudy around pH 4 but clear up above pH 5. After the ligand-Cd complex is formed, the solution is placed in a 2-neck round-bottom flask, outfitted with a septum and condensing column and heated with vigorous stirring to ~80 °C. While stirring, the desired amount of NaHTe is rapidly injected into the ligand-Cd solution and the reaction brought up to a weak reflux. The NaHTe will likely turn light purple in the transfer syringe but should not inhibit the CdTe formation.

The reaction rapidly turns yellow/orange with the nucleation and growth of CdTe nanocrystals and aliquots can be taken at different times to select different sizes. Growth time varies depending on the ligand used, but can be >500 minutes for TGA and >1000 minutes for mercaptopropionic acid (MPA). Other ligands with different functionalities may also be used with slight modifications to pH and temperature if necessary. CdSe and CdS are prepared in the same way but do not show size tunable emission spectra as does CdTe. CdS can be prepared from either reducing Sulfur or from a $Na_2S•9H_2O$ salt, which is usually easier to use. For this reason, experiments in this section used primarily CdS synthesized at room temperature.

For reactions with mercaptoethylamine (MEA), to yield positively charged ligands in aqueous environment, the reaction was done at either an unadjusted pH (pH ~5-6), or by adjusting to pH = 7.8 with KOH (aq) and yield particles with very good absorbance spectra but very weak emission. The emission spectra of MEA-CdS can be improved by removing excess MEA ligand by precipitation with isopropanol and resuspension in H_2O. Attempts to synthesize MEA-CdTe yields a soapy mixture of orange/yellow precipitate. Representative optical spectra for different CdTe, CdSe and CdS nanocrystals prepared as described above are shown below.

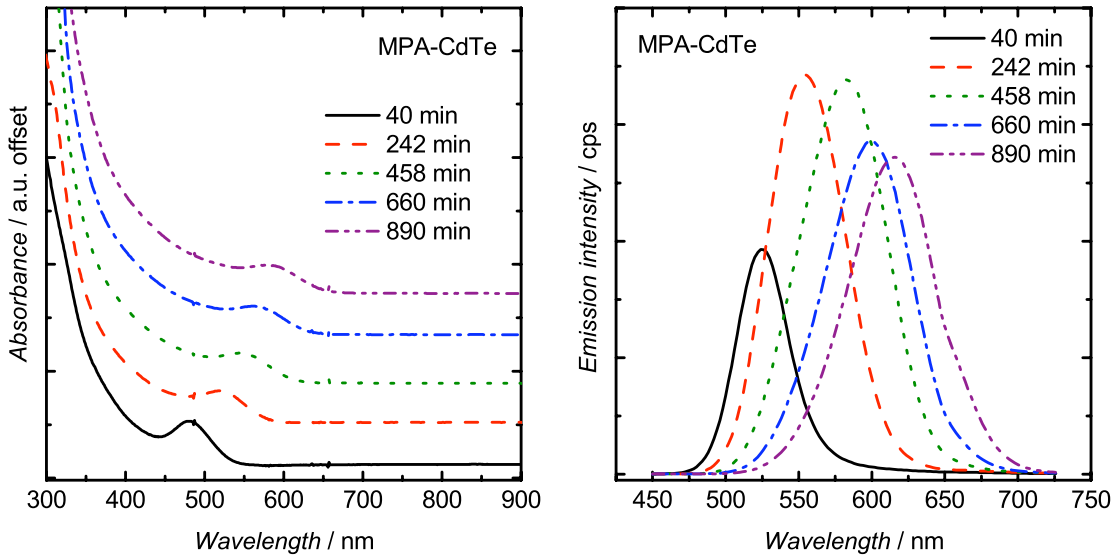

Figure 3.2: Absorbance and emission spectra of MPA-CdTe at varying growth times. CdTe, unlike CdSe and CdS shows good quantum confinement and band edge emission.

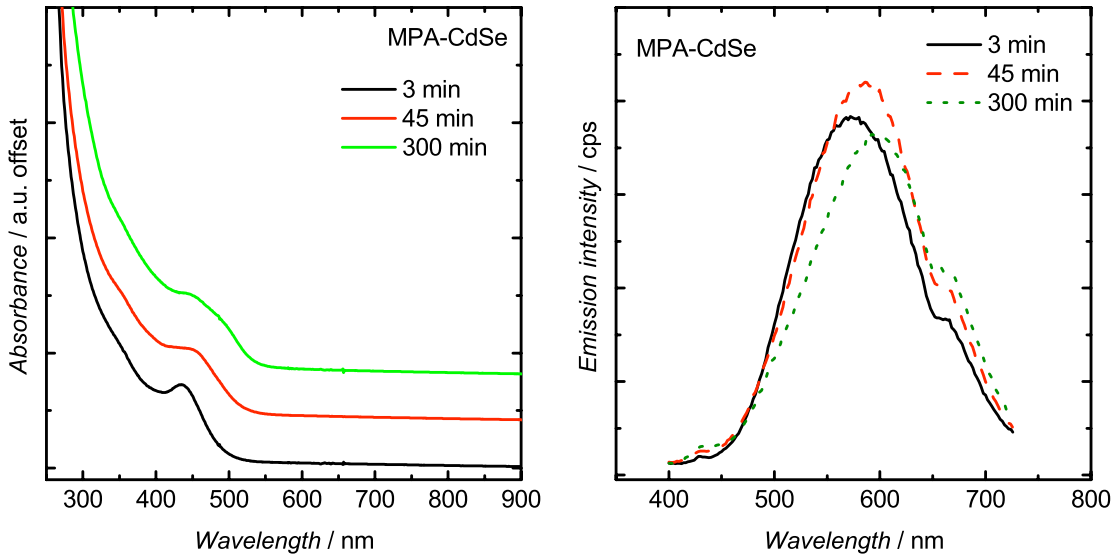

Figure 3.3: Absorbance and emission spectra of MPA stabilized CdSe with different growth times showing trap-state emission and a broadening out of the band edge absorption features.

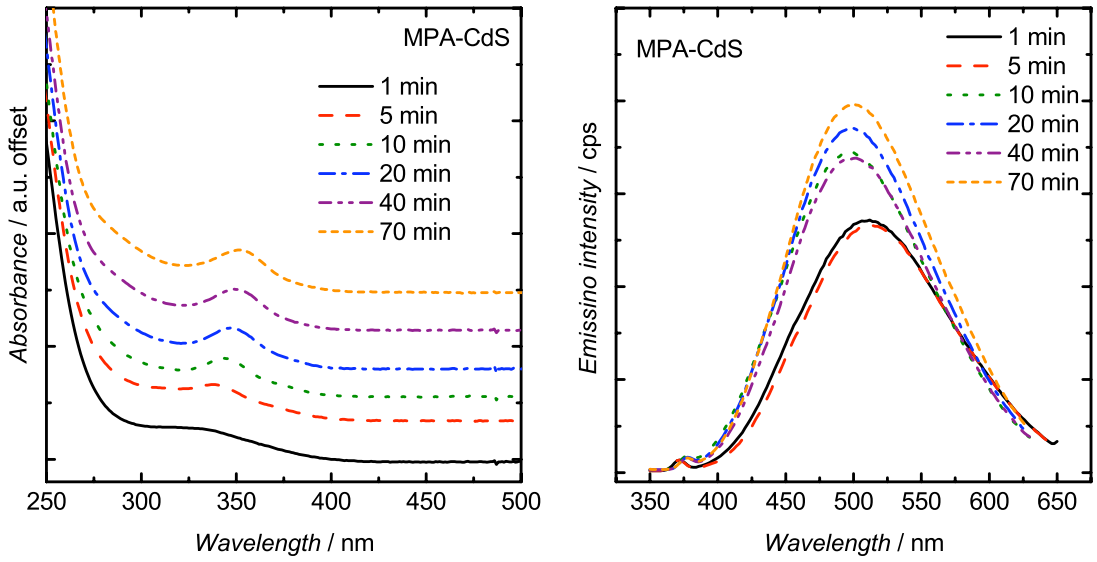

Figure 3.4: Absorbance and emission spectra of MPA-CdS with varying growth times. The small peak at 375 nm in the emission spectra is from Raman scatter from the aqueous solvent. No appreciable growth in particle size is evident over 70 minutes. Emission is from deep trap states.

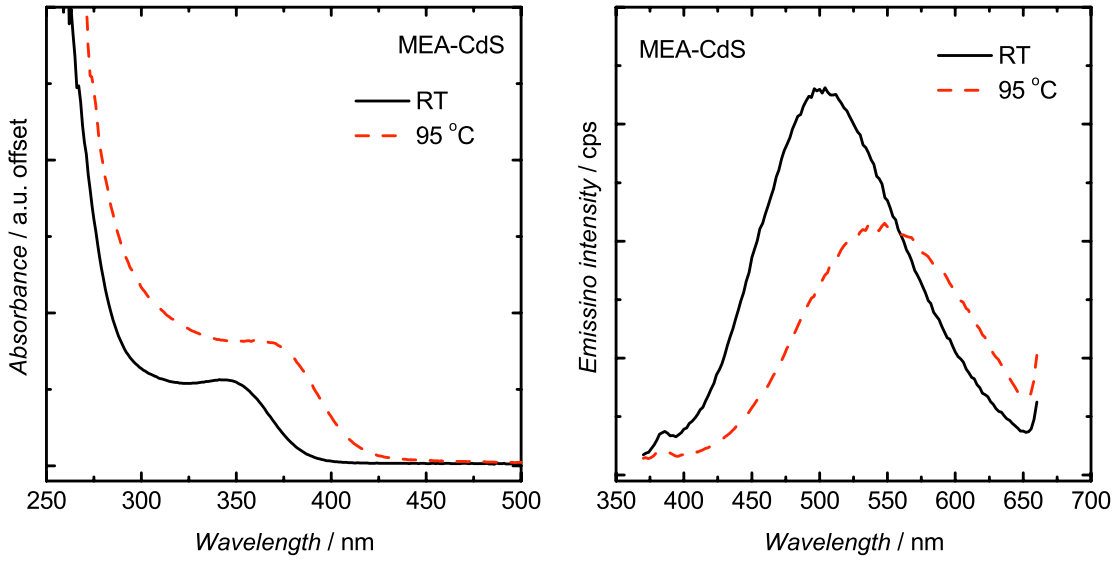

Figure 3.5: Absorbance and emission spectra for positively charged MEA-CdS nanoparticles. No appreciable growth was evident at elevated temperatures, similar to the findings with MPA.

Solution phase coupling

A number of different coupling motifs were devised for aqueous based materials, and those of interest are presented in detail here. In the experimental section above, two different primary ligand systems are highlighted, one producing particles with a negative charged surface (organic acids) and one giving particles with a positive charged surface (primary amines) at physiological pH. Based on these two ligand systems, three different schemes for forming a donor-acceptor complex immediately present themselves. They are (1) complex formation from electrostatic interaction, (2) ion mediated complex formation, and (3) covalent coupling by formation of an amide bond. Ultimately, none of these methods yielded materials suitable for pump-probe spectroscopy but the detailed chemistry and findings are described below for reference.

The most straightforward method was to simply mix a dilute solution of positively charge particles with negatively charged particles using electrostatics to direct them together in solution. This idea was previously used by Wargnier *et al.* where they observed energy transfer from positively charged green emitting CdSe particles to negatively charged red emitting CdSe particles.[99] They determined a Förster critical radius on the order of 7.3 nm, for interacting particles of 4.4 and 6 nm in diameter, and

Figure 3.6: Coupling of donor-acceptor particles by oppositely charged passivating ligand systems. Based on previous reports, they may get within 2-3 nm of each other in solution.

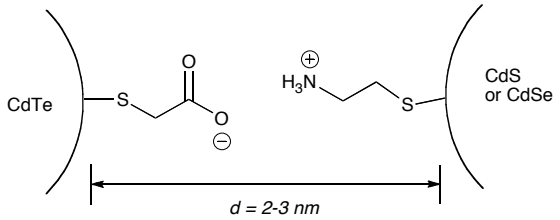

determined that the particles got within 2-3 nm of each other. With a surface-to-surface separation of ~2 nm, there is approximately a 1 nm solvent gap between the ligands. While this is sufficient for the dipole-dipole interactions necessary for FRET, it has not been indicated whether it would be sufficient for effecting electron transfer from a donor CdTe to and acceptor CdS or CdSe.

To perform the above experiment, TGA stabilized CdTe and MEA stabilized CdS were prepared as described above. The products were characterized by absorbance and emission spectroscopy and stock solutions prepared for mixing by diluting each stock 5-fold. Mixing of equal volumes of TGA-CdTe and MEA-CdS showed a weak change in emission intensity when viewed under 364 nm light, but

Figure 3.7: Mixing of (+)-CdS and (-)-CdTe show no evidence of emission quenching from charge transfer or energy transfer. Emission quenching from CdS addition is identified only by competitive absorption by CdS as indicated by excitation dependent emission studies.

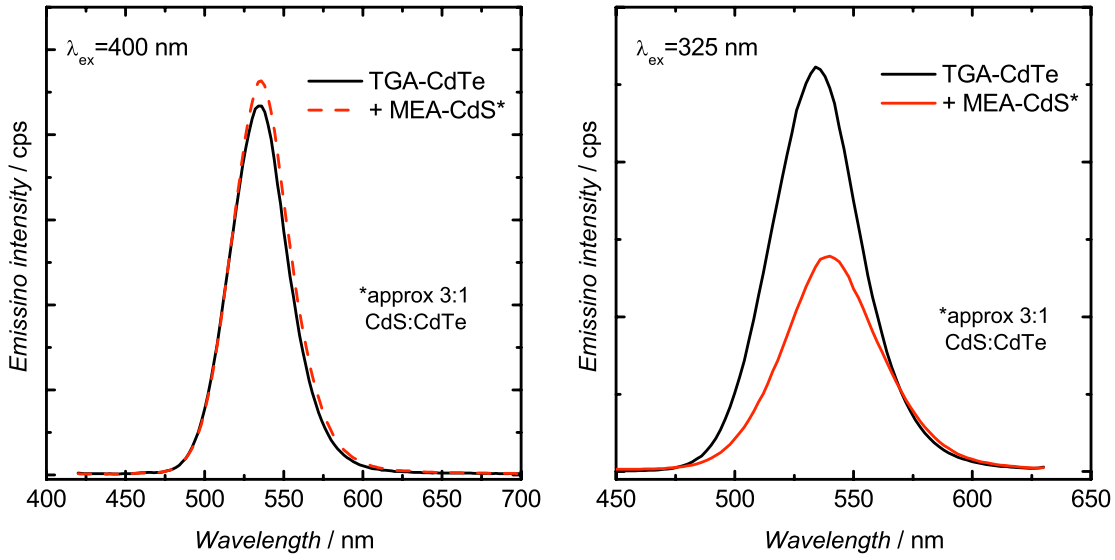

after examining excitation wavelength dependent emission spectra, the emission quenching was determined to be from competitive photon absorption only and not from any electronic coupling (see Figure 3.7). It was hypothesized that perhaps with the excess salts dissolved in solution from the synthesis, the charge screening was preventing any subsequent interactions

To remove excess salts and ligands from solution the products were dialyzed against pH 9 (TGA-CdTe) or neutral (MEA-CdS) water for 12 hours. After dialysis, a direct 1:1 mixture of the two solutions produced a rapid precipitation of product and an obvious red-shift in emission as observed by eye. To measure this quantitatively, a series of dilutions with varying ratios of CdS and CdTe was setup and the emission spectra recorded at different excitation wavelengths. Again, at an excitation to the red of the

Figure 3.8: Excitation dependent emission spectra of varying (-)-CdTe:(+)-CdS ratios.

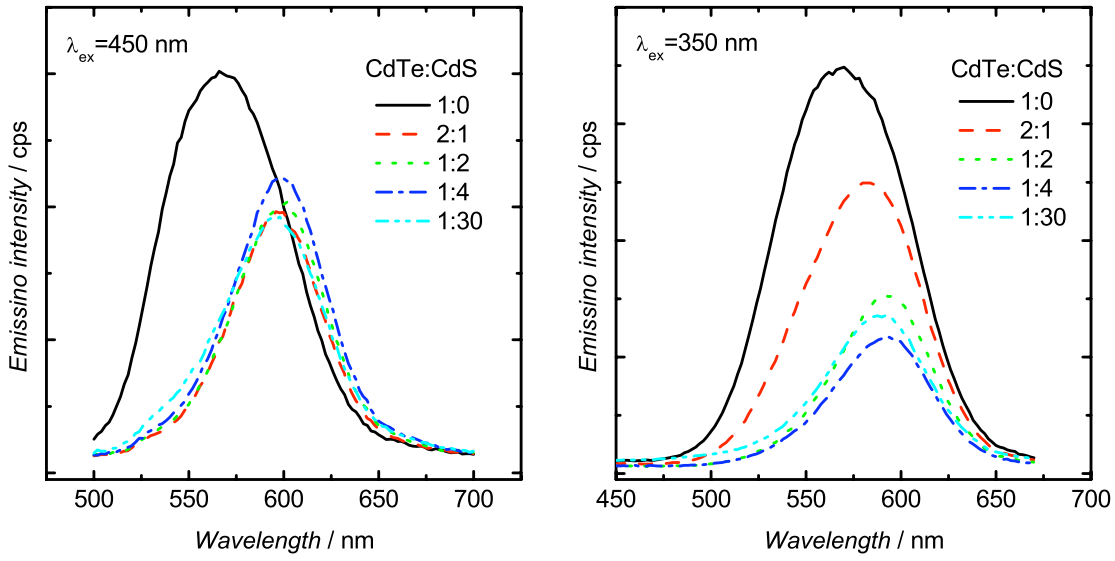

bandgap of CdS, no dependence on CdS concentration was observed. The decrease in emission intensity and the measured red-shift were consistent with the observations before precipitation. Importantly, when excited at 350 nm, at the absorption band edge of the CdS particles, the emission intensity again tailed off with increasing CdS indicative of competitive photon absorption. Lastly, since the materials slowly precipitated out of solution as a weakly red-emitting material, the emission spectra were measured in a plate-reader. Though the precipitate is believed to be the result of coulombic interactions between the two particles and the red-shift the result of the associated ligand interactions, not being stable in solution prevented further characterization by pump-probe spectroscopy and being able to decisively measure whether electron transfer is observed.

A similar scheme was proposed by Gross *et al.* where they used a metal ion to form small clusters of negatively charged donor-acceptor molecules in which they claim to observe evidence of electron transfer.[102] Their basic scheme is depicted in Figure 3.9 and is argued that it should decrease the surface-to-surface gap over that shown in Figure 3.6 from 2-3 nm to ~1 nm.

Figure 3.9: Proposed ionic complex by Gross *et al*. used to induce electron transfer.[102]

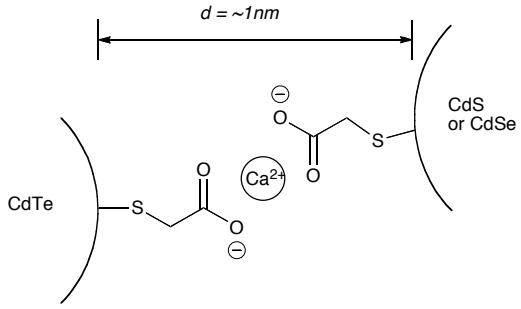

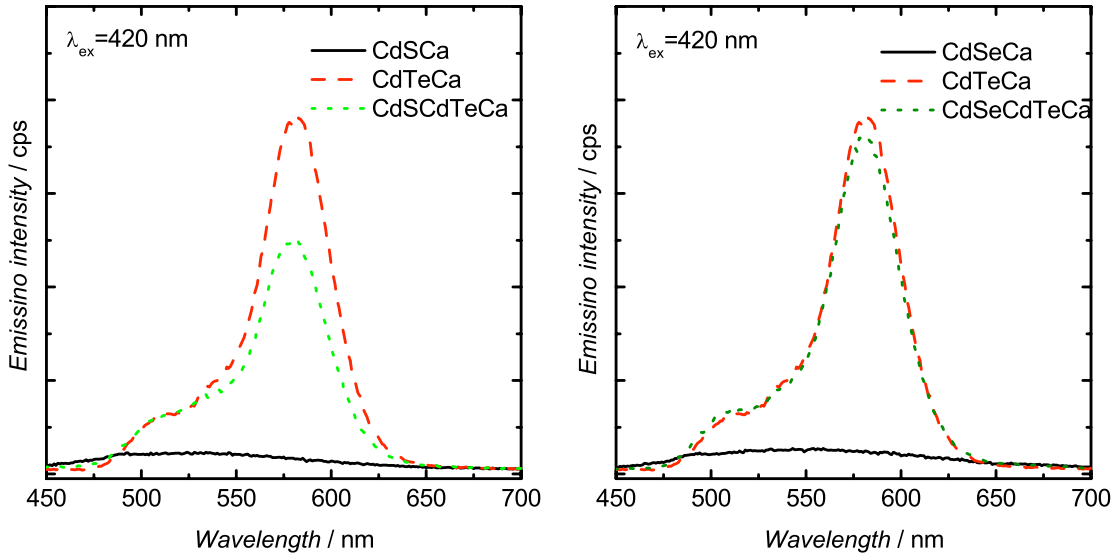

Figure 3.10: Representative emission spectra for negatively charged TGA-CdTe complex formation with TGA-CdS (left) and TGA-CdSe (right) by induced flocculation with Ca^{2+} ion addition. The decreased emission from CdS addition was found to be within experimental error.

Following the same protocol using $CaCl_2$ as a complex mediating ion yielded quite different results from their published data, though it was no less interesting. It was found that TGA-CdTe emission is heavily quenched by the addition of excess $CaCl_2$ to solution (200:1 Ca^{2+}:CdTe) and emission is slightly red-shifted. Addition of equal mole amounts of TGA-CdSe did not show, however, any noticeable emission decrease as reported in the literature. In contrast, the addition of TGA-CdS did yield a 20% decrease in emission intensity for samples with Ca^{2+} though this is within experimental error. Finally, increases in concentration of the quantum dots in this experiment lead to a more rapid precipitation of the complexes from solution. This prohibited the use of this complex formation motif for interrogation by a transmission absorption pump-probe experiment to directly monitor

exciton behavior. Final optical densities on the order of 0.5 are ideal requiring concentrations on the order of >20 μM, about 50-fold the concentration used for the experiments in Figure 3.10.

As an alternative to the electrostatic interactions from the previous two schemes, which did not give suitable materials for pump-probe spectroscopy, an activated acid amide bond formation reaction can be used to selectively and covalently couple the donor and acceptor. As opposed to a simple dithioalkane cross-linking agent as has been used in FRET experiments between tethered CdSe quantum dots,[103] a selective amide coupling prevents the formation of the 50% undesired homomaterial-linked products and removes the necessity of needing to exchange surface ligands with potentially deleterious ligands.

At near neutral pH in water, a carboxylic acid can be activated with 1-ethyl-3(3-dimethylaminopropyl) carbodiimide (EDC), which is used as the water stable hydrochloride. This carbodiimide is stable in neutral to acidic pHs in contrast to the more traditional solid-phase peptide synthesis activating carbodiimides such as N,N'-diisopropylcarbodiimide (DIC) or N,N'-dicyclohexylcarbodiimide (DCC). It has been shown to functionalize amine terminated self-assembled monolayers on a Au surface with MPA-CdSe quantum dots for SPR measurements with good yield.[104] The synthetic scheme adopted for these experiments is shown in Figure 3.11 below, utilizing a neutral HEPES buffer to prevent particle degradation, which occurs at lower pHs. Both nanoparticle stock solutions were initially dialyzed before reaction to remove excess ligands from solution, which compete with surface bound ligands for the EDC activator during reaction with TGA-CdTe or the activated acid with MEA-CdS.

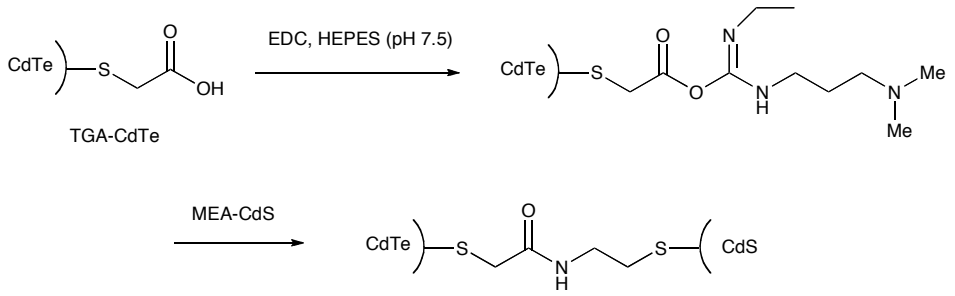

Figure 3.11: Synthetic scheme for EDC mediated amide coupling of a CdTe-CdS donor-acceptor complex.

For the reaction, an excess of EDC was used – about 5 to 10-fold the concentration of TGA-CdTe. After reaction for 15 minutes, MEA-CdS was added and the reaction mixed rapidly for 45 min. After the reaction an aliquot was removed, labeled and stored in a glass vial. To the remaining coupling reaction, ~2 µL TGA was added to effect an incomplete ligand exchange with the MEA-CdS to help prevent aggregation as was seen in the electrostatic experiments above. The emission spectrum from CdTe in the coupled products showed no significant change in shape or intensity after coupling. Conversely, the addition of TGA shifted the emission to the blue about from 620nm to 592 nm (0.1 eV) with appreciable broadening. This shift is consistent with TGA binding free surface sites on CdTe and is consistent with control experiments on CdTe dialyzed particles which experience a simple red-shift after dialysis and then return with addition of suitable ligand. After allowing the aliquot without the additional TGA to sit for 12 hours, a dramatic flattening and broadening of the absorption profile is observed, discernable by eye by the deterioration of the CdTe orange/brown color. Interestingly,

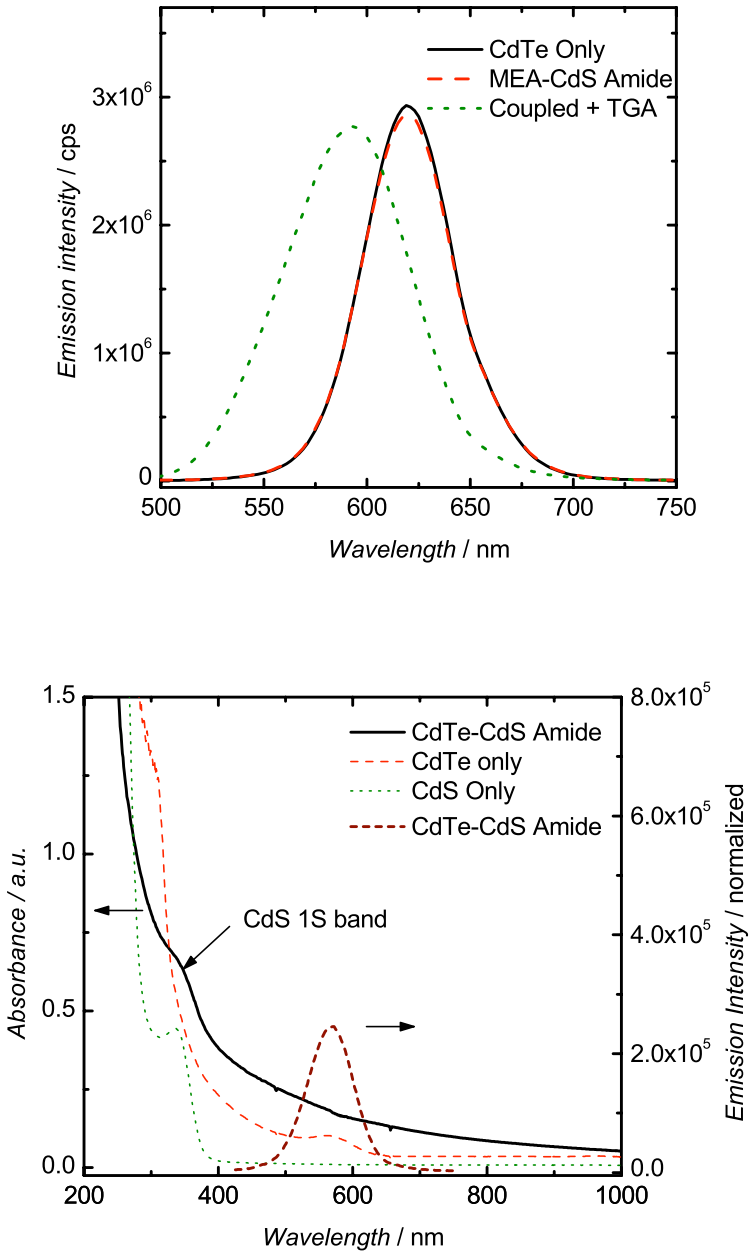

Figure 3.12: (above) The emission of amide coupled CdTe-CdS showed no change in emission after coupling. After addition of TGA to stabilize the product the emission shifted 0.1 eV to the blue. (lower) After reacting for an additional 12 hours, the absorption profile of the product showed a dramatically changed CdTe absorption profile with strongly blue-shifted emission (0.2 eV).

the emission also shifted a dramatic 0.2 eV (50 nm) to the blue and decreased in intensity by 10-fold. This emission profile is indicative of well-passivated CdTe quantum dots and is directly on top of the band edge absorption band (see Figure 3.12 above). However, the absorption profile is heavily broadened suggesting either particle degradation or electronic coupling of CdTe to a broad range states in CdS. The former is less likely as such bulk material would precipitate out of solution. It is possible that this is the result of electronic coupling between the CdTe and CdS, or the result of an electron transfer event, consistent with the 10-fold decrease in emission efficiency. However, no electron transfer emission band was visible to the red as is traditionally observed though it may be significantly red-shifted as the absorption profile is strongly broadened.

Though encouraging, these materials remained difficult to work with as they had relatively short shelf lives as a result of the need to dialyze the starting materials. Dialysis of TGA-CdTe and MPA-CdTe was inconsistent in that it often led to product precipitation or stochastic spectral changes. Because of these inconsistencies, an alternative approach for generating heteromaterial complexes was pursued.

It should be noted that the approaches explored above proved ineffective for carrier separation studies as they lacked long-term stability or any direct evidence of electron transfer. The experimental details have been included as a reference should further studies pick up on these chemistries.

3.2.2 Heteromaterial organometallic nanostructures

Organometallic methods of quantum dot synthesis are significantly more capable than aqueous methods and offer subtler control over particle morphology and desirable optical properties. [56, 57, 105, 106] Since the first reported colloidal synthesis,[41] an enormous amount of work has been done to move to less toxic and safer precursors giving the chemistry improved scalability.[107] Nanoparticles and rod-like structures of CdS, CdSe and CdTe are easily fabricated with diameters of 4-10 nm, which is slightly larger than those accessible by the aqueous conditions described above. Furthermore, better surface passivation is observed with quantum confinement based control over emission from CdSe and CdS which aqueous synthesis does not provide (see Figure 3.3 and Figure 3.4 above). A number of simple schemes can be devised to create the heteromaterial type-II junction necessary to yield spatial charge carrier separation in a colloidal solution suitable for characterization by differential pump-probe spectroscopy. This section will highlight two different schemes that we envisioned to solve the problem, and finally detail the synthesis of a heteromaterial structure that is both suitable for the solution phase experiments and also that can be made into photovoltaic devices.

The first of the two schemes that we proposed was an analogous approach to the EDC coupling used in aqueous syntheses above. “Click”-chemistry approaches to covalent molecular tethering[108, 109] have become heavily used in materials,[108] medical, [110] biomolecular targeting[111, 112] and polymer[113, 114] sciences largely because of the facile chemistry, relatively benign reaction conditions, the method’s robustness and lack of

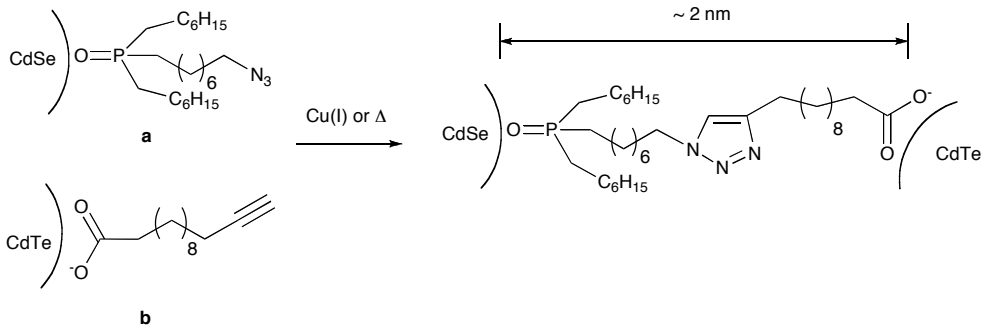

Figure 3.13: Synthetic scheme using Cu catalyzed [2+3] cycloaddition azide-alkyne coupling to selectively link CdTe and CdSe quantum dots.

coupling side-products. Despite the prolific use in other fields, very little work has been done to examine the use of such chemistry with the organic ligands stabilizing semiconductor quantum dots. Briefly, Binder *et al.* have used Cu-mediated "click" chemistry to attach small molecules through the 1,3-dipolar alkyne-azide cycloaddition[115] while Voggu *et al.* have used it to link CdSe quantum dots to Au nanoparticles.[116] The "click" chemistry approach for coupling different II-VI QDs together offers a number of merits. As with the EDC coupling approach in water, the cross-linking would be covalent and specific for heterogeneous coupling. In contrasts to aqueous environments, the reactions are between non-charged ligands, the solvent conditions can be easily modified, the coupling has no by-products that might interact with the surface of the particles, and organic soluble QDs are more easily manipulable and synthetically robust. For these reasons a "click" coupling approach is more promising than the earlier EDC aqueous coupling.

The scheme devised to accomplish this coupling is outlined in Figure 3.13. The reaction uses a azido-trioctylphosphine oxide stabilized CdSe which can be obtained by

ligand exchange of native TOPO capped CdSe particles as previously shown.[115] The commercially available alkynyl organic acid should be stable under the synthetic conditions used to make CdTe with no additional ligand exchange necessary after workup. The cross-linking can be accomplished by preparing a mixture of the purified products and either weak heating or preferably using a Cu(I) catalyst. After the reaction, a simple particle precipitation with an appropriate non-solvent will allow isolation of the semiconductor product and removal of the Cu(I) catalyst.

While this chemistry should facilitate the couplings of interest without the need for deleterious dialysis steps as in the aqueous coupling and utilizes robust chemistry with fewer than 5 total steps, the particles will still be extremely far apart with surface-to-surface separation on the order of 2 nm. For this reason we chose instead to first pursue an alternative approach of directly growing donor and acceptor systems within the same particle to generate materials suitable for solution phase characterization of interfacial electron transfer. The merits of the “click” chemical approach were highlighted because it is believed that they should be pursued in the future as the chemistry has not been explored in the literature and would offer important opportunities for bottom-up fabrication techniques based on semiconductor quantum dots and quantum rods.

Heteromaterial quantum rods

As an alternative approach to a ligand directed coupling between two quantum dots, directly growing a second nanostructure on a single face of a seed crystal offers the

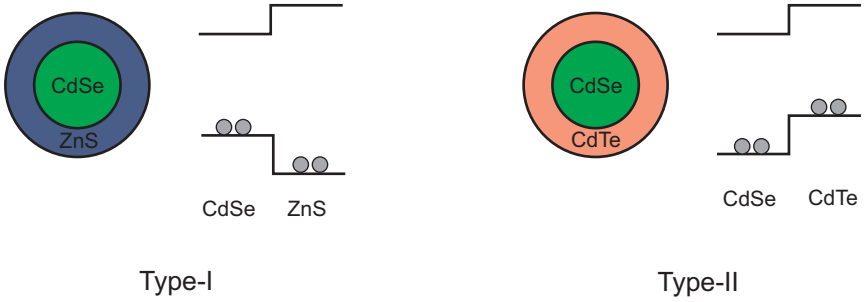

Figure 3.14: Core/shell quantum dots can have two different band structures. ZnS capped CdSe are the most commonly studied particles and have a type-I band structure with the both photogenerated charge carriers being isolated to the core of the system. Conversely, in a type-II structure the hole and electron are spatially separated.

ability to put a donor and acceptor dot in atomically close proximity. Heteromaterial structures are not novel in their synthesis with CdSe/ZnS core/shell QD structures (see Figure 3.14) being one of the most studied materials in the field.[42] In this case a type-I band structure leads to both carriers being confined to the core material. This results in an improved PLQE from better passivation of CdSe surface sites by the semiconductor shell vs. the organic ligand shell. Similarly, type-II structures can be synthesized by choosing a different material than ZnS, such as CdTe for a shell, in which case the photogenerated electron is located in the core and the hole in the shell.[43, 98] However, using conventional phosphine oxides and long chain carboxylic acids as surface stabilizing ligands leads to a nearly uniform coating of the material and therefore a core that is isolated from solution. In order to make these materials suitable for photoelectronic applications, both materials need to be conceivably interfaced in order to pull the charge carriers into an electronic circuit.

To accomplish this for a desired heteromaterial structure, a ligand that directs asymmetric growth of a second material on only a single face is needed. In 2001, Peng *et al.* observed that TDPA facilitated exactly this reaction , growing rod based structures. It was observed that as growth on the chalcogenide-rich <001> face was significantly faster than on the cadmium-rich faces.[107] This chemistry has been used extensively to grow single material QRs. However, recently the same chemistry was expanded to grow CdSe/CdTe heteromaterial rod structures by following the nucleation and growth of a seed rod with the addition of a second chalcogenide in the presence of excess cadmium precursor.[117, 118] The CdSe/CdTe structures (see Figure 3.15) are ideal for electron transfer dynamics studies as they put the donor and acceptor in atomically close proximity and exhibit an optically active charge separation transition (see optical spectra in experimental details below). Furthermore, the chemistry involved in their synthesis is well established, offering good control over particle dimensions, uses elevated temperatures with traditional high-boiling solvents, and utilizes strong ligands and high reaction concentrations to direct near monodisperse crystal growth. As organic soluble

Figure 3.15: Asymmetric heteromaterial quantum rods (hQRs) are ideal structures for studying photoinduced charge carrier spatial separation in materials where both carriers are electronically accessible. The schematic below illustrates the hNR structure and growth direction during synthesis off a single face of the CdSe seed crystal.

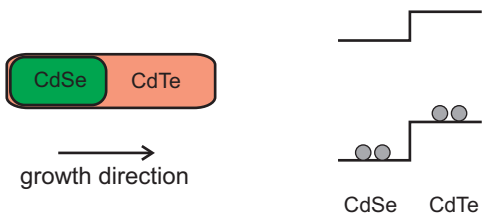

particles, their processing and purification is relatively straightforward using repeated non-solvent precipitation and redispersion in either hexanes or toluene. Finally, the materials are more photostable in air than their aqueous counterparts, making them suitable for the high pump-fluences used to acquire a good excited state transient absorbance signal. Based on these properties, the hQR materials were selected to probe transfer dynamics using our pump-probe experimental methodology and gain a better understanding of the separation dynamics and their effectiveness as materials for photovoltaic devices.

Experimental – Organometallic hNR synthesis

The synthesis of CdSe/CdTe hNRs was accomplished by modification of published procedures[117, 119] utilizing an excess amount of cadmium precursor during growth of the CdSe seed to effect higher aspect ratios[105] as well as leave additional material for the growth of CdTe.

In a representative synthesis, the cadmium precursor was prepared by combining, CdO (~125 mg), TOPO (~3 g, 99% pure), and TDPA (400 mg, >98% pure) in a 3-neck round-bottom flask with a magnetic stir bar. The flask was then outfitted with a water-cooled condensing column, a thermometer and a rubber-septum and connected to a vacuum/inert gas dual-manifold. The mixture was then heated to 80-100 °C for 2-3 hr under high-vacuum to remove dissolved H_2O from the TOPO solvent as well as degas the mixture. After back filling with either Ar or N_2, the Cd-$(TDPA)_2$ complex was formed by reaction at 320-340 °C under positive pressure to give a clear solution. After the

reaction, the solution was cooled to 110-120 °C and put under high-vacuum for 1 hr to remove the evolved H_2O from the complex forming reaction. Typically, the reaction needs to be put under vacuum at ~150-170 °C as it cools to prevent significant foaming of the soapy solution indicative of the change in viscosity after reaction of the TDPA with CdO. This last degassing step was found to not be necessary and many published reports run a similar reaction without it.

The selenide and telluride precursors were prepared by reduction of Se (~35 mg) and Te (~42 mg) metal powder with ~1.5 mL of trioctylphosphine (TOP – 99%) in separate vials. The sealed vials were magnetically stirred and usually cleared up to the reduced product in 15 minutes. The TOP-Te reduction needed weak heating (~50-80 °C) to complete in this time otherwise it took >1hr. A mole ratio of Cd:Se and Cd:Te of less than 2:1 for each precursor was used to keep the Cd precursor in excess.

After drying the $Cd(TDPA)_2$ precursor for 1 hr at 110 °C, the reaction mixture was backfilled with N_2 and heated to 330 °C under a slight positive pressure. To the rapidly mixing solution, the TOP-Se precursor was rapidly injected via syringe and the temperature stabilized at 290 °C. A color change after a few seconds indicated the formation of the CdSe particles. This formation usually occurred between 5 and 120 seconds. After heating for 4-8 minutes depending on the particle diameter size desired, a small aliquot of the seed was removed and the TOP-Te rapidly injected via syringe. The colored solution changed to dark brown indicating the growth of the CdTe particles. Aliquots of 1-2 mL were removed via syringe at the desired times (usually 4-10 minutes) and the products were precipitated from the TOPO solution with anhydrous MeOH. The precipitate was separated from excess ligands and TOPO solvent by centrifugation

followed by decanting off the supernatant and dissolving the quantum rods in toluene. MeOH precipitation was repeated two more times to help purify the samples before characterization. It is important to note here that the optical spectra can be measured by simply dissolving the TOPO/product mixture in toluene. It was found that higher PLQE values are obtained this way and many groups follow this protocol. However, for the presented experiments, a full purification was performed as excess TOPO caused significant scatter and higher signal-to-noise ratios in the pump-probe experiments. Figure 3.16 and Figure 3.17 below show representative optical spectra of the materials and a TEM micrograph of the final hNR products.

Figure 3.16: Representative absorbance and emission spectra of a CdSe seed crystal used to grow hNRs.

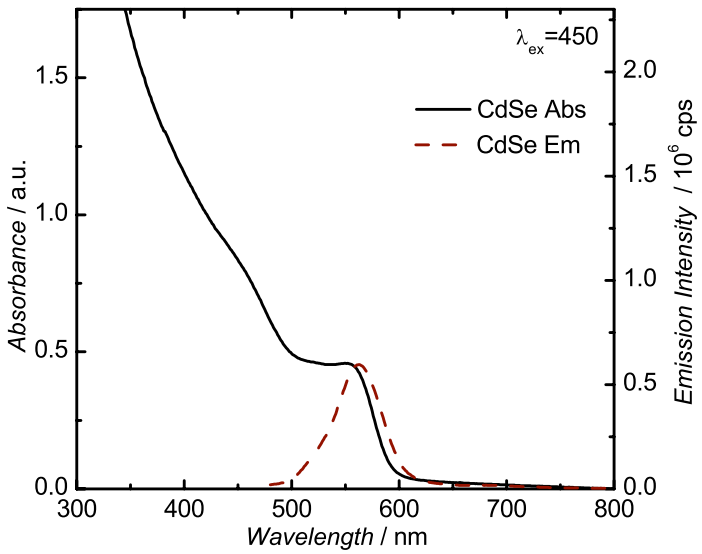

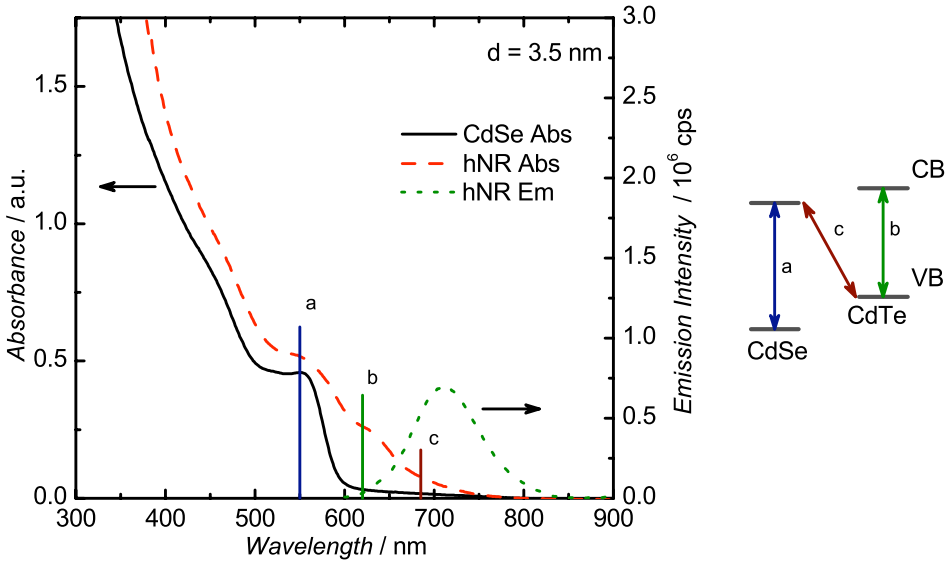

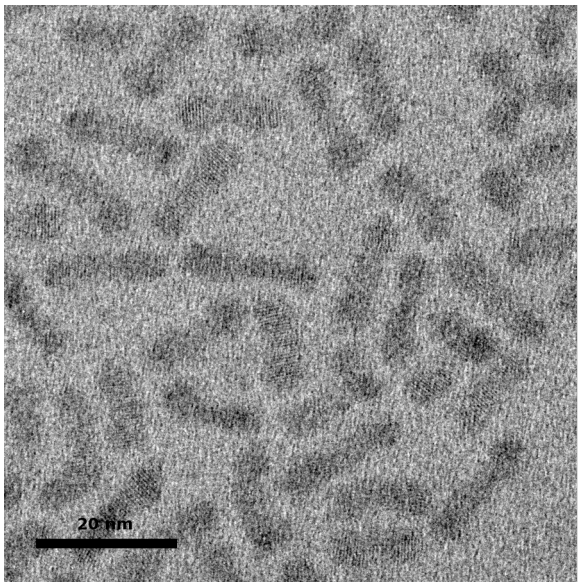

Figure 3.17: (above) Optical spectra of a representative hNR sample showing the CdSe and CdTe 1S band edge absorption transitions as well as an allowed transition to a charge transfer state (CT) with corresponding photoemission from this state. (below) A TEM micrograph showing the hNR structures that are made from the protocol described above.

3.3 Electron transfer dynamics

Pump-probe transient absorbance spectroscopy offers a unique ability to study charge carrier dynamics in hNRs. This experimental technique has been used extensively over the past decade to study exciton dynamics in semiconductor quantum dots and quantum rods on the sub-ps timescales.[46, 64, 97, 120-123] A typical transient signal is presented below for a CdSe QD showing a strong state-filling induced bleaching signal at the ground state 1S transition as well as weaker signals from an energy transitions from deeper holes. The states are assigned according to the envelope quantum number of the hole states involved. Here, the $CdSe_{1S}$ transition, sometimes referred to simply as 1S, corresponds to the 1S(e)-$1S_{3/2}$(h) transition. Likewise the 2S transition corresponds to the 1S(e)-$2S_{3/2}$(h).[47]

Figure 3.18: Transient spectra of CdSe quantum dots showing bleached ground state transitions.

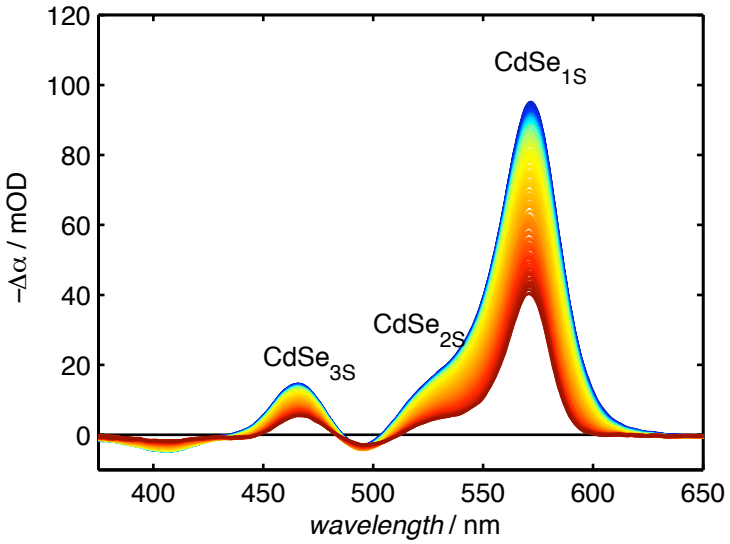

The absorption changes for the state filling bleach can be found according to:

$$\Delta\alpha(h\omega) = -\sum_i a_i G_i(h\omega - h\omega_i)\left(n_i^e + n_i^h\right) \tag{3.1}$$

where a_i is the area of the transition i, proportional to the oscillator strength, $G_i(h\omega - h\omega_i)$ is the unit area profile of the transition, and $n_i^{e/h}$ is the occupation number of the electron and hole states respectively involved in transition i.[47, 124] Because of the high degeneracy of the valence band, and the higher mass of the holes (m_h/m_e ≈ 4-9) leading to a higher density of valence band levels, the occupation numbers of electron states are much larger than for hole states (i.e. $n_i^e >> n_i^h$). The result is that these state-filling induced bleaching signals are dominated by signals proportional to electron density and can be used to monitor directly electron dynamics.

3.3.1 Electron transfer dynamics in 3.5 nm heteromaterial nanorods

A large library of different hNR materials ranging in rod diameter to differing aspect ratios has been studied and electron injection dynamics extracted. To first introduce the findings from our experiments, I will go through the characterization of a representative sample in detail and then discuss some of the more general conclusions from examination of many different samples. We have highlighted some of these findings previously.[67]

The materials reported here are 3.6 nm in diameter and 10-15 nm in length with CdSe seeds of the same diameter and 6-8 nm in length as characterized by TEM. The absorbance spectrum was shown above in Figure 3.17 on page 69 and exhibits three important absorption bands. The first two bands – identified as a and b – correspond to

the lowest energy 1S transitions of CdSe and CdTe (570 nm and 620 nm respectively). The third feature (c) is a broad peak at >670nm corresponding to the CT band where the electron and hole are spatially separated between the two materials. This band is not present in mixed solutions of CdTe and CdSe NRs. Comparison with the absorption spectrum of the seed material identifies the CdSe 1S transition in the hNR spectrum and suggests that the CdSe NRs do not grow during the CdTe deposition stage. The absorbance spectrum of CdSe does not have a relatively sharp 1S transition indicative of a small degree of size variation within the sample, estimated to be between 0.2 and 0.3 nm. This is consistent with measurements by TEM where the variance was found to be 0.2 nm.

In order to isolate dynamics contributions from electron transfer, the sample needs to be excited at the smaller of the two material band gaps ($E_{g,CdTe}$= 2.00 eV, $E_{g,CdSe}$= 2.18 eV). This effectively eliminates any population of the $CdSe_{1S}$ state where an electron has been excited from the valence band of CdSe and thus ensuring that any signals corresponding to an electron in the CdSe-1S(e) conduction band has originated from an electron transfer event. Optical pumping of the hQRs at 620 nm leads to the formation of two distinctly different excited states, i.e. $CdTe_{1S}$-CdSe where one electron has been promoted from the valence band edge of CdTe to the conduction band edge of CdTe – simply a photoexcited CdTe* state – and $CdTe^{+}$-$CdSe^{-}$ where one electron has been promoted from the valence band of CdTe to the conduction band of CdSe – a charge transfer state. Figure 3.19 below illustrates these states and identifies three optical transitions that are observable as state-filling induced spectral bleaching.

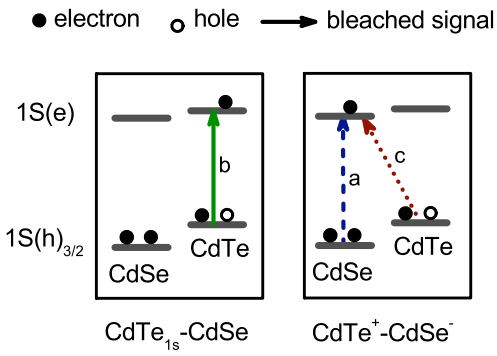

Figure 3.19: Energy level diagram showing two electronic states possible from photoexcitation of the smaller band-gap CdTe electron donor.

These three state-filling signals are the interfacial CdTe/CdSe CT transition (~ 680 nm), and the lowest energy 1S transitions of CdTe (620 nm) and CdSe (550 nm). As discussed above, the bleaching signal's amplitudes are proportional to the electron state occupation number and thus their signal behavior corresponds to electron dynamics. It follows, then, that the state-filling signal at 550 nm from the CdSe-1S bleach and the CT bleach result from the same electron in the CdSe-1S conduction band while the bleach at 620 results from an electron in the CdTe-1S(e) electron state. Therefore, by monitoring the temporal evolution of the three bleaching signals one can probe the time-dependent populations of the (optically prepared) $CdTe_{1S}$-CdSe and $CdTe^{+}$-$CdSe^{-}$ states and monitor the corresponding transfer of electron population from the $CdTe_{1S}$ excited state to that of CdSe.

The pump pulse was tuned to ~625 nm, i.e. just to the red-side of the 1S transition of CdTe. In order to minimize the effects of multi-exciton generation on cooling dynamics and avoid Auger-type processes, a low-intensity pump pulse was used such that the

average number of excitons per particle, $\langle N_{ex} \rangle$, was less than 0.05. This value was calculated by $\langle N_{ex} \rangle = \sigma_i \cdot j_\lambda$ where j_λ is the excitation pulse fluence in photons per cm^2, and σ_i is the absorption cross-section at the excitation wavelength, which can be calculated from the molar extinction coefficient. The extinction coefficient was determined based on the band-gap energy based on a previously published empirical fit[125] and found to be 180000 $M^{-1} \cdot cm^{-1}$.

Figure 3.20 displays the temporal evolution of the hNR pump probe spectrum which consists of the three separate bleaching bands with maxima at 570 nm, 620 nm and ~680 nm. As pointed out above, these bands are the state-filling signals that represent the populations of the $CdTe_{1S}$-CdSe excited state and the $CdTe^{+}$-$CdSe^{-}$ charge separated state states. It is immediately observable from the transient evolution that the CdSe conduction band is populated instantly upon selective photoexcitation of CdTe, indicating a transfer process on the sub 100-fs timescale, the temporal resolution of the experiment. To ensure that the strong signal was not from the near edge absorption of CdSe a control was done with a mixture of homomaterial CdTe and CdSe nanorods of similar dimensions (d = 3.5 nm, l = 5-10 nm) in a 1:1 mole ratio which yielded spectra dominated by bleaching of only the $CdTe_{1S}$ transition, without any signal from the CT band or the $CdSe_{1S}$ band.

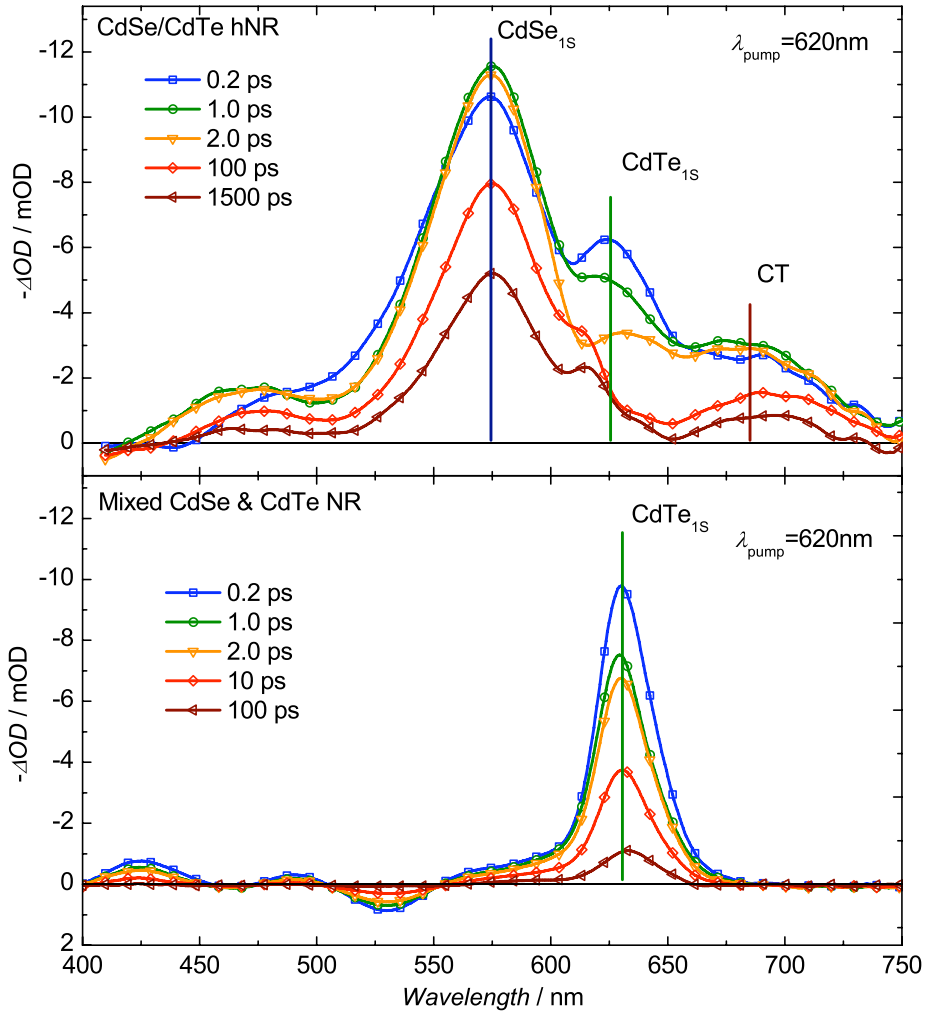

Figure 3.20: Pump-probe spectra of (upper) CdSe/CdTe hNR and (lower) mixed CdSe and CdTe nanorods at selected time points following photoexcitation of CdTe with a 45 fs 620 nm pump pulse. Excitation of CdTe in hNRs leads to a strong state filling induced bleaching band from electron injection into the 1S(e) electron state of CdSe (570 nm and 680 nm). In mixed colloids of similar sized CdSe and CdTe no state-filling of the CdSe electron level is observed.

Plotting the normalized differential absorption signal at the maximum of the $CdSe_{1S}$, $CdTe_{1S}$ and CT bands as a function of time reveals an ultrafast decay of the $CdTe_{1S}$-realCdSe population as identified by the $CdTe_{1S}$ band. On the same timescale this decay is accompanied by a corresponding increase of the $CdSe_{1S}$ and CT state filling signals, which are assigned to the $CdTe^{+}$-$CdSe^{-}$ state. It is noteworthy that the $CdSe_{1S}$ and CT bleaching bands exhibit nearly identical buildup dynamics during the first 2 ps after excitation as is expected since they both are proportional to the electron occupation number of the CdSe 1S(e) conduction band. Following a sub-100fs population buildup on the timescale of the pump pulse, a second rise with a time constant of ~400 fs is observed. Similarly, a fit of the $CdTe_{1S}$-CdSe population decay at 620 nm reveals a time constant of ~500 fs, a value that is within the confidence of the CT rise time. The similarity in the rise times of the charge separated $CdTe^{+}$-$CdSe^{-}$ state on the one

Figure 3.21: Single wavelength differential absorption changes over the first 2 ps after excitation showing a growth in CdSe 1S(e) population on a 400 fs timescale.

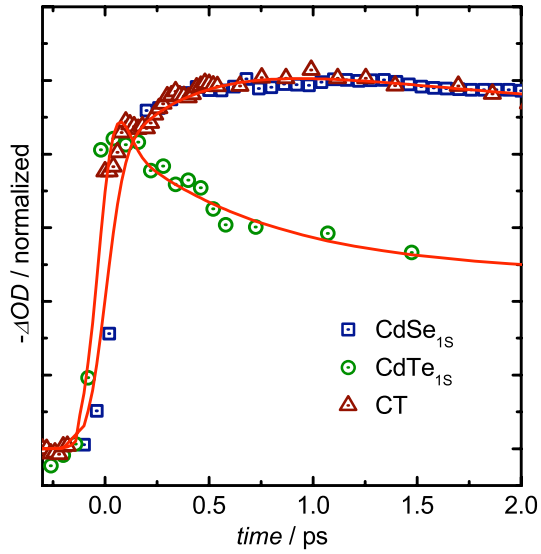

hand and the decay time of the electron donor $CdTe_{1S}$-CdSe state on the other, is consistent with the injection of an electron from the CdTe conduction band into the conduction band of CdSe. The 400 fs buildup only accounts for about 20% of the total signal amplitude indicating that most of the electron population in the CdSe conduction band level arrives on the timescale of the pump pulse. This quasi-instantaneous buildup can occur by either the direct optical electron transfer of an electron from the valence band of CdTe to the conduction band of CdSe without forming the $CdTe_{1S}$-CdSe intermediate state or via the unintentional excitation of a CdSe valence band electron. Since the pump wavelength (625 nm) does not overlap the $CdSe_{1S}$ transition – see Figure 3.22 for control experiment – it follows that direct optical carrier transfer takes place upon photoexcitation. Consistent with this conclusion is the presence of a (weak) CT absorption band in the steady-state UV/VIS spectrum Figure 3.17 on page 69 as well as the state-filling bleaching band.

Figure 3.22: Control experiment showing weak CdSe-seed signal when pumped at 625 nm.

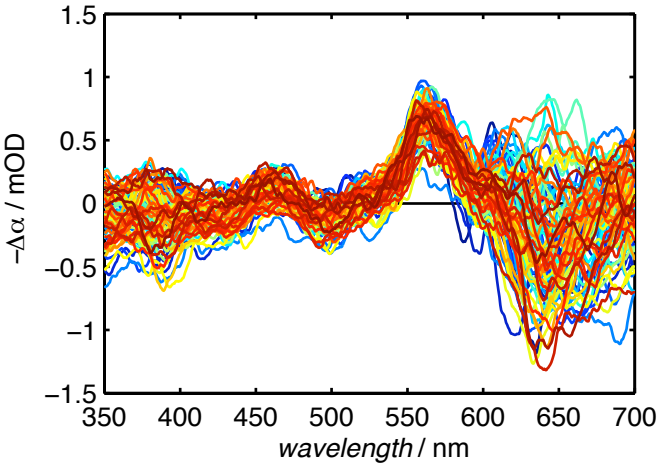

It may be important to consider that following the formation of the CT state by direct optical promotion from CdTe, hole-transfer *to* the CdSe valence band would yield a CdSe excited state and the same bleaching signals observed. This transition, however, is endothermic in a type-II structure and thus energetically unfavorable. While electron-hole couple Auger-like relaxation dynamics might be able to stimulate such a transfer, the low pump energy and intensity used in these experiments should preclude such complications. This consideration again suggests that the 400 fs growth in signal originates from an electron injection event. Furthermore, since the dynamics of the CT and $CdSe_{1S}$ bands are coupled, the optical transition at >680 nm must involve at least one electron or hole state from the CdSe particle and cannot be associated with an optically allowed transition to a shallow trap-state within the CdTe band gap. If the broad, red-shifted emission observed were from a trap-state then it would involve states confined within the CdTe band structure and not contribute to the CdSe signal.

Following similar buildup dynamics, the $CdSe_{1S}$ band exhibits a 280 ps decay while the CT band decays with a 200 ps time constant (shown in Figure 3.23). While this discrepancy could simply be attributed to the excitation of a small fraction of CdSe, Figure 3.22 shows this contribution to be less than 5% of the total signal. Curiously if the dynamics of the CT band were monitored between 690 and 700 nm (instead of 685 nm) this discrepancy in the time constants was less pronounced. On the other hand, monitoring the differential absorption dynamics at wavelengths shorter than 685 nm resulted in a larger discrepancy in the two time constants. Based on this observation, it is believed that the difference in dynamics is the result of spectral inhomogeneities in the

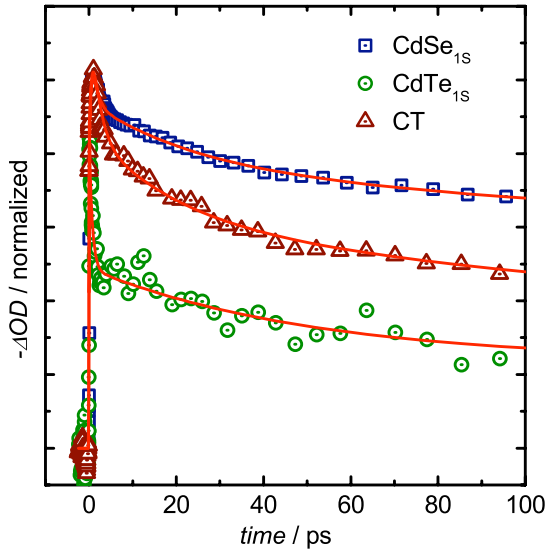

Figure 3.23: The transient differential absorption signal of the CT band and the $CdSe_{1S}$ differ in their 100 ps decay component. This difference is attributed to inhomogeneous broadening from overlap of the CT absorption band with other transient signals.

state-filling induced bleaching signal due to spectral overlap with the $CdTe_{1S}$ band and other positive signals. Thus, at wavelengths closer to the $CdTe_{1S}$ band, the spectrum is more affected by the decay of the $CdTe_{1S}$ population. Furthermore, as detailed previously,[119] the dynamics involved in carrier relaxation are sufficiently complicated that strong deviations from the simple model used here are not surprising.

With an injection time of 400 fs, the interfacial electron transfer event in CdSe/CdTe hNR occurs more than 500 times faster than previously believed[119] and on a time scale that is competitive to the ultrafast relaxation dynamics observed in type-II quantum dots.[45, 46] The observed timescale is similar to that of electron-transfer in model dye-sensitized semiconductor systems,[126-128] hole-transfer across the CdS/HgS interface, and about 3-fold faster than electron transfer at the CdS/HgS interface.[121] The similar

observed kinetics to CdS/HgS can be explained qualitatively by considering the energy overlap of the respective conduction and valence bands.[121] At the CdS/HgS interface, both valence band states are composed of atomic orbitals from S^{2-} giving them more closely matching carrier effective masses[129] and correspondingly, energy overlap, than their respective conduction band electron states. In the type-II CdSe/CdTe hNR band structure, both conduction band levels are composed of orbital contributions from Cd^{2+}. A similar consideration of relative energies suggests that these levels would also exhibit good acceptor/donor overlap resulting in a larger single electron coupling element. By an extension of this analysis, we would expect the hole-transfer process from $CdSe_{1s}$ to CdTe to be slightly slower as a result of less favorable overlap between valence bands states of Te^{2-} and Se^{2-}. This transfer event, however, cannot be isolated from state-filling bleaching signals alone as the hole-transfer dynamics, activated by pumping at or above the CdSe band gap energy, would be mixed in with the electron transfer mechanism and a number of other cooling processes occurring on a similar timescale.

Direct observation of hole dynamics would require probing in the mid-IR since they contribute negligibly to the state-filling bleaching signals. Optical transitions from the $1S_{3/2}$ to the $3S_{1/2}$ hole state are on the order of ~0.4 eV (3100 nm) before splitting, putting them well outside the range of our current optics capabilities. That said, extending the probe capabilities out to this wavelength will be an important step as the work looks to understand these materials spectral response across the entire visible spectrum.

3.3.2 Size dependent electron transfer rates?

One of the exciting features of semiconductor quantum dots is their size dependent optical properties. On these lines, it is also important to examine whether the size tunable band structure yields any size dependence on the electron transfer properties. Qualitatively a decrease in the particle size will affect the 1S(e) electron state of CdTe more dramatically than that of CdSe because of their slight differences in effective masses, and a corresponding decrease in band overlap is expected. Conversely, as particles get larger, better electronic coupling is expected along with a smaller driving force. A more detailed examination of the Marcus approach to this problem is given in Section 3.4. Here, the experimental findings are summarized.

Two samples larger than that discussed in detail above are presented in Figure 3.24 representing hNRs with diameters of 4.4 nm and 6.2 nm. Both samples put the $CdTe_{1S}$ and CT absorbance transitions at near the spectral detection limit of our system. This can be seen dramatically in the 6 nm sample where in the >700 nm range the signal-to-noise ratio is very small and the pump scatter completely saturates out the $CdTe_{1S}$ state-filling signal. However, the deeper hole state transitions blue of the bandgap features can be used to measure the same dynamics if necessary. These state-filling signals blue of the bandgap transitions are usually significantly weaker as a result of the increased degeneracy of the deeper hole states compared to the $1S_{3/2}$(h) hole state. The limitation of doing the dynamics analysis in this spectral range is that the signals in this region exhibit a higher degree of inhomogeneous broadening as a result of overlap of multiple bands. Evidence of such bands can be seen between the 2S and

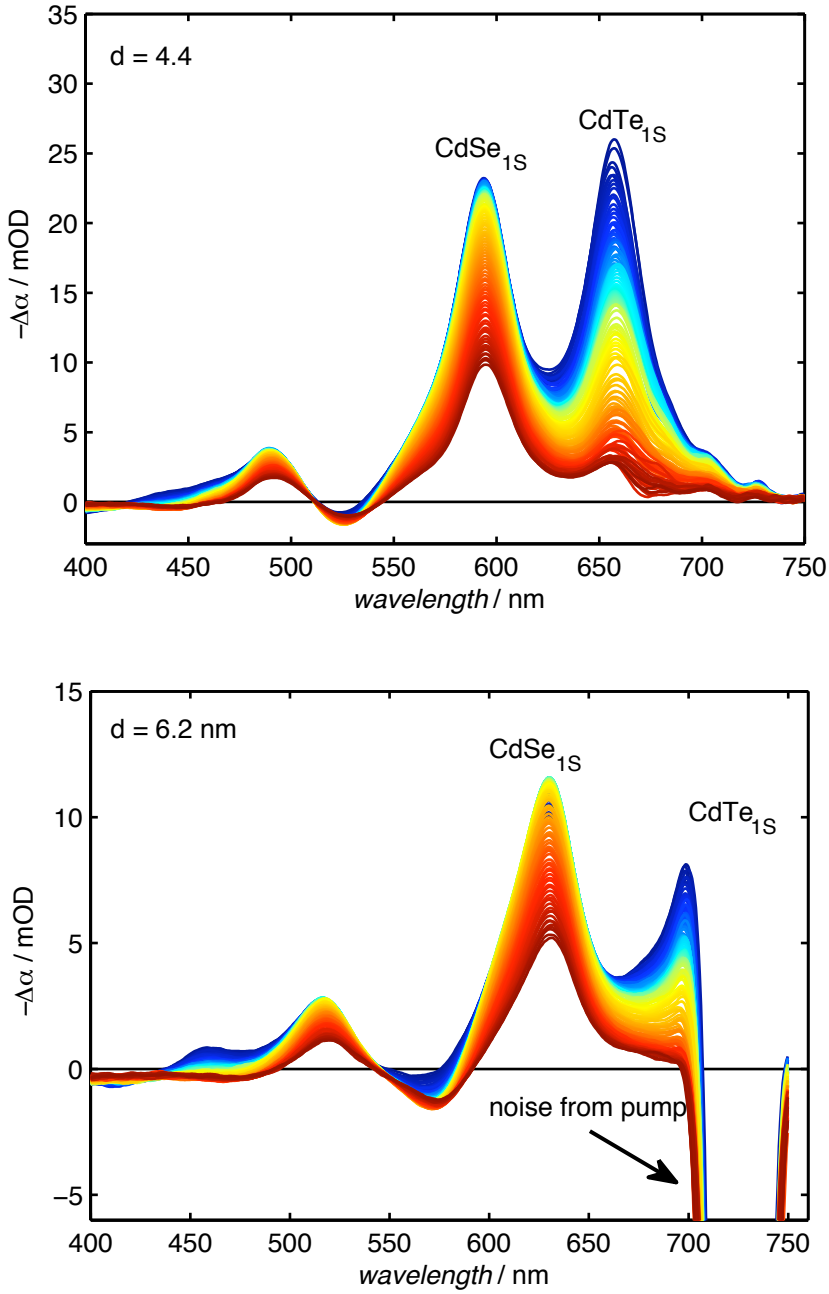

Figure 3.24: Transient absorption signals from 4.4 nm (upper) and 6.2 nm (lower) hNRs. The state-filling signal from the CdTe 1S(e) population in the 6.2nm sample is hidden behind the scatter from the pump pulse. The WLC intensity is weak at wavelengths >700 nm decreasing the signal-to-noise ratio.

3S transitions of the CdSe seed at around 525 nm and 575 nm for 4.4 nm and 6.2 nm respectively.

A fit of the $CdSe_{1S}$ and $CdSe_{3S}$ state-filling induced bleaching signals in the 4.4 nm sample show a build up of 330 fs. Additionally, a fit of the $CdTe_{1S}$ and $CdTe_{3S}$ signals at 655 nm and 455 nm respectively, show a rapid decay with a 460 fs time constant. A similar analysis of the 6.2 nm sample shows an increase in the population of the CdSe-1S(e) electron state on the order of 410 fs. Analysis of the $CdTe_{3S}$ signal at 455 nm shows a rapid decay of 500 fs. Importantly, both the $CdTe_{3S}$ signals are visibly a combination of multiple signals as after 5 ps the signal shows a weak excited state induce absorption band (positive signal).

Analysis of an extensive range of samples with diameters from 2.7 to 6.2 nm shows growths with similar time constants between 230 and 580 fs. The diameter and corresponding measured $CdSe_{1S}$ growth rate is shown in Table 3.1. Importantly, there is

Table 3.1: Comparison of hNR diameters to the electron injection rates showed no correlation between the two parameters.

hNR diameter	$CdSe_{1S}$ population growth rate (fs)
2.7 nm	250 fs
2.9 nm	400 fs
3.7 nm	500 fs
4.1 nm	230 fs
4.4 nm	460 fs
4.5 nm	580 fs
5.2 nm	300 fs
5.6 nm	320 fs
6.2 nm	410 fs

not a general trend for electron injection rate as a function of particle diameter. The injection rates have an average value of 390 fs and a variance of 110 fs based on this sample set. This variance is close to the fitting error of ± 50-80 fs usually observed for these experiments. This suggests that within the experimental error of determination, the injection rates are roughly the same. This assertion can be seen graphically by comparing some of the single wavelength differential absorption signals at the $CdSe_{1S}$ transition during the first 5 ps. Figure 3.25 shows the kinetics of a 3.7, 4.5 and 5.6 nm sample, along with their fitted growth rate constants. The three samples all show very similar kinetics during the first 2 ps though when fit they show appreciably different lifetimes. Based on the error in the fits, it is determined that within the limits of the current experiment, there is no measureable difference in injection lifetimes as a function of diameter.

Figure 3.25: Growth kinetics of 3 selected samples from **Table 3.1** showing similarities in the growth rates across a wide range of particle sizes.

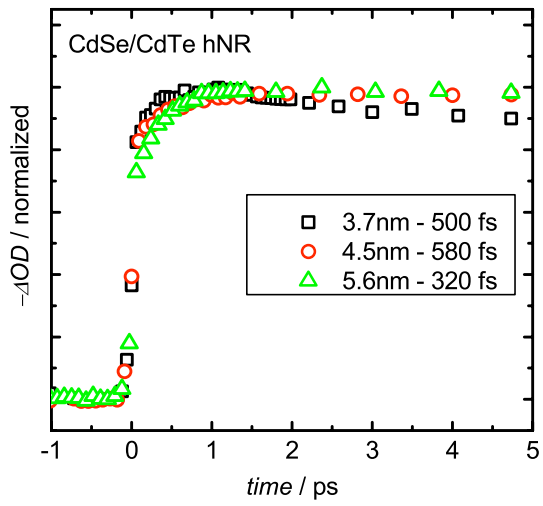

3.4 Marcus analysis

One of the most theoretically interesting predictions about these materials is seen from a simple Marcus framework. Scholes *et al.* have pointed out that the electron transfer process from CdTe-1S(e) to CdSe-1S(e) in these hNRs should be deep in the Marcus inverted region and has presented a detailed analysis of the steady-state optical spectra from a classical adiabatic and diabatic Marcus viewpoint.[130] To corroborate his findings, and examine the presence of Marcus inverted behavior in our samples, I present the detailed analysis of two representative samples below. In characterizing simply steady-state spectra, Scholes *et al.* needed to rely on Gaussian fits of their steady-state spectra to resolve individual transitions, and then perform fits of the extracted Gaussian functions. For samples where the $CdTe_{1S}$ and the CT absorption features are close together, this can be difficult and add considerable error to the analysis. I also show in this section how through the use of our transient differential absorption spectroscopy technique such transitions can be temporally resolved.

3.4.1 Mathematical treatment

In order to determine the classical Marcus parameters and construct a free energy diagram for the electron transfer reaction, the individual bands of the absorbance and fluorescence spectra can be fit according to equations 3.2 and 3.3:

$$a(v)/v \propto \left\langle \left(4\pi\lambda_i k_B T\right)^{1/2} \times e^{-\left(\Delta G^0_{abs} + \lambda_i - hv\right)^2 / 4\lambda_i k_B T} \right\rangle \tag{3.2}$$

$$f(v)/v^3 \propto \left\langle \left(4\pi\lambda_i k_B T\right)^{1/2} \times e^{-\left(\Delta G^0_{em}+\lambda_i+hv\right)^2 / 4\lambda_i k_B T} \right\rangle \tag{3.3}$$

where $a(v)/v$ and $f(v)/v^3$ are the absorption and fluorescence lineshapes respectively of either the CS or $CdTe_{1S}$ bands.[131] The reorganization energies, λ_i (for *i* = $CdTe_{1S}$ or CT) of the transitions can also be calculated as half the Stokes shift of the respective ground state transitions if the peaks are sufficiently resolved. Comparing the two determined values gauges the quality the fitted curves and correspondingly the qualitative accuracy of ΔG^0.

Based on the determined Marcus parameters, a classical non-adiabatic energy diagram of the involved electronic states can be constructed according to:

$$G_i(x) = \frac{k}{2}\left(x - \left(2\lambda_i/k\right)^{1/2}\right)^2 + \Delta G_i^0 \tag{3.4}$$

for the CdTe*-CdSe (*i* = $CdTe_{1S}$) and $CdTe^+$-$CdSe^-$ (*i* = CT) states relative to the ground state where *k* is an arbitrary force constant for arbitrary units of *x*. Based on the generated free energy curves, the reorganization energy of electron transfer (λ_{ET}) from CdTe to CdSe is determined from the optical ground state transitions by using equation 3.4 constructed for CdTe and CT respectively to yield:

$$\lambda_{ET} = \frac{1}{2}k\left(\left(\frac{2\lambda_{CdTe}}{k}\right)^{1/2} - \left(\frac{2\lambda_{CT}}{k}\right)^{1/2}\right)^2 \tag{3.5}$$

which can then be solved for λ_{ET} to give:

$$\lambda_{ET} = \lambda_{CdTe} + \lambda_{CT} - 2\left(\lambda_{CdTe}\lambda_{CT}\right)^{1/2} \tag{3.6}$$

Lastly, the free energy difference driving the electron transfer event ΔG^0_{ET} is simply the difference $\Delta G^0_{CdTe} - \Delta G^0_{CT}$ which can be calculated from the results of spectral fitting using equations 3.2 and 3.3, and should be approximately the difference between the CdTe and CS absorption bands, depending on the broadening from λ_i.

3.4.2 Inverted region behavior

The examination of the absorption spectrum of a selected sample is presented below in Figure 3.26 along with Gaussian fits of the usual three bands of interest, $CdSe_{1S}$, $CdTe_{1S}$, and the CT band. This 3.6 nm sample showed an electron transfer rate of 450 fs, with a traditional transient absorption progression. The absorbance bands

Figure 3.26: Steady state absorbance spectrum showing fitted Gaussian curves at the $CdSe_{1S}$, $CdTe_{1S}$, and CT bands. The fitted curves were used to derive the classical Marcus parameters. The transient differential absorbance spectrum is also shown.

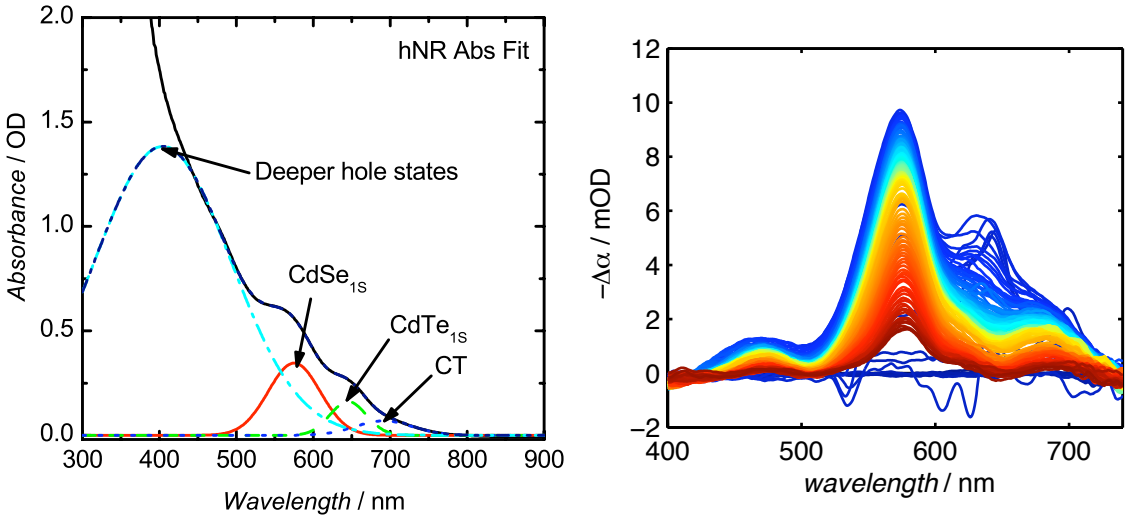

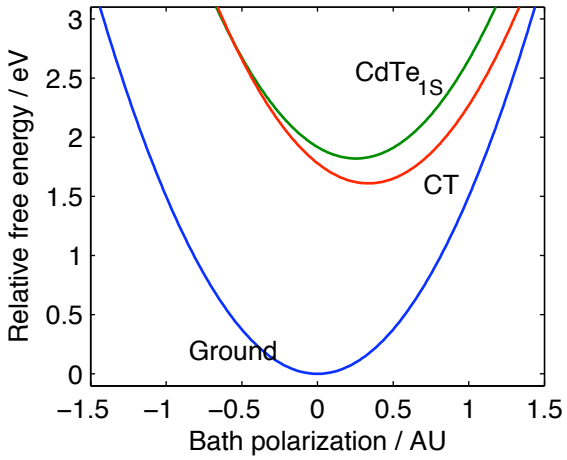

Figure 3.27: The calculated free energy diagram for 3.6 nm hQRs with a reorganization energy of 12 meV and thermodynamic driving force of 210 meV. The energies are plotted relative to the ground state for arbitrary *k*.

identified as the $CdTe_{1S}$ and CT optical transitions were fit to equation 3.2. The corresponding reorganization energies for each state were found to be 0.10 eV and 0.18 eV respectively. These values correspond to a total electron transfer reorganization energy, λ_{ET}, of 12 meV. While this value is exceedingly small relative to the energies usually seen in organic molecules, it is on the same order as already reported for similar materials.[130] The fitted free energies for the respective bands were ΔG_{CdTe} = 1.82 eV ΔG_{CT} = 1.61 eV yielding a net driving force for electron transfer of 210 meV. The corresponding diabatic free energy diagram, constructed for arbitrary *k,* shows the characteristic inverted region scheme where $\Delta G_{ET} > \lambda_{ET}$. This conclusion, first reported by Scholes *et al.*[117, 130] is fundamentally important, as intense efforts have been launched in search of the inverted region, yet only recombination transfer events have been able to yield such behavior.[132, 133] The difficulty with organic samples is that typical

reorganization energies range from 0.5 to 2 eV. Accordingly, it has been difficult to create a suitable driving force for forward electron transfer without encountering a number of other chemical processes inhibiting the reaction. However, with reorganization energies well below 0.1 eV, these materials are potentially ideal for such investigation and for the first time observed inverted region behavior for forward electron transfer.

The time-resolved absorption experiments reported here should be capable of resolving the differences in electron transfer rate as a function of driving force even though the transfer rates observed are already considerably close to the instrument resolution (~100 fs). Since the electron transfer event in this system is strongly in the inverted region, a decrease in the driving force should increase the transfer rate. However, a difficulty with decreasing ΔG_{ET}, even marginally, is that the absorbance and emission features are consequently much closer together and more difficult to resolve from steady-state spectroscopy. However, as the CdTe excited state decays much faster than the bleaching of the CT band, the band position and shape can be extracted from the transient absorption spectrum. Figure 3.28 on page 90 shows the transient signals of a sample where the $CdTe_{1S}$ and CT transitions strongly overlap. After >500 ps, the CdTe-1S(e) electron state is depopulated and the only bleaching that remains is from the CT absorbance feature. Accordingly, by fitting the differential absorption spectra at both an early time point (~0.2 ps) and a late time point (~ 1000 ps), the line shapes of the $CdTe_{1S}$ and CT absorbance features can be directly measured.

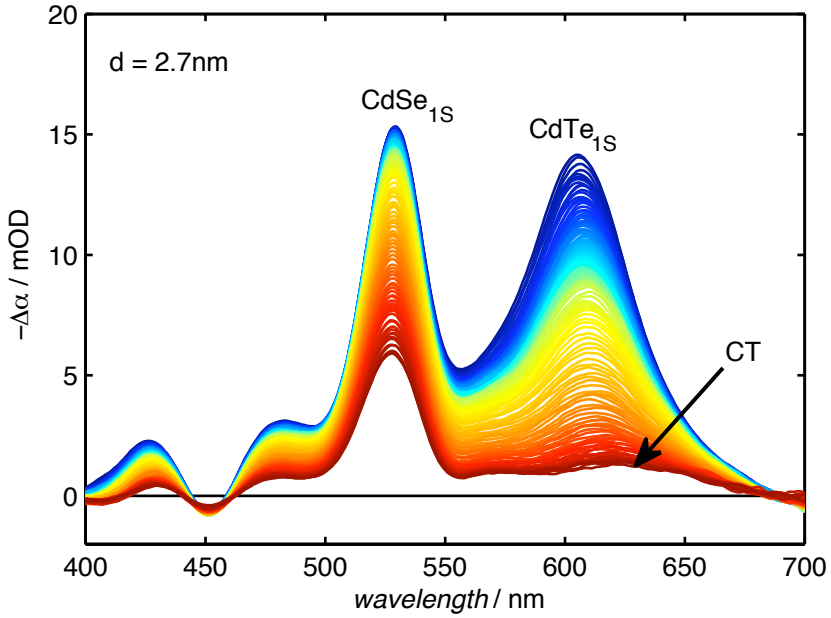

Figure 3.28: Transient absorption spectra of a sample showing strong overlap of the $CdTe_{1S}$ and CT absorption features. Using an early (<2 ps) spectrum and later (>1 ns) spectrum the bands can easily be isolated.

Fits of the lineshapes derived from the late and early transients with equation 3.2 yield reorganization energies of the $CdTe_{1S}$ and CT states of 0.19 and 0.11 eV respectively. From these two values, a reorganization of electron transfer between the two states is calculated to be ~11 meV, close to that of the previous sample. The free energies were measured to be ΔG_{CdTe} = 1.95 eV and ΔG_{CT} = 1.81 eV for a net driving force of -140 meV. Based on the previous analysis, while this forward reaction is still in the inverted region, it is expected that the electron transfer event occurs at a faster rate than the 3.6 nm sample, which had a larger driving force. Indeed, the measured electron transfer lifetime was 260 fs.

While the extrapolation of the $CdTe_{1S}$ and CT bands from this shown sample was possible because of a strong CT absorbance band, most samples prepared with more closely overlapping CT and $CdTe_{1S}$ states, had a relatively weak CT absorption signal. Consequently, at very long times (>1 ns) the larger relative signal-to-noise has prevented additional characterization, as a suitable fit to the absorbance lineshape is not possible. Unfortunately this has prevented the observation of the complete Marcus inverted region as a function of driving force. As synthetic methodologies are refined for the synthesis of these materials it is believed that revisiting this problem will be a fruitful endeavor.

Importantly, the lifetime of ~250 fs is on the same order as exciton-phonon coupling frequencies we recently measured in aqueous CdTe nanocrystals.[134] The measured frequency corresponds to the longitudinal optical phonon at 0.2-0.4 eV. The implications of the fact that the electron transfer is occurring on the same timescale suggests that this system exhibits a very large electronic coupling constant between the donor and acceptor conduction band states and that electron transfer is occurring on the fastest phonon allowed timescales. A more in-depth look at the adiabatic description of this system has been previously reported[130] but sufficient time-resolved data is not available to examine the problem in greater depth.

3.5 Photocurrent generation

In order to connect the results from the electron transfer dynamics studies of this chapter to the greater goal of understanding their role in photon energy conversion, a simple photovoltaic cell has been constructed and studied. The simple device is an

electrolyte based cell with a hNR coated conductive glass working electrode, a high pH sulfide redox couple and a Pt counter electrode. The Na_2S redox couple is used to maintain the stability of the metal-chalcogenide semiconductor. [64, 135, 136] This working electrode fabrication is based on the process used by Gur[58] and is easily modified to use different metal electrode back contacts as has been presented by recent studies on PbS based devices.[60, 61, 66, 137]

3.5.1 Photoelectrode fabrication

Briefly, the fabrication process starts by resuspending MeOH precipitated quantum rods in pyridine followed by a 24 hour reflux to effect a ligand exchange of the TDPA with short pyridine ligands.[58] The ligand exchange material is then separated by precipitation with hexanes, or by rotary evaporation, dissolution in toluene again followed by a MeOH precipitation step. When hexane precipitation was ineffective the ligand exchange was likely incomplete however they were still suitable for device fabrication. The precipitate was then washed 3 times with methanol to remove excess ligands and resuspended in minimal pyridine, with weak heating if necessary. A small drop, ~5-10 µL, of the pyridine solution was put on the FTO surface of the conductive glass electrode and allowed to evaporate to dryness leaving behind a thin film of quantum rods. If the optical density was too small, indicated by being able to see through the film, additional coatings were added to increase the local concentration.

Once a film of desired thickness and optical density was obtained, the electrode was soft-baked on a 200 °C hot plate for 15 minutes to remove any excess pyridine from the film. The quantum rods were then coated in a saturated solution of $CdCl_2$ in MeOH and

again soft baked at 200 °C for 5 minutes. Subsequently, the films were annealed in standard furnace at 500 °C for 15 minutes. After cooling back to RT, a photosensitive epoxy resist film was usually added to insulate the non-photoactive area of the electrode and minimize background currents during analysis. A photoimageable epoxy coating was chosen instead of the S1818 DQ positive resist used for multiplexed gold nanowire arrays[138] because of its increased tolerance of elevated pH environments. A schematic of the working device is shown in Figure 3.29. Typically electrodes were cut to be 5 cm x 1 cm with a photoactive area of 0.34 cm^2 (r = 3.3 mm).

The electrolyte used for characterization was a solution of Na_2S, Sulfur[139] and KOH, each at a concentration of 0.2 M. The added sulfur dramatically impedes the photoresponse to the blue side of the visible spectrum (see discussion below) but gives cleaner *I-V* curves. Removing it from solution does not change the photocurrent density significantly, in contrast to the omission of either the KOH or Na_2S which dramatically

Figure 3.29: Schematic representation of the photoelectrodes made from hQRs. The epoxy coating is optional but leads to cleaner dark current signals during characterization.

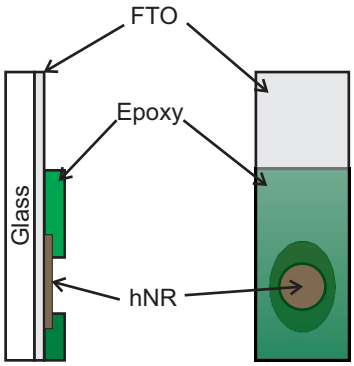

limits the current generation. For most of the measurements presented here, a solution of all three is presented except where noted. For optimization of these experiments, a more careful look at the role of the electrolyte will be necessary.

All electrochemical measurements except IPCE measurements were done on a CH Instruments 600 series potentiostat[140] using a Ag/AgCl 3M KCl reference electrode in a Pt-tipped Luggin capillary filled with a 200 mM NaCl solution. The Luggin capillary is necessary to protect the Ag/AgCl reference electrode from degradation in the sulfide redox solution of the photovoltaic cell. IPCE measurements were performed on a EG&G Princeton Applied Research Model 264 Polarographic Analyzer/Stripping Voltammeter holding the potential fixed at the V_{OC} measured under dark conditions. The incident wavelength was controlled by the excitation dual-monochrometer of a Fluorolog-3 fluorometer with a 5 nm bandwidth. The incident power at each wavelength was measured by performing a scan of the lamp spectrum and subsequent calibration at 480, 500, and 520 nm with an external power meter. This calibration was performed before each measurement to account for fluctuations in lamp power between experiments. Under this experimental setup, the photocurrent measured corresponds to the short-circuit current (I_{SC}) as is routinely used in similar published reports.[64] The corresponding IPCE can be calculated as the number of electrons per unit area, $I_{SC}/(A \cdot q)$, divided by the number of incident photons per unit area, P_λ / E_λ – where P_λ is the power density at the selected wavelength, and E_λ is the energy per incident photon.

Measurements of the cell power conversion efficiency and fill-factor were performed by connecting the photocell to a low resistance current meter in series with an 11 kΩ decade resistor box with < 0.1% variance serving as a variable load. The potential

across the load was measured using a standard multimeter. Under continuous illumination from a Xe arc lamp source with a power density of 100 mW/cm^2, the potential across the load and circuit current was measured as a function of load resistance. Based on the measured potential vs. resistance data the fill-factor and efficiency can be determined. The fill-factor is defined as the ratio of the total power output to the total "theoretical" output power represented by the product of the short-circuit current and open-circuit potential.

$$FF = \frac{P_m}{I_{SC} \times V_{OC}} \tag{3.7}$$

Here the maximum power corresponds to the highest power dissipated by the variable resistor calculated from Ohms law as $P = V^2/R$. The overall power conversion efficiency can be calculated as the ratio of the maximum power output per active area divided by the incident lamp power density.

$$\eta = \frac{P_m}{P_{lamp}} \tag{3.8}$$

3.5.2 Electrochemical characterization

Photoelectrodes were made from a variety of different sized hNRs according to the procedure described above and characterized under illumination by a 150 W Xe arc lamp with a white light fluence of 100 mW/cm^2. The I-V plots of two electrodes made from 2.7 and 3.7 nm hQRs are shown below in Figure 3.30. Photocurrents were measured under both continuous illumination and as well as a chopped light signal to

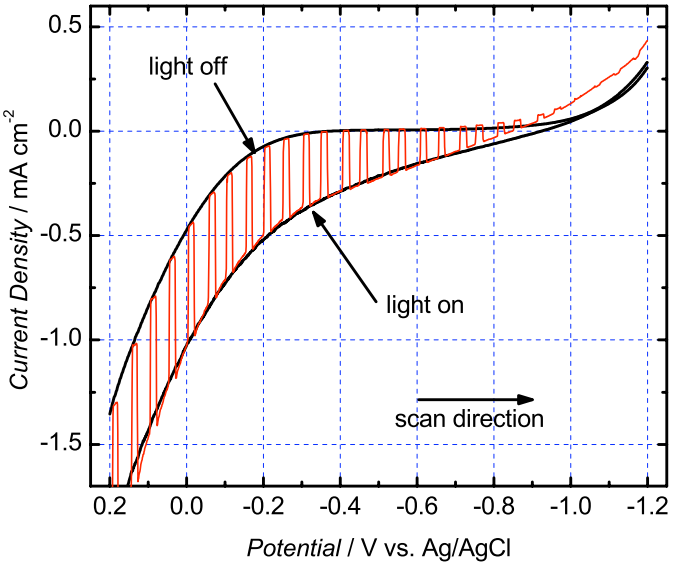

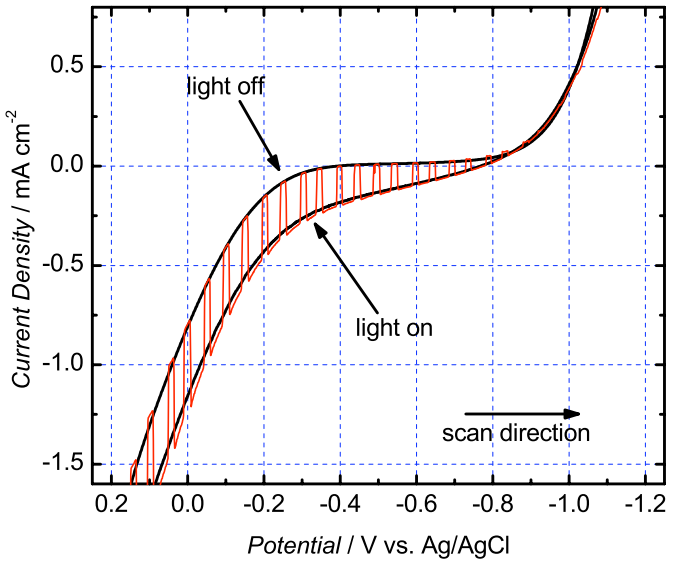

Figure 3.30: Voltammograms of a cathodic polarity linear sweep voltammetry experiment showing the photocurrent densities of two heteromaterial quantum rod photoelectrodes. The thin inside curve shows the cells response to a chopped light source during the scan.

clearly show the electrode behavior under illumination as well as the rapid photoresponse of the electrodes. The curves were measured with a cathodic scan direction (scan toward more negative potentials) as the measured photocurrents more accurately compared with the steady state values at a fixed potential. Anodic scanning polarity led to current-density values that were observed to be artificially high.

The photoelectrodes made form hQR samples showed typical *I-V* traces, which were consistent with relatively low fill-factors. An average current density of 200 μA/cm^2 was observed at the open-circuit potential (V_{OC} = -0.4 vs. Ag/AgCl) for hQR cells; comparable to densities seen in other quantum dot photovoltaic cells,[64] but at least an order of magnitude less than needed to be usable in application driven research. The model cell's fill-factor, as measured by coupling the cell to a variable external load was determined to be 18% on average, consonant with the shallow curvature of the *I-V* trace. Although the calculated fill-factor was encouraging, the overall power conversion efficiency was measured to be only 0.015% on average. This is consistent with the low current densities observed in the photo-electrochemistry experiments.

A plot of the measured currents as a function of external load resistance allows for an estimate of the internal resistance by fitting Ohms Law as expressed in equation 3.9.

$$I = \frac{V_{cell}}{R_{\text{int}} + R_{load}} \tag{3.9}$$

where R_{load} is the independent variable and V_{cell} and R_{int} are fitted variables. This is only valid for a constant photovoltage as a function of cell power delivery; found to be a fair assumption for these cells. Fitting the data to equation 3.9 yielded a determined internal resistance on the order of 2-3 kΩ with a determined photovoltage of 250 mV. This

determined voltage is roughly equal to the average measured open-circuit potential of 280 mV. The high internal resistance is expected for an electrolyte based cell with an FTO electrode. Measured directly, the 2 inch FTO electrode has a resistance of approximately 25 Ω per inch and the electrolyte solution adds ~1 kΩ per centimeter.

Importantly, no appreciable dependence on photocurrent response was observed as a function of hQR size or measured electron transfer rates in the hQR precursors. Photoelectrodes all exhibited roughly the same current densities with an experimental error of ~25%. The large variance is an indication of the irreproducibility of device optical densities between electrodes and not simply variance in material transfer dynamics as electrodes fabricated from the same precursor materials shared the same variance. From the large error, it is expected that without a more controlled fabrication process, it is unlikely that distinguishable differences between photocurrents as a function of transfer dynamics will be observable.

As a control experiment, photovoltaic cells were constructed from single material CdSe and CdTe nanorods and characterized as above. Interestingly, the CdSe-only cells gave a very strong photocurrent, on the same order as that observed from the hNR samples. Within experimental error they were indistinguishable. In contrast, the electrodes made from CdTe showed extremely small photocurrents with efficiencies two orders of magnitude smaller than those of CdSe or hNR photoelectrodes (see *I-V* curves in Figure 3.31 below). The measured FF for electrodes made from CdSe NRs was on average was 15% with a power conversion efficiency of 0.011%. Photocurrents from CdTe based cells were too small to measure consistently. Importantly, the CdTe

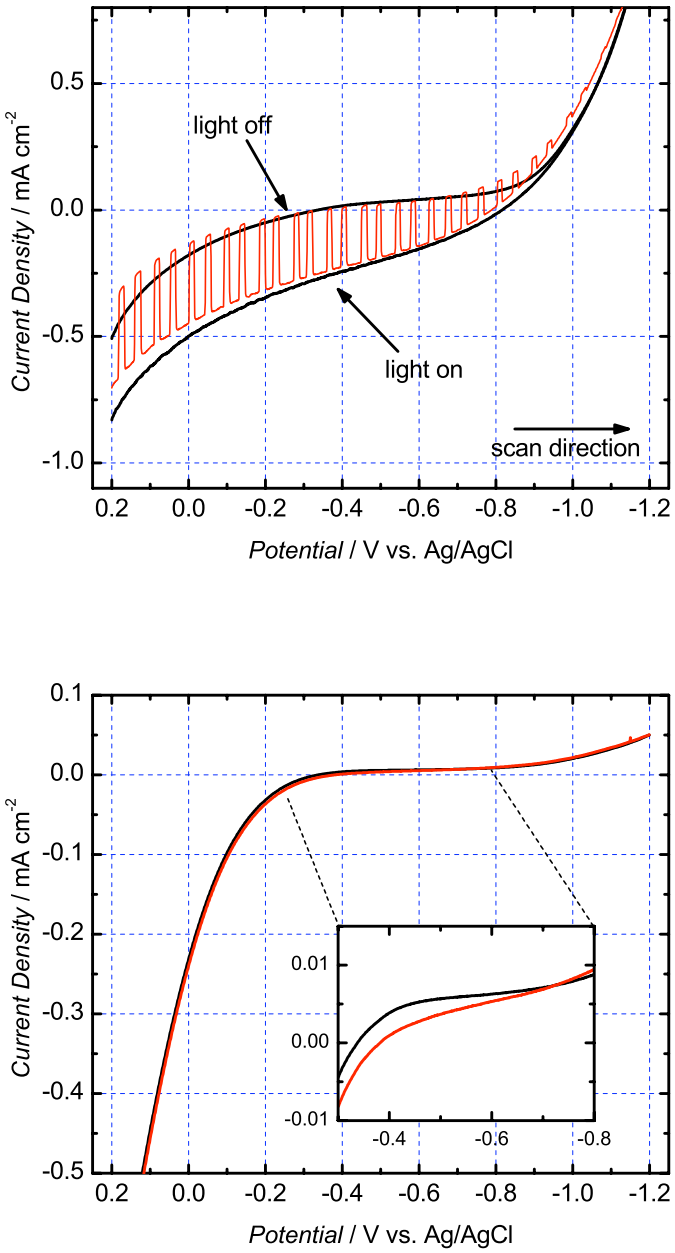

Figure 3.31: Voltammograms of photoelectrodes made from CdSe (upper) and CdTe (lower) quantum rods. The CdSe shows a similar photocurrent density response to the hNR samples. In contrast CdTe based electrodes showed negligible photocurrents.

electrodes were significantly more susceptible to degradation from the 500 °C annealing step performed in an ambient atmosphere. While the rest of the samples all showed a darkening from the heat treatment, the CdTe samples always became more transparent and showed a large amount of white solid. This was believed to be from oxidation of the CdTe to TeO_2, which is a white solid. However, if this is the case, there should also be CdO, which is a red solid and none was observed. However, it is well known that CdTe is significantly more susceptible to surface oxidation than the earlier cadmium chalcogenides as a result of its higher valence band potential. The implications of these findings are that perhaps in the observed photocurrents only CdSe is involved and that the heteromaterial structure is not inhibiting or benefitting photocurrent generation at all.

The role of the annealing step was studied by removing the 500 °C baking and only soft-baking out the remaining solvent at 200 °C for the additional 15 minutes. However, short-circuit photocurrents measured for all samples fabricated this way were very small at < 50 $\mu A/cm^2$ and rapidly degraded during the first cyclic voltammogram with a strong anodic current and an observed flaking-off of the photosensitive film. A consequent limitation of the film degradation was that extensive examination was too inconsistent to yield meaningful and reproducible data for direct comparison to 500 ºC annealed electrodes. The current densities from CdTe prepared at the lower temperature were usually on the order of 25 $\mu A/cm^2$, significantly larger than after the high temperature annealing step, but after an average of 3 CV scans showed negligible photocurrent with most all of the film having flaked off the FTO.

Incident-photon-to-current efficiency

As an alternative to measuring the power conversion efficiencies to determine electrode capabilities, we also measured the incident-photon-to-current-efficiency (IPCE) across the visible spectrum. This experiment gave additional information regarding the response of the cell as a function of photon energy as well as a measure of the overall photon capture efficiency. The spectral response is critically important at this point to determine if any significant structural changes to the nanostructures has occurred as a result of electrode fabrication, specifically the 500 ºC annealing step. This serves as an alternative to a total-reflectance absorbance spectrometer which otherwise would give the absorbance spectrum of the film and an indication of whether the quantum rods have grown or otherwise changed under the elevated temperatures.

The IPCE response of a representative hNR sample and the CdSe samples are both on in the range of 1-10% across the visible spectrum with higher efficiencies at higher photon energies, roughly following the typical absorbance spectra of CdSe and hNR nanomaterials. The CdSe electrode showed a photocurrent shutoff at ~700 nm while the hNR was >800 nm. Importantly, comparison of the spectral response to the colloidal absorbance spectra before electrode preparation shows a dramatic shift to lower energies for both materials (see Figure 3. for details). The transformation is especially pronounced in the CdSe control sample where the CdSe bandgap transition in solution was just above 525 nm but after annealing, the photoelectrode showed a response out to 700 nm. This is indicative of a continued growth of the quantum rods during the annealing process, likely the result of a non-uniform thin-film formation. Thus it is the

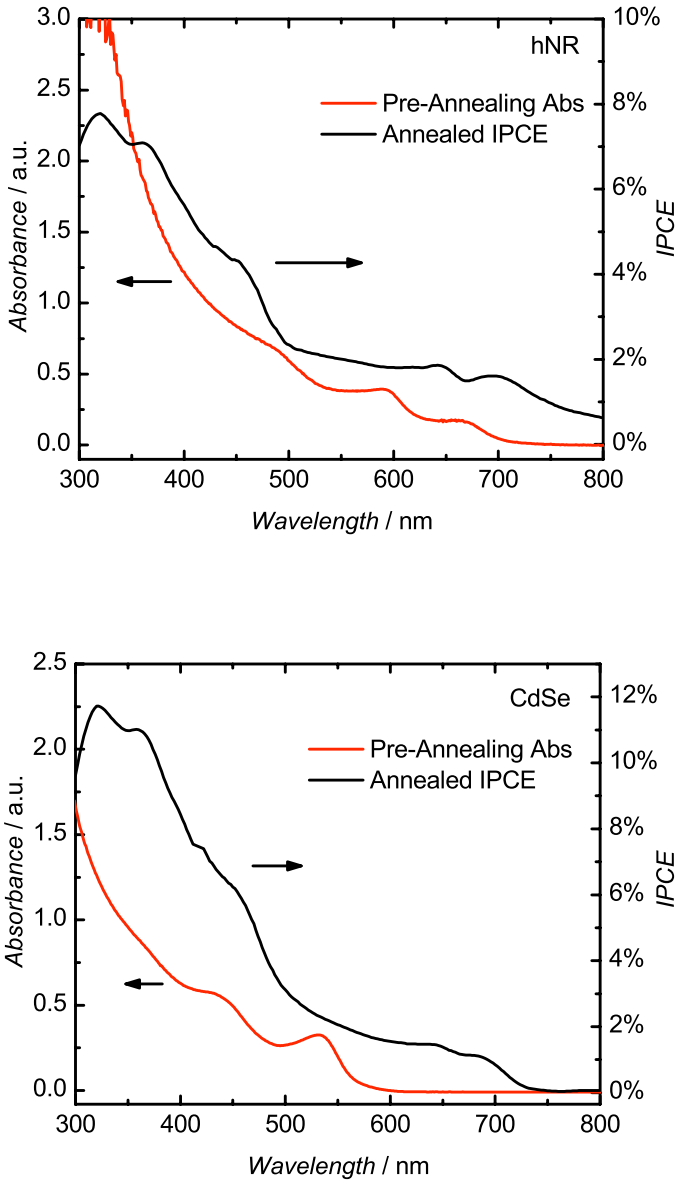

Figure 3.32: IPCE spectra of photoelectrodes of heteromaterial quantum rods (upper) and CdSe quantum rods (lower) show percent efficiencies of 2 – 10 % across the visible spectrum. The increased spectral response of the IPCE measurements in the red and NIR regions compared to the colloidal absorbance profiles in both samples suggests additional growth as a result of the 500 °C annealing process.

effects of the 500 ºC treatment that is believed to remove any distinguishing characteristics between different diameter quantum rods and consequently any distinguishing photocurrent response.

The results of the model photovoltaic device fabrication experiments suggest that better fabrication methodologies are necessary in order to improve power conversion efficiency from photoelectrodes based on semiconductor quantum dots. The necessary step of a 500 °C annealing step deleteriously alters the materials removing the benefits of quantum confinement by promoting additional particle growth, likely by merging with other particles and not through a controlled growth mechanism. It also dramatically oxidizes the CdTe rods, potentially removing the benefits of using type-II heteromaterial quantum rod structures with excellent charge separation efficiencies.

For future electrochemical experiments, a number of important methodologies may be considered as alternatives to the annealed photoelectrode, including work similar to that done by Sargent *et al.* [60, 61, 66, 137] where the materials are not annealed but joined together using small organic linkers and contacted using a metal back electrode to make an all-inorganic solar cell. Further work in our group using such methodologies will continue to be undertaken as work is done to understand the capabilities of quantum dot and quantum rod structures for use in photovoltaic technologies.

3.6 Summary/Conclusions

A number of different chemical linking motifs have been explored to create a semiconductor donor-acceptor complex ranging from electrostatic coupling of aqueous samples to covalent linking by amide bond formation. A heteromaterial quantum rod

structure was synthesized using established organometallic methodologies to couple a CdSe electron acceptor to a CdTe electron donor. For the first time, the electron transfer dynamics in these materials were studied in detail using a broadband pump-probe technique that showed, for materials where the donor and acceptor components are atomically close, that electron transfer from the conduction band of CdTe to that of CdSe occurs on the sub-ps time scale with two distinct time components. First, a quasi-instantaneous transfer on the time scale of the pump pulse is observed where electron density is measured in the CdSe-1S(e) electron state immediately after pumping. The signal from this electron population then continues to increase on a ~400 fs timescale with a concomitant decrease in population of the CdTe-1S(e) electron state. We have examined these dynamics in a range of material sizes and found no substantial dependence on the particle diameter. It has been suggested that ET in such materials should occur in the Marcus inverted region.[117, 130, 131] We have observed the first time-resolved evidence for this hypothesis. A decrease in the electron transfer lifetime from 450 fs to 250 fs was measured to correspond to a decrease in the driving force from 210 meV to 140 meV. However, challenges in the synthesis of particles with the desired electronic properties and inhomogeneous broadening of sample signals have prevented the examination of the complete inverted region curve to date. Additional work in this direction is ongoing in the lab.

With transfer rates on the order of 2.5 x 10^{12} s^{-1} (τ = 400 fs), the electron transfer process in the heteromaterial structures studied are almost an order of magnitude faster than the next fastest carrier cooling process. In CdTe prepared by the chemistry presented here, carrier cooling is typically significantly faster than in CdSe quantum

dots, with an average lifetime of <50 ps compared to the near nanosecond lifetimes in CdSe structures. This can be qualitatively seen simply by the photoemission quantum yields of CdSe which are >100-fold better than CdTe NRs. However, even with a fast native carrier cooling process, the electron transfer lifetime of 400 fs (and faster) suggests that a high yield of carrier separation is obtainable and should not be a limiting factor in photovoltaic devices constructed from these materials. Indeed, carrier separation efficiencies greater than 90% were calculated. However, it is speculated that separating the materials by a layer of organic ligand molecules will drastically effect the electron transfer dynamics by increasing the corresponding reorganization energy and dramatically decrease the adiabatic nature of the electron transfer process through a decrease in the electronic coupling between donor and acceptor electron states.

Lastly, the fabrication of a solar cell based on the hNRs showed markedly good photocurrent densities and IPCEs though very poor overall power conversion efficiencies. Based on the results of these studies in conjunction with the carrier separation results above, the limiting factor in photon energy conversion technologies based on these materials is likely the material interfacing from bulk electrodes, and more fundamentally, the inability to collect the charge carriers from the charge separated states. A considerable effort will be necessary to accomplish the task of improving device efficiency requiring scientists to learn how to more effectively interface with nanostructured materials.

4 Nucleic acid stabilized quantum dots

4.1 Introduction

As highlighted in Section 1.4, inorganic semiconductor nanoparticles are a promising material for the development of optoelectronic devices and novel luminescent biological probes exhibiting greater quantum yields and a higher degree of spectral tunability than their organic counterparts.[34] By choosing between different inorganic materials ranging from larger band-gap II-VI materials such as ZnS, to smaller band gap IV-VI materials, such as PbS and PbSe, the emission of nanometer sized particles can be localized anywhere from the near ultra-violet to the near-infrared. The latter emission range is ideal for shallow tissue imaging in the near-infrared spectral region.[70-72]

Substantial progress has been made in the production of particles with controlled spectral properties, being monodisperse in size (σ < 5%), and stable over time. A variety of single functionality ligands have been employed to accomplish this at elevated temperature (>270 °C) and under an inert atmosphere, the most common being trioctylphosphine (TOP) and trioctylphosphine oxide (TOPO) but also including primary alkyl amines, long chain organic acids and alkylphosphonic acids. Although considerable control has been gained over desired properties, progress in generating water-soluble particles amenable to biological applications or chemistries using more benign conditions has remained a formidable challenge.

For the production of particles miscible in water, a number of methodologies have been employed with ranging degrees of success.[34] Ligand exchange reactions are common in the literature but often lead to incomplete exchange as well as decreased emission efficiencies and stabilities. Research into the synthesis of biologically amenable nanoparticles has lead to studies into both the manipulation and direct synthesis of simple inorganic semiconductors in water using oligonucleotides. With a negatively charged phosphate backbone, accessible endocyclic nitrogen groups, and exocyclic primary amines, nucleic acids have multiple functionalities that can potentially chelate metal cations[141-143] and passivate semiconductor surfaces (see Figure 4.1). Reports on the synthesis of nucleic acid-templated nanoparticles have yielded preliminary information concerning how these biomolecules can be used as ligands.[74, 144-148] However, a comprehensive understanding of how nucleic acids function in semiconductor nanocrystal synthesis has not been attained.

Figure 4.1: Ribonucleotides triphosphates contain functionalities capable of passivating the surface of semiconductor quantum dots.

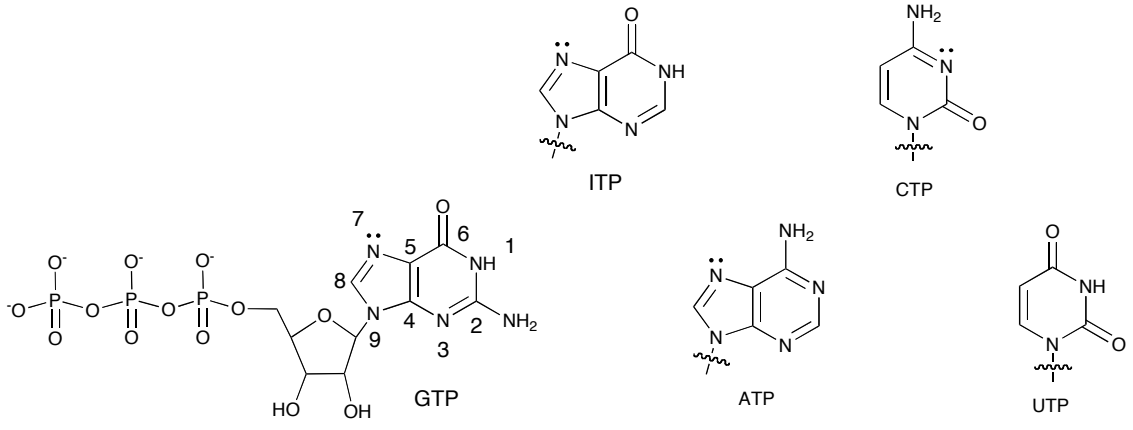

In the work presented here are interested in using nucleic acids as an easily customizable ligand system and scaffold for aqueous semiconductor nanocrystal synthesis. Given that nucleic acids contain functionalities known to interact with semiconductor materials such as CdS and PbS, as well as other inorganic semiconductors, they should provide the relevant chemical moieties for the synthesis of stable materials. Moreover, if nanocrystal growth could be manipulated systematically, the higher-order structures of DNA and RNA polynucleotides could be explored for precise synthetic tuning and an array of potential applications. Towards this end, I present here a systematic and detailed study of nucleotide-stabilized CdS nanocrystals that dramatically extends our published work on PbS.[74] While previous reports have documented that nucleotides can stabilize emissive quantum dots, we have used a combination of fluorescence and absorption spectroscopy, gel electrophoresis and gel filtration, high-resolution transmission electron microscopy (HR-TEM) and energy dispersive spectroscopy (EDS) to explore how different moieties within nucleotides affect the materials produced and generate a meaningful understanding of how a chemist can tune the ligand binding of these materials in water. The results provide the basis for using nucleotide structure to manipulate nanocrystal properties.

4.2 Experimental methods

One of the benefits of the aqueous synthetic method that was developed for this project and is described in detail below is the relatively simple, easily permutable and easily scalable reaction design. For traditional II-VI quantum dot syntheses, like those described in Chapter 3 for the heteromaterial experiments, an inert atmosphere with

elevated temperatures is required including a long preparation time to degas the precursors and remove evolved H_2O from the cadmium/phosphonic acid complex formation process. Accordingly, each reaction requires significant amounts of time, materials and equipment to perform. For the experiments described here, we have successfully scaled down the reaction to those more traditional of a biomolecular reaction dealing with sub-mL scales and ambient temperatures and not requiring inert atmospheres. The result is the chemistry is easily ported to being done in a single eppendorf tube and many reactions can be performed at once for higher throughput.

4.2.1 Nucleotide-CdS synthesis

All chemicals for these syntheses, including but not limited to, nucleotide triphosphates (NTPs), cadmium (II) chloride ($CdCl_2$), sodium sulfide nonahydrate ($Na_2S•9H_2O$), and all buffer salts, were purchased from Sigma-Aldrich and used without further purification. Water was purified and deionized to 18.2 MΩ·cm.

For a typical 3:n:m (NTP:Cd^{2+}:S^{2-}) synthesis on the "0.1x" scale, the following protocol was used. First, stock solutions of 3mM NTP, 27.2 mM $CdCl_2$ and 25.5 mM Na_2S were prepared. For each NTP-CdS to be made, 49 µL of NTP (3 equivalents of NTP) was diluted to 200 µL in water or buffer which ever is being used, in separate eppendorf tubes and sealed. The cadmium precursor solution is then prepared before adding to the NTP solution. To do this, 3, 6, 12, 18, 24, or 30 µL (for 1, 2, 4, 6, 8, and 10 equivalents of Cd^{2+} respectively) of the 27.2 mM stock solution was diluted to 200 µL in water. Of this solution, 120 µL was injected into the NTP solution, mixed and allowed to equilibrate for 2-5 minutes at the desired temperature, usually room temperature.

Illustratively, for the standard 3:4:1 NTP:Cd^{2+}:S^{2-} experiments, 12 µL of the stock Cd^{2+} solution is diluted to 200 µL for a single experiment or 60 µL was diluted to 1 mL for up to 8 experiments.

While the NTP/Cd^{2+} mixture is equilibrating a working solution of the S^{2-} solution is prepared by diluting 8, 16 or 32 µL (for 0.5, 1, or 2 equivalents of S^{2-} respectively) of the stock Na_2S solution to 1mL in water or the desired buffer. When ready to run the reaction, 120 µL of the diluted Na_2S solution is quickly added and vigorously mixed by either vortex or with repeated pipetting for at least 10 seconds. It was found that rapid addition and mixing by repeated pipetting yielded the most reproducible experiments as well as the best emission intensities (see Figure 4.2 on next page). For this reason, this method was usually preferred. Longer mixing times for room temperature reactions were found to have no noticeable effect on the outcome of the reaction. After the reactions have equilibrated for 1-2 minutes, or after quenching elevated temperature reactions by cooling them to room temperature, the samples were centrifuged at 8000 rpm to remove bulk product from the colloidal solution. Of the 440 µL reaction volume, the top ~350-400 µL was removed and used for all subsequent characterizations.

If desired, the particles can be precipitated with ethanol to separate the materials from excess ligands. For the precipitation, a 10% v/v 3 M sodium acetate is added to the sample and then 300% v/v 200 proof ethanol. The mixture can then be mixed on a vortex and chilled at -20 °C for 10-15 minutes. The chilled solution is then centrifuged and the supernatant is removed leaving the white product pellet. The NTP-coated CdS can finally be redissolved in the desired solvent, usually water or buffer.

Syntheses on the "0.1x" scale refers to a base concentration of 100 µM. Therefore a 3:4:1 solution should be at a final concentration of 300 µM NTP, 400 µM Cd^{2+} and 100 µM S^{2-}. For a "1x" synthesis, typically used for large calf-thymus syntheses of PbS materials, the stock dilutions are smaller yielding a final concentration ratio of 3:4:1 mM respectively.

Figure 4.2: The emission spectrum of ATP stabilized CdS in carbonate buffer shows the effect of rapid injection and mixing via micropipette in contrast with mixing via a traditional vortex mixer. The quantum yield was improved by almost 2 fold for ATP syntheses and also showed a marginal improvement in reproducibility.

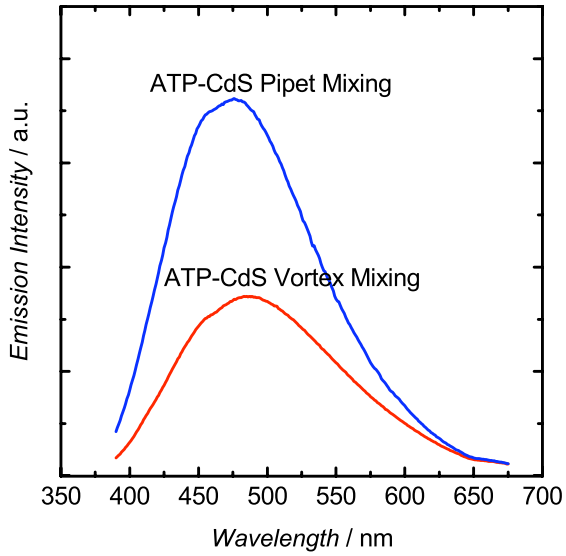

4.2.2 Characterization

Spectroscopy

Absorption and luminescence spectra of the CdS samples were measured on an Agilent 8453 UV/Vis spectrometer and Jobin-Yvon Fluorolog FL3-22 spectrometer,

respectively. Absorbance spectra were collected from 200 to 1100 nm and the spectrometer blanked against water or the corresponding buffer. The luminescence spectra were typically acquired with an excitation wavelength of 362 nm and an emission wavelength range from 390 to 675 nm. The FL3-22 spectrometer excitation source is a 450 W Xe-arc lamp that is passed through a dual monochrometer with variable slits allowing 1-7 nm excitation bandwidths. The emission spectrum is also scanned through a dual-monochrometer with variable bandwidth of 1-7 nm before being detect by a PMT operating at 900 V sensitive to 820 nm. Photoluminescence quantum efficiencies were measured relative to a freshly prepared 7-diethylamino-4-methylcoumarin standard in ethyl acetate, which has a known photoluminescence quantum efficiency (PLQE) of 99% or fluorescein at elevated pH.

Electron microscopy

High-resolution electron micrographs of the prepared nanocrystals were acquired on a JEOL 2010F transmission electron microscope operating at 200 kV. Samples were typically prepared by EtOH precipitation of the nucleic acid capped product and subsequent resuspension in 1/2 volume of water after the removal of the supernatant. Of the more concentrated sample, 2-5 µL were then dispersed on a carbon and formvar coated 300 mesh Cu TEM grid purchased from Ted Pella Inc.

Gel electrophoresis

Analysis of hydrodynamic mobility was measured by gel electrophoresis, typically in a 2% agarose gel in 0.5x tris-borate buffer run for 1 hr. Sample was loaded in a 0.25%

bromophenol blue, 0.025% xylene cyanol FF, 30% glycerol loading dye. The gels were imaged by the emission of CdS nanoparticles with excitation by 365 nm UV light.

4.3 Results & Discussion

Nucleic acids represent a highly tunable ligand system for the stabilization of semiconductor nanocrystals. Parameters of interest include the length, backbone composition and sequence, all of which may play an important role in stabilizing emissive metal chalcogenide nanoparticles. Before a detailed understanding of polymer sequence and other structural polymer effects can be obtained, a systematic examination of nucleotide functionalities is needed. To this end, the synthesis of CdS stabilized by natural and unnatural ribonucleotides, under optimized conditions are reported. The results yield an understanding of the important functionalities in growth and passivation of semiconductor nanocrystals.

4.3.1 Nucleotide stabilized CdS nanoparticles

Precursor ratio optimization

Before setting out to study the binding chemistry of the ligand NTPs in detail, we first needed to optimize the synthetic methodology used. Based on our preliminary results from experiments on PbS[74] where we optimized the synthetic method for reproducibility, we set out to explore and optimize nanoparticle emission intensity by finding optimal ligand-to-precursor ratios. Starting with the 2:1:1 system used for traditional organometallic methods, we found GTP stabilized CdS particles yielded the highest

emission intensities. Based on these findings ratio studies were conducted to find the optimal ligand:precursor ratios with GTP as the standard ligand. A series of experiments were performed where the sulfide concentration was held fixed at 100 µM and the NTP:Cd^{2+}ratios were varied. Preliminary experiments showed that increasing the ligand ratio to greater than 2:1 NTP:sulfide was beneficial (see Figure 4.3 below). A series where the NTP:S^{2-} ratio was fixed at 3:1 is also presented in Figure 4.3 showing the optimal ratio of 3:4:1 giving the highest emission intensity and most blue shifted emission. At higher Cd:S ratios but with a fixed ligand concentration, the emission fell back off toward bulk material.

Figure 4.3: Emission spectra from a series of ratio studies showing improved emission as the GTP:Cd^{2+}:S^{2-} is varied. From this series, it can be seen that as the ratio of ligand to Cd gets above unity, the product tends back toward bulk materials indicated by the red-shift in the emission spectrum.

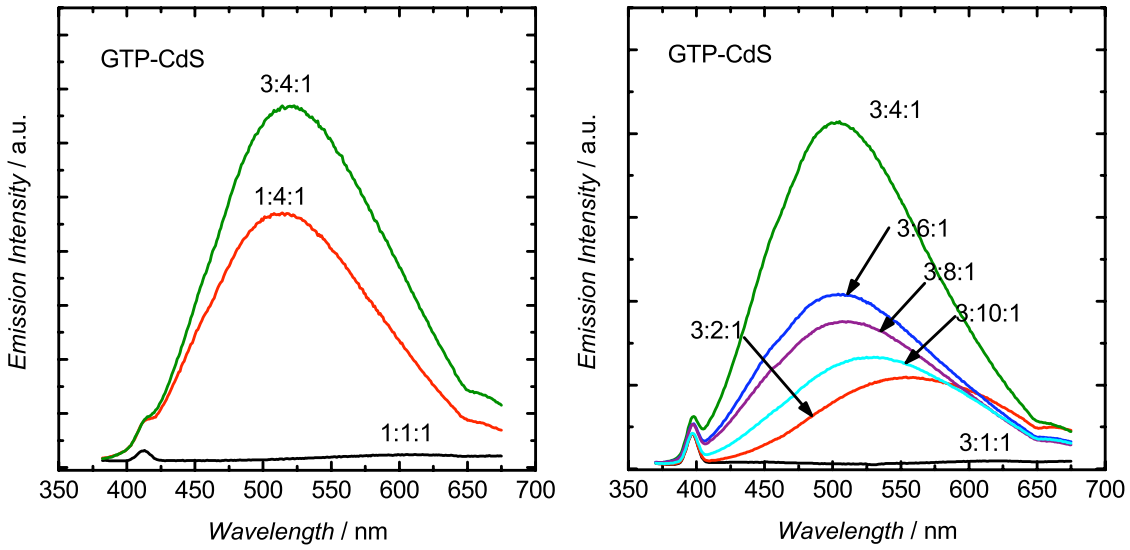

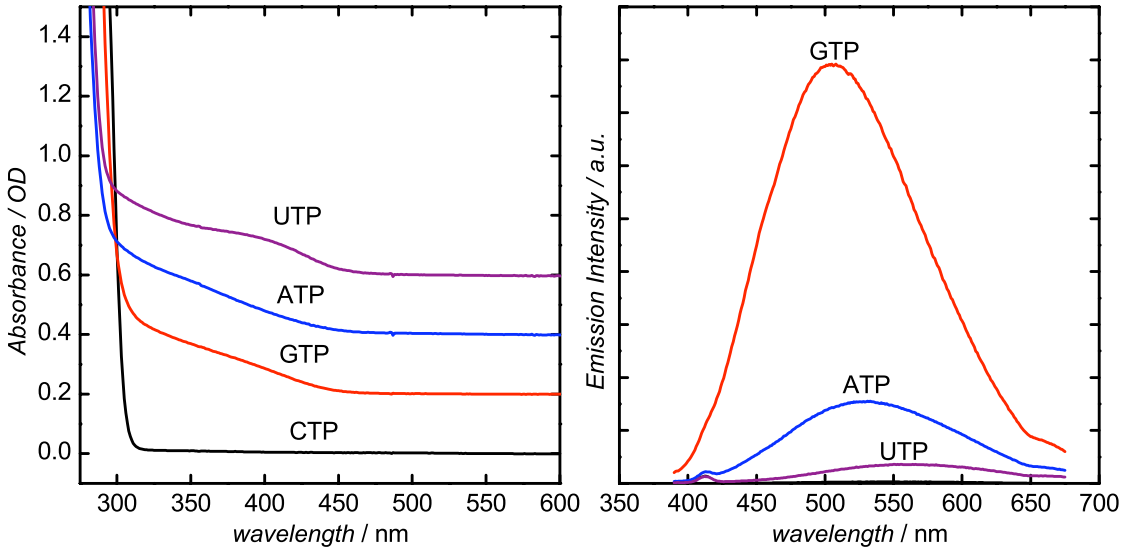

Figure 4.4: Absorbance and emission spectra of NTP stabilized CdS in aqueous solution. The absorbance spectrum of CTP is blank indicative of only bulk material forming which is removed before characterization. The large absorbance feature at <300 nm is the NTP absorbance at ~260nm. GTP yielded the highest emission intensities and most blue-shifted.

Synthetic dependence on nucleotide

Based on the experiments above, the dependence on nucleotide chemistry was studied explicitly by studying the particle properties as a function of the nucleotide triphosphate ligand used. For these experiments, the NTP:Cd^{2+}:S^{2-} ratio was fixed at 3:4:1. Synthesis of CdS in the presence of the four naturally occurring ribonucleotides, done on the 100 μM scale yielded particles with the absorbance and emission spectra shown in Figure 4.4. The synthesis yielded product with appreciable intensity for both purine bases GTP and ATP. The photoluminescence from ATP stabilized product was typically about an order of magnitude less in quantum efficiency at 0.5% and red-shifted

at 545 ± 6 nm compared to the emission of GTP stabilized product. With an emission maximum at 506 ± 6 nm, photoluminescence from CdS stabilized by GTP is roughly equivalent to the bulk material band gap characteristic of an ensemble of well passivated CdS materials with dimensions on the order of the 5nm Bohr exciton diameter.[147] Characterization by electron microscopy further confirms this value for GTP passivated product. Quantitatively, the photoluminescence quantum efficiency (PLQE) of the pyrimidine stabilized products is negligible with no measurable emission from CTP stabilized product and ~0.1% efficiency for UTP capped particles. Although all quantum efficiencies are low and emission profiles are characteristic of non-radiative relaxation and surface trap-state luminescence, the 4.7% PLQE exhibited by GTP stabilized product compares well with previously reported values for calf-thymus DNA passivated PbS synthesized under much higher precursor concentrations.[148]

To identify the chemical functionalities involved in the successful synthesis and stabilization of CdS nanoparticles, the importance of the nucleophilic 7-guanine electrons, the pendant phosphate backbone and the nucleobase exocyclic amine functionalities were examined.[73] The endocyclic purine 7-amino functionality in guanine has been previously shown to interact with metal cations,[142, 143] as has the pendent phosphate group of the corresponding nucleotide triphosphate.[149] Given the differences in effectiveness of stabilization by the four natural ribonucleotides, we used modified guanine nucleobase triphosphates to ascertain the important moieties for crystal formation and stabilization.

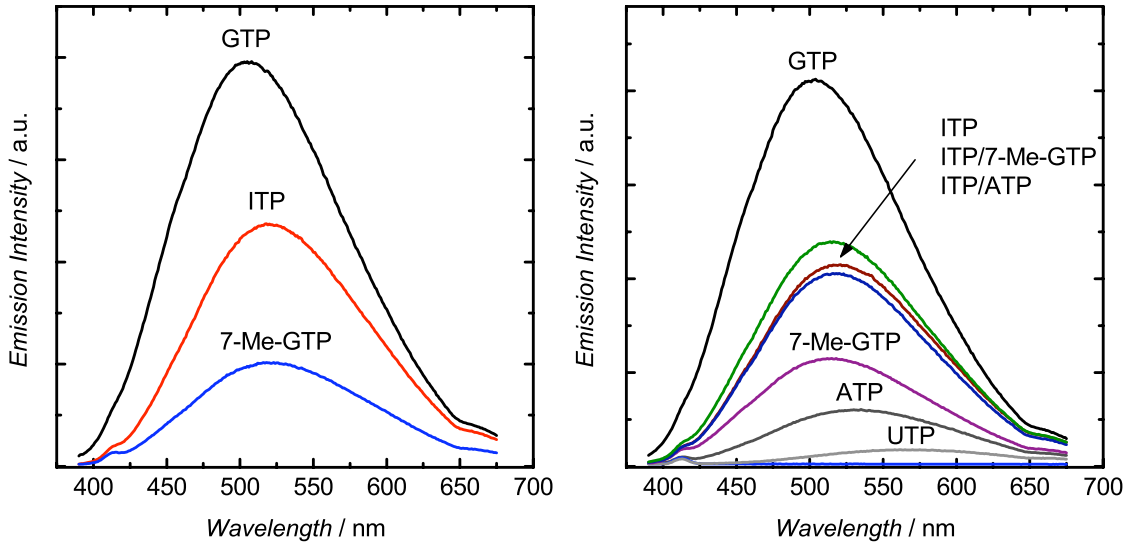

Figure 4.5: Emission spectra of syntheses utilizing GTP analogs ITP and 7-Me-GTP. ITP, which lacks the exocyclic amine, gives CdS particles with better emission properties than 7-Me-GTP which lacks the nucleophilic electrons at the 7-N position of the purine base.

In the presence of the GTP analog inosine triphosphate (ITP), which lacks the exocyclic amine, CdS particles exhibited a PLQE of just below half that of GTP at 2%, and an emission maximum of 520 ± 6 nm, again red-shifted with respect to the bulk material band-gap. These results are in striking contrast to the results with PbS where the 2-amino functionality was critical to successful particle stabilization and solvation[74] suggesting a different mechanism of surface interaction. Synthesis of PbS under identical conditions yields bulk product with no measurable emission, a key difference between the materials that is not clearly understood.

The importance of the N-7 equatorial electrons on guanine can be examined by methylation of the endocyclic amine, making the electrons unavailable for binding to a

cadmium rich surface. Synthesis of CdS in the presence of 7-Me-GTP yields product with limited emission comparable to the product observed with ATP as a ligand. This is consistent with a more critical role for the nucleophilic electrons on guanine. In tying up the electrons in the methyl-ammonium bond, GTP is rendered essentially identical to ATP with its less nucleophilic endocyclic nitrogen and planar exocyclic amine. Accordingly, an extension of our findings with ITP and the natural ribonucleotides suggest that GTP yields the strongest emission efficiency because it can passivate the surface of the product crystal at both cadmium and sulfur sites where the studies analogs can do one or the other.

In the current system, a cadmium rich surface should favor interactions with electron donating groups such as the N-7 position on guanine or perhaps the 6-carbonyl functionality while any surface sulfide sites should prefer a hydrogen-bonding motif. If this is indeed the case, then a mixture of 2 nucleobases, one with a nucleophilic N-7 position for Cd^{2+} binding but no exocyclic nitrogen group and one with an exocyclic primary amine for surface sulfide binding, might behave nearly identical to GTP, which has both. A 1:1 mol/mol mixture of ITP and ATP facilitates this comparison but yields product with emission comparable to that of a reaction with only ITP. Additionally, a mixture of ITP and 7-Me-GTP which has the exocyclic amine at the 2 position yields similar results (Both shown above in Figure 4.5). This is perhaps indicative of the dynamic interaction of the nucleobases with the surface and the blocking of any ATP or 7-Me-GTP surface interactions by the relatively bulky purine ligand of ITP, which binds most strongly. Furthermore, this suggests that GTP may be simultaneously binding with both functionalities consistent with previously reported FT-IR data[74] and a binding motif

not capable by other nucleotides yielding higher emission yields and more strongly stabilized particles.

Synthetic dependence on polyphosphate

The nucleobase is not the only functionality expected to play an important role in the synthesis of emissive CdS; the pendant triphosphate is known to coordinate to Cd^{2+} and Pb^{2+} ions and this step may be critical in controlling the rate of nanocrystal nucleation by controlling the availability of the cadmium precursor. To examine the role of the polyphosphate in GTP stabilization of CdS, syntheses were carried out with both mono- (GMP), and di- (GDP) phosphates, as well as with the guanosine nucleoside that lacks

Figure 4.6: Experiments with guanosine n-phosphate illustrate the importance of the phosphate backbone for particle synthesis. A synthesis with GDP yielded identical particles optically to GTP but at half the concentration. GMP yielded very little product.

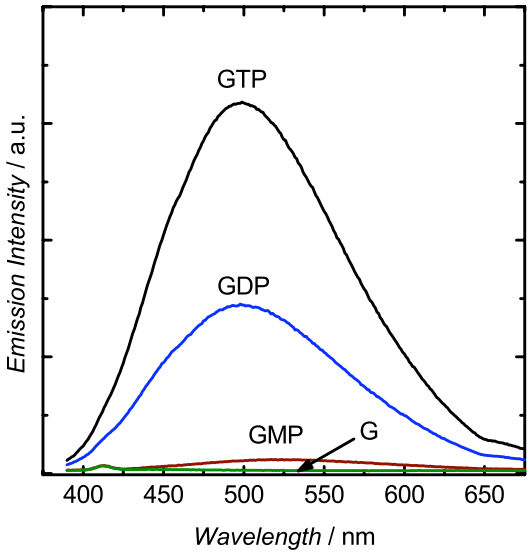

any phosphate functionality. In water, GTP and GDP gave indistinguishable particles as determined by spectral shape, position and PLQE. However, under identical starting concentrations, GDP yielded a solution with about half the CdS optical density as GTP, with the remainder of the CdS materials having precipitated out of solution as insoluble bulk material. In contrast, GMP yields only marginally photoluminescent product that is significantly red-shifted from the GDP and GTP products. The poorly soluble guanosine, lacking any phosphate groups, gave no measurable product emission. These results are indicative of the key role the polyphosphate plays in preparation of Cd^{2+} ions within a phosphate shell before reaction with the corresponding chalcogenide. The four negative charges and near-by equatorial N-7 guanine electrons are likely able to weakly complex 2 Cd^{2+} ions while GDP, with only 3 negative charges, can only completely coordinate 1 ion for reaction. Metal cations that are not coordinated by the polyphosphate and 7-purine nitrogen pocket remain in solution where upon binding with the sulfide ion rapidly grow unpassivated and fall out of solution. At the low concentrations used in these experiments, < 1 mM, it is unlikely that a discrete nucleation event will occur in free standing solution and then be rapidly passivated before it grows too large to remain in solution. These results identify the triphosphate pendent in the screened materials as critical for the initial coordination of cadmium and its preparation for reaction with the chalcogenide while in close proximity to a capable ligand system.

4.3.2 Effect of hydroxide on NTP-CdS synthesis

Effect of buffers on synthesis

It has been known for almost two decades that increasing the pH is a straightforward method to improve exciton radiative recombination efficiency in CdS nanocrystals.[150] Accordingly, we were interested in looking to reproducibly control the pH of our reaction on the sub-mL scale to examine the effect of pH on the NTP binding chemistry. The pH of the reaction can be adjusted by a number of different means, including addition of $^{-}$OH or use of a carbonate or phosphate buffer. When we started this work, no reports of using buffers had been explored as the buffering salts were also likely to interact with the particle surface. To this end, we first explored the effects of different buffers and added salts on the syntheses of CdS nanocrystals.

Using water as a control, 3 different buffers were screened as well as a simple pH adjustment using a small injection of 0.1 M NaOH to the NTP/Cd^{2+} solution. It was found that neutral tris buffer has no significant effect on the product, indicating that the protonated amine in the buffering salt has no beneficial or deleterious effect on the surface of the particles. In contrast, pH 10 carbonate buffer offered a significant improvement to the quantum yield as well as a noticeable blue-shift indicating improved surface passivation. The improved emission is characteristic of a surface coating of Cd-OH groups, traditionally believed to passivate dangling bonds in conventional aqueous syntheses and improve PLQE.[150] In contrast, the use of a phosphate buffer to adjust the pH shows detrimental effects at both neutral and elevated pH. The origin of these effects is likely the result of the phosphate conjugate base binding free cadmium

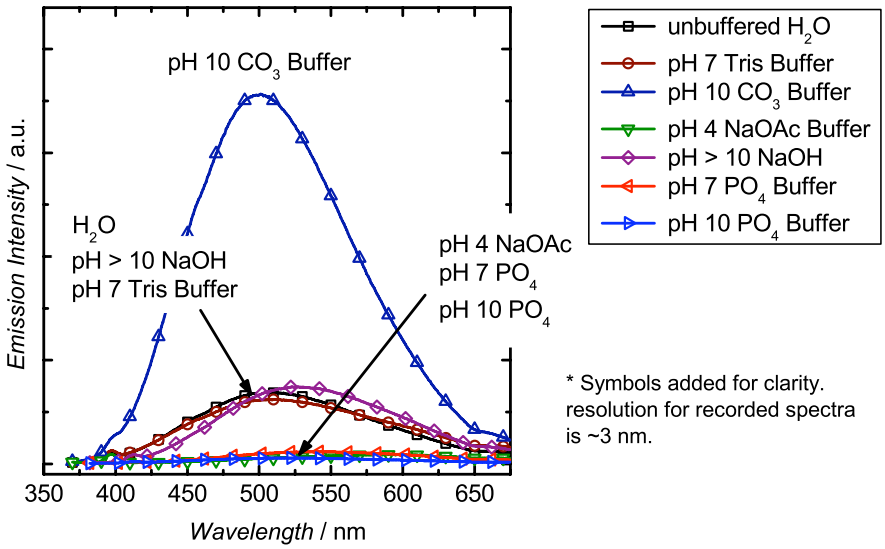

Figure 4.7: Different buffers were studied to examine the effect of additional salts on the formation of GTP-CdS nanoparticles. It was found that phosphate buffers deleteriously effected the formation of quality CdS nanoparticles while carbonate buffers enhanced significantly the particle emission. NaOH addition yielded variable results though on average was only slightly better than an unadjusted synthesis.

sites on the surface of the nanoparticle. This is supported from the fact that in organometallic reaction methods, alkylphosphonic acids are commonly used because they bind cadmium stronger than traditional organic acids or alkylamines. Presumably then, the phosphate salts bind to the surface of the crystal changing the surface chemistry which no longer facilitates secure passivation by the solubilizing NTP.

The result of this previous study is that a weak carbonate buffered solution at pH 10 allows for control over the pH without detrimental effects on the reaction chemistry involved in the formation of CdS nanoparticles. In screening other buffers at different concentrations and pHs, we found that at low salt concentrations buffers performed the same as or better than their unbuffered counterparts (NaOH addition) with greater reproducibility between experiment. NaOH addition had sporadic effects and was highly

sensitive to overall concentration. In the presence of moderately high $^{-}$OH concentrations (pH >12-13), Cd(II) salts precipitate out as white $Cd(OH)_2$ out competing with the weakly binding GTP.

Nucleotide effects at elevated pH

As a result of our previous studies, a low concentration (10 mM) carbonate buffer at pH 10, was used to controllably and reproducibly increase the pH of the reaction and consequently promote higher emission efficiencies, fewer mid-band trap-states and simultaneously change the surface-ligand binding motif to study the effect on the NTP binding chemistry. In using a carbonate buffer, we also expected a change in the coordinating chemistry motif; a change from nucleobase-metal interactions to simple hydrogen bonding nucleobase-CdOH interactions. Experimentally, quite a dramatic change was observed. Though the luminescence efficiency of GTP stabilized CdS only slightly decreased and its corresponding emission shifted to 512 ± 3 nm, the other nucleotides abilities to stabilized emissive products changed dramatically. Both CTP and UTP yielded emissive nanocrystals with emission efficiencies comparable or better than GTP at 3.5% and 6.1% respectively. Furthermore, with the increased emission efficiencies, a shift toward higher energy emission was observed with UTP at 514 ± 7 nm and CTP at 529 ± 7 nm. The emission lineshapes are still significantly broad but are dramatically increased in intensity from their non-buffered counterparts. What is more striking from the ensemble of data is that both ATP and ITP overtook GTP in both emission energy and PLQE. With emission maxima blue-shifted from the bulk material

band-gap (492 ± 4 and 495 ± 4 nm respectively), the PLQE values were generally around 7.0% an 8.5% respectively with an experimental maximum observed at ~10%. These higher than band edge emission maxima are suggestive of weak quantum confinement and both show evidence of a blue side shoulder at 450 nm consistent with emission from well passivated products observed in conventional organic syntheses.[151] Representative photoemission spectra are shown in Figure 4.8 indicating these trends above. Additionally, Figure 4.9 shows a summary representation of the PLQE trends comparing syntheses in H_2O with elevated pH as well as a the relative emission maximum relative to the bulk band energy.

Figure 4.8: Photoluminescence spectra of NTP-stabilized CdS synthesized in pH 10 carbonate buffer show dramatically different emission profiles than the spectra of materials synthesized in water.

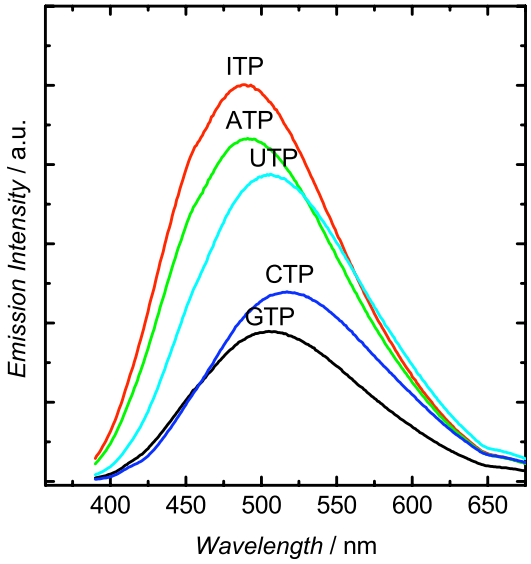

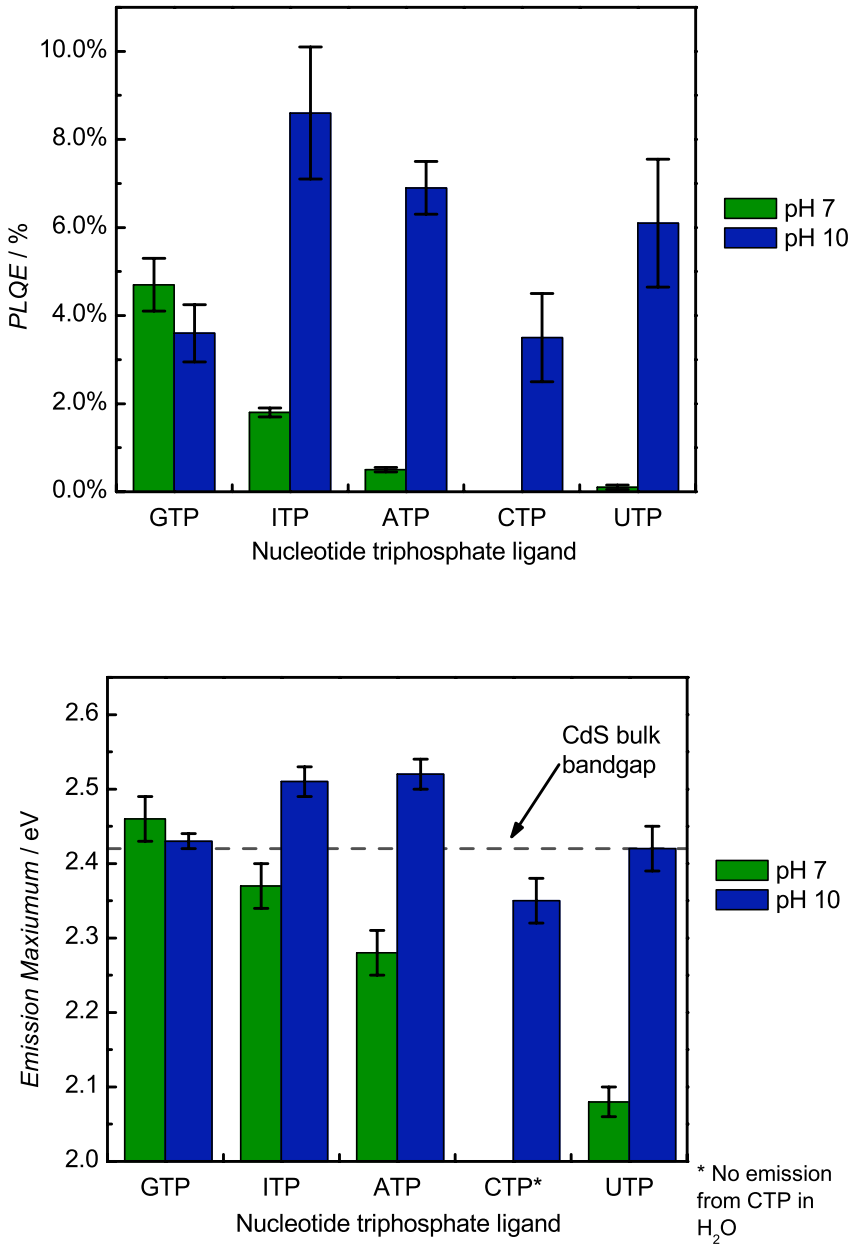

Figure 4.9: (upper) Comparison of the PLQEs of the 4 natural ribonucleotides and ITP used to stabilize CdS nanoparticles in H_2O and pH 10 carbonate buffer showing the strong out performance at elevated pH. (lower) A graphical representation of the emission maximum of the nanoparticles for the screened conditions relative to the bulk band gap of 2.42 eV. Emission maxima higher than 2.42 are evidence of quantum confinement.

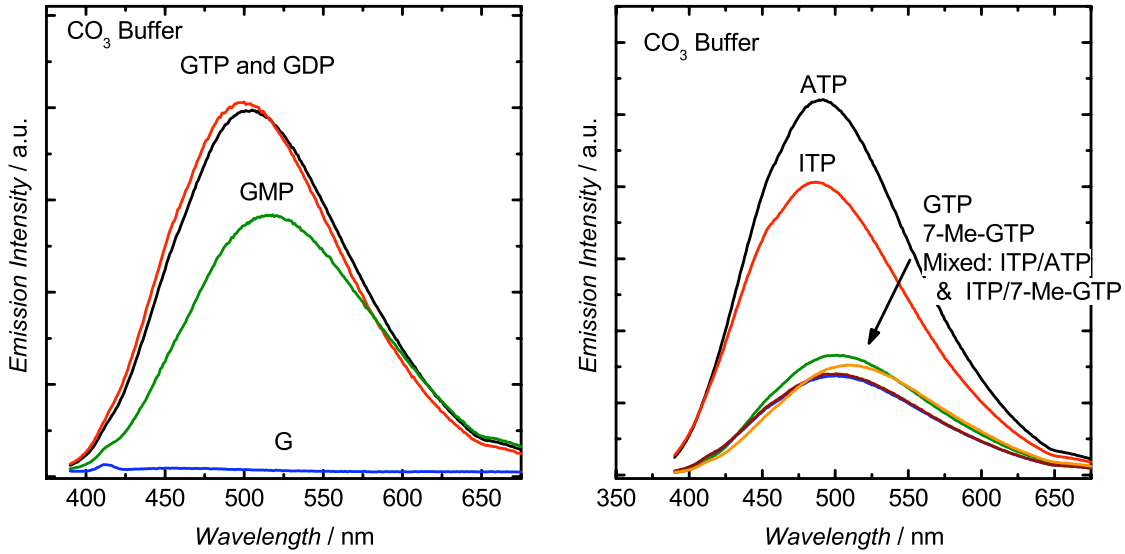

Figure 4.10: (left) GnP, where n = mono, di, or tri, stabilized CdS in pH 10 carbonate buffer shows a decreased dependence on the phosphate backbone. (right) Mixed ligand and GTP analog emission spectra. GTP, 7-Me-GTP and GDP provided experimentally identical products and yields. This is in striking contrast to the same materials in unbuffered solutions.

An examination of the other GTP analogues yielded further information about these systems and the important functionalities at elevated pH. Stabilization by 7-Me-GTP as well as GDP lead to product indistinguishable spectroscopically and in product yield from that of GTP at elevated pH, consistent with a change in the passivation and precursor preparation schemes. The data from representative experiments are presented above in Figure 4.10. Both 7-Me-GTP and ITP mixtures exhibited diminished surface-Cd binding in H_2O while at elevated pH, the H-bonding surface passivation chemistry has decreased the dependence on the endocyclic 7-purine nitrogen. Furthermore, the likely formation of cadmium hydroxide in solution decreases the need of 3 phosphate groups to coordinate effectively the cadmium ions before reaction with the sulfur chalcogenide, indicated by

the GDP-stabilized product. Interestingly, though GMP gave a significantly more emissive product in buffer compared to just water, its emission maximum was still red-shifted to that of the GTP product suggestive of a hindered ability to get the surface binding nucleobase near the forming CdS. It seems then that the tertiary structure of the polyphosphate is important and with the longer, more flexible diphosphate and triphosphate a pocket is available that can hold Cd^{2+} or $^{+}$Cd-OH close to the nucleobase while the shorter monophosphate cannot. As expected the altered surface composition changed the surface-binding motif such that all nucleotides are all capable of stabilizing nanoparticles, a result that may be less than ideal.

The increase in pH, though frequently utilized to improve the PLQE of cadmium chalcogenide semiconductor nanoparticles by eliminating surface trap states through Cd-OH formation, is detrimental to the ligand specificity offered by using nucleic acid ligands. In looking to extend these results to polynucleic acids we would expect no sequence-only specificity. This does not preclude any tertiary structure dependence of product particle size, evidence for which we have already reported in aqueous syntheses.[144] Consequently, with the aim of generating sequences where only specific regions bind to the surface while other regions are solution accessible, syntheses need to be done under neutral aqueous conditions where, under optimized ligand rations, PLQEs are still appreciable.

Application of buffer synthesis findings to PbS

Based on the work on CdS described above, the buffered synthesis methodology was extended to the PbS materials initially of interest.[74, 148] While in unbuffered aqueous solution it was previously found that only GTP gave nanocrystals, in carbonate buffer four of the five tested nucleotide triphosphates yielded particles with similar emission profiles. Only CTP did not yield any soluble product, instead showing only the formation of bulk PbS materials. Interestingly, no degree of tunability in particle size was evident. With a smaller band gap and large Bohr exciton radius, PbS emission is significantly more sensitive than CdS to particle diameter and therefore would easily have been observed if present. In the synthesis of CdS in buffer, particles stabilized by ATP and ITP gave cleaner emission profiles and smaller particles. As characterized by their emission profiles, the PbS materials obtained are indistinguishable.

Figure 4.11: Photoemission from NTP capped PbS synthesized in pH 10 carbonate buffer. No emission was visible from CTP products

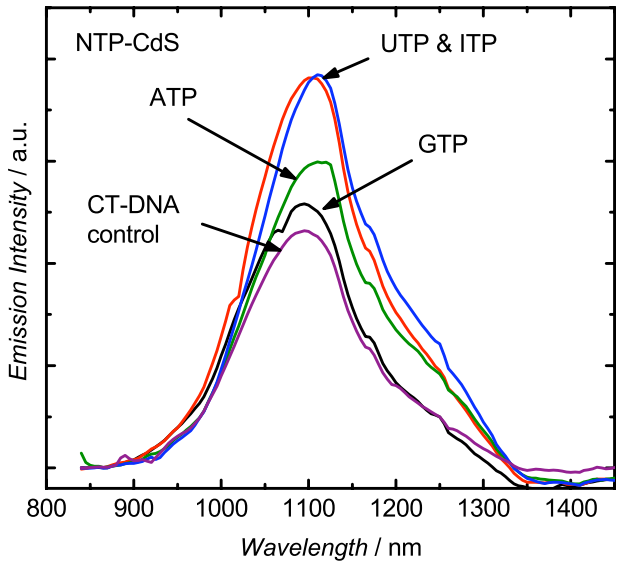

Importantly, compared to a control sample made using bulk calf-thymus DNA in water, the materials are also essentially the same suggesting little ligand specific chemistry to control the particle geometry under elevated pH.

4.3.3 Size determination

In the fabrication of nanomaterials with the aim of eventual biological applications, especially for *in vivo* studies, the size of both the semiconductor or metal crystal, testable by transmission electron microscopy (TEM), and hydrodynamic size, testable by light scattering or gel filtration, are of significant importance. The crystal size and geometry has important implications on the spectroscopy while the hydrodynamic size is relevant to the expected product mobility and gives a sense as to the nature of the ligand shell dimensions. In our experiments we used high-resolution TEM and a combination of gel filtration and gel electrophoresis to characterize NTP-CdS product crystal size and hydrodynamic mobility respectively.

Analysis of the ethanol precipitated NTP stabilized CdS product by HR-TEM showed a wide size and shape distribution among the different nucleotides consistent with the variation in luminescence spectra observed and characteristic of the kinetically controlled crystal growth at the low temperatures employed. In water, only GTP exhibited particles with average sizes on the order of 5±1 nm while ITP stabilized particles, with the next best emission profile, showed significantly more variation in size and shape with cross-sectional lengths ranging from 5-10 nm. Notably, GTP stabilized crystals were also generally non-spherical though with less variation than ITP. Samples from ATP primarily exhibited large particle aggregates consistent with the low intensity, trap-state emission

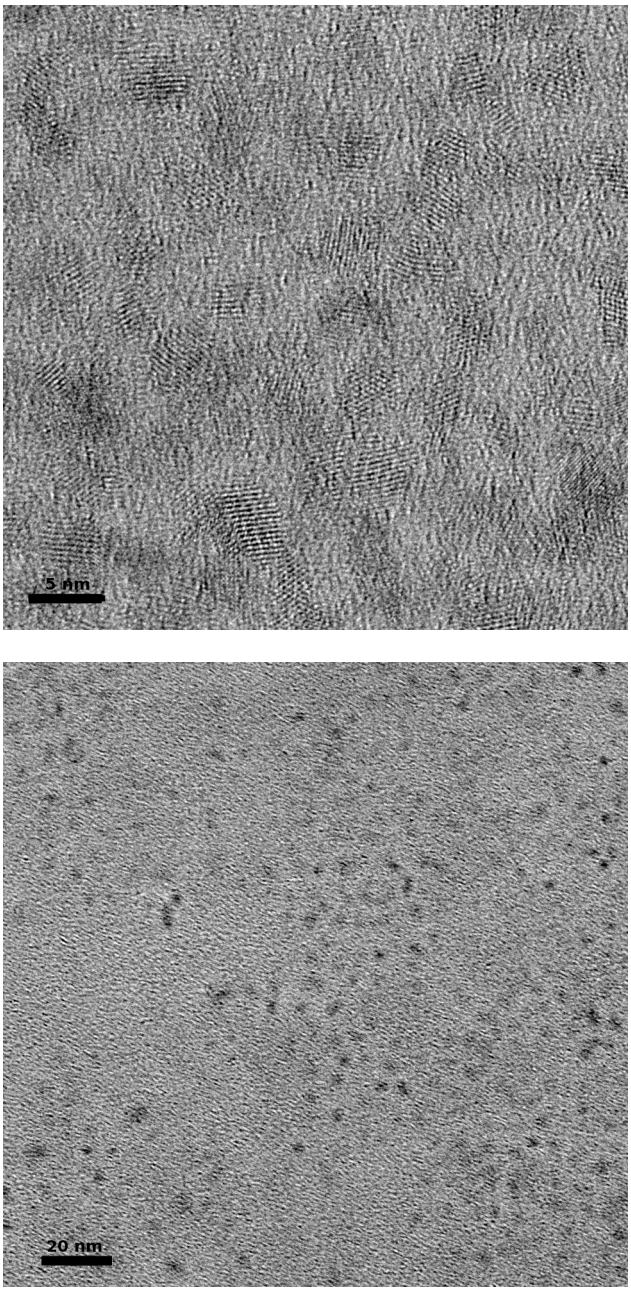

Figure 4.12: High and low-resolution TEM micrographs of ATP (upper) and GTP (lower) stabilized CdS nanocrystals.

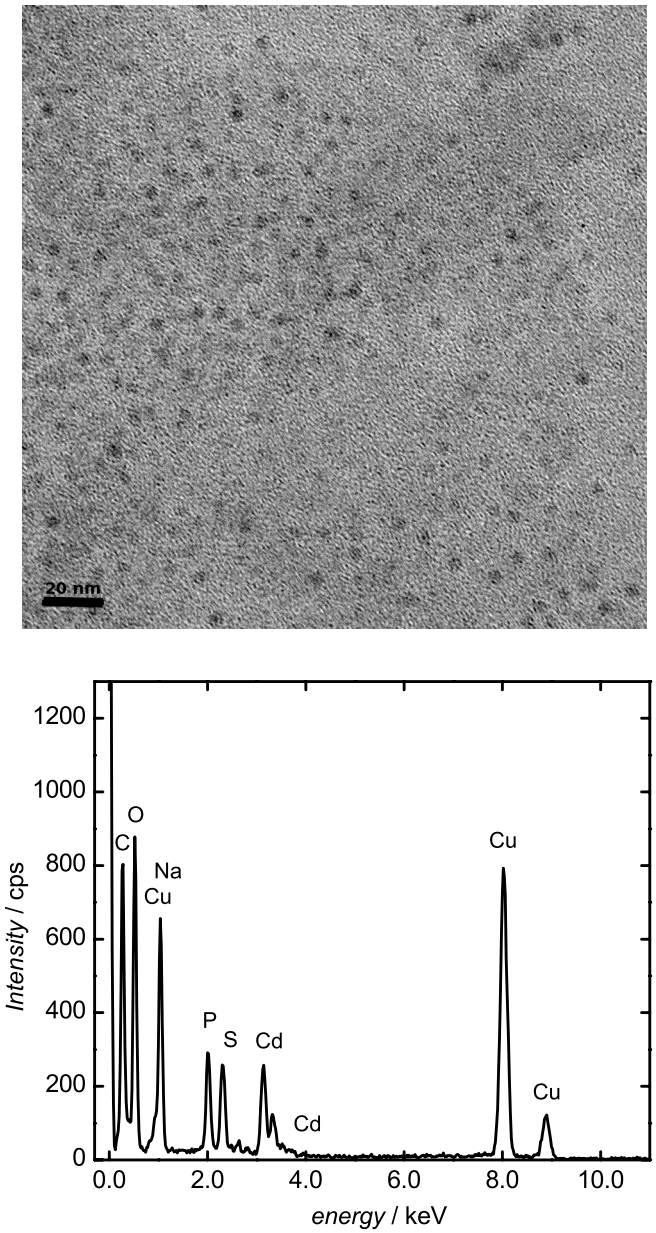

Figure 4.13: TEM micrograph of ITP stabilized CdS and the corresponding EDX spectrum showing the CdS and phosphate composition of the materials.

profile from a weakly binding ligand system. Material from UTP and CTP could not be desalted effectively without flocculation preventing quality TEM micrographs from being obtained.

Conversely, the more highly emissive and better-stabilized Cd-OH capped particles from carbonate buffered syntheses were more easily characterized. On average, the purines showed similar sized particles ranging from 3-5 nm in cross-sectional lengths and all were noticeably variable in particle shape prohibiting quantifiable correlation between particles size and photo-emission maximum. The pyrimidine products in contrast were noticeably larger measuring 6-8 nm for CTP-CdS and 5-7 nm for UTP-CdS crystals. The particles for both the elevated pH syntheses and neutral reactions were polydisperse in size and geometry, consistent with the FWHM values greater than 100 nm.

Table 4.1: NTP-CdS nanoparticle emission maxima and crystal sizes based on TEM.

Nucleotide	pH	λ_{em} max / nm	Particle Size / nm
GTP	7	506 ± 6	4.2 ± 0.5
	10	511 ± 3	3.9 ± 0.7
ATP	7	545 ± 6	7.6 ± 2.0
	10	492 ± 4	3.9 ± 0.8
CTP	7	-[a]	-[b]
	10	529 ± 7	5.6 ± 1.2
UTP	7	598 ± 7	-[b]
	10	514 ± 7	4.7 ± 1.0
ITP	7	523 ± 6	4.5 ± 1.0
	10	495 ± 4	3.1 ± 0.3

[a] No measureable emission was observed from CTP-CdS. [b] Only bulk material was observed from pyrimidine nucleobases in neutral conditions.

Agarose gel electrophoresis was used to monitor hydrodynamic mobilities for nucleotide-stabilized nanoparticles. The emission from CdS under UV excitation allows the positions of the nanocrystals to be monitored directly, and thus the technique provides insight into charge and size trends. Analysis of NTP stabilized nanocrystals in a neutral environment showed limited mobility for GTP and ITP samples (see below) and negligible mobility from ATP and UTP. For the more highly emissive elevated pH samples, mobilities tracked nearly identically with the unbuffered counterparts

Figure 4.14: Gel electrophoresis shows the effect of the ligand shell on particle mobility. Samples made in unbuffered solution (top-left) had approximately the same mobility as those made in carbonate buffer (top-right). Increasing the total NTP concentration increases the particle mobility while also decreasing emission intensity (lower).

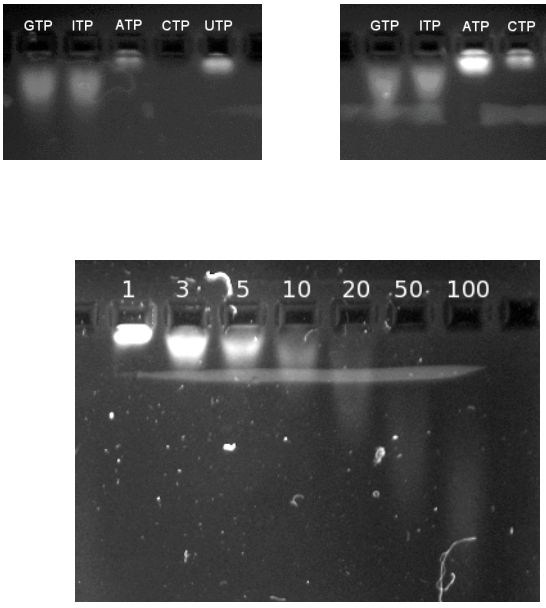

suggesting mobility dictated by a ligand mediated solvation shell and less on crystal geometry. If the concentration of charged ligands is increased from the typical 3:4:1 to more 100:4:1, as shown in the lower gel in Figure 4.14, then the mobilities increase. The samples are blurred out through the gel indicating a large dispersion of sizes and charges. This is consistent with particles that have a large solvent shell made up of a dynamically binding charged ligand system.

Lastly, examination by gel-filtration chromatography strengthens this hypothesis by identifying hydrodynamic diameters that are often 5x greater than the crystal size at almost 28-29 nm for GTP made in carbonate buffer. Such sizes are appreciably less than ideal for biological applications. However, comparison with RNA stabilized nanocrystals shows the limited mobility may only be a problem for single or short

Figure 4.15: Gel filtration chromatogram showing GTP emission relative to a protein ladder used as a standard. The standards are, in order of decreasing size, blue dextran, thyroglobulin, BSA, and lysozyme corresponding to 29.5 nm, 18.8 nm, 7.0 nm and 3.9 nm respectively.

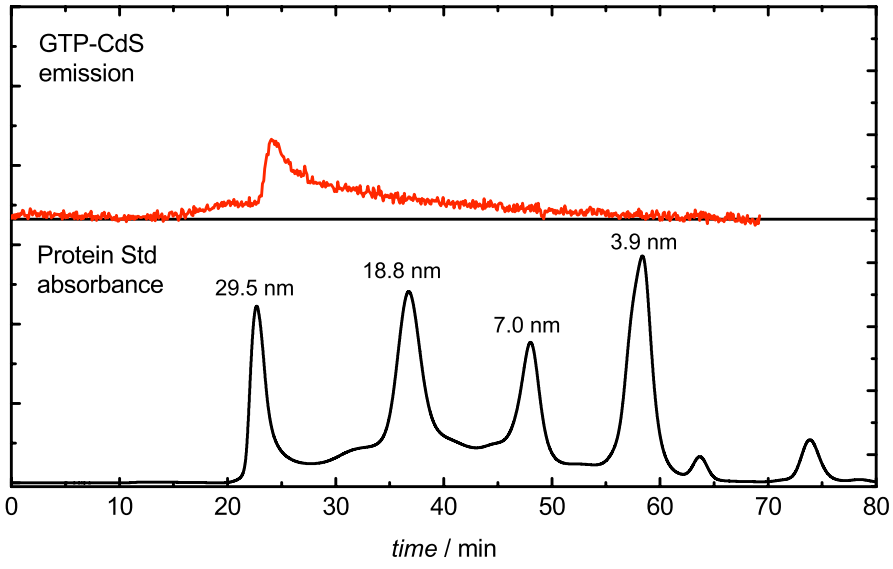

nucleotide sequences with a higher charge to ligand ration and should not be as much of a challenge when exploring the rest of polynucleic acid space.

4.3.4 Conclusion

Nucleic acids represent a promising ligand system for the stabilization of inorganic semiconductor quantum dots allowing chemists the ability to vary both ligand chemistry and structure. We have shown that under optimized neutral conditions, GTP can stabilize CdS nanoparticles with PLQEs of 5% while the next closest emission efficiency from CdS passivated by a naturally occurring nucleotide was almost an order of magnitude less. Syntheses with guanine analogs ITP and 7-Me-GTP identify the importance of the nucleophilic N-7 electrons of guanine in facilitating this reaction while studies with different phosphate pendent lengths demonstrate that the phosphate group is critical in cadmium precursor coordination and less the final product passivation. The use of elevated pH effected a general increase in quantum efficiency but also changed the coordination binding chemistry to primarily hydrogen binding resulting in loss of nucleotide specificity. The broad emission profiles observed are characteristic of the polydisperse crystal geometries and mid-band trap-states, the former being confirmed by transmission electron microscopy with particle sizes ranging from 3-5 nm with non-spherical geometries for purine stabilized elevated pH syntheses, 4-6 nm for unbuffered GTP-CdS and as high as 10 nm for other products. Although the hydrodynamic size of the smallest of these particles is too large to use *in vivo*, an extension of what has been learned should prove promising in the exploration of polynucleotide sequence space. Although one might expect that with polynucleic acids some degree of nucleobase dependence might break down as a general polymer effect, understanding the role

individual nucleotides play in surface stabilization may still allow for engineered sequences with a surface binding region and a solution displayed region. Such a co-polymer like structure would allow for further solution phase manipulation and perhaps the engineering of larger structures from quantum dot building blocks.

5 Outlook

The previous chapters have reported our findings on the fundamental chemical and physical properties of semiconductor nanocrystals, both from an optoelectronic and synthetic chemistry approach, as they apply to photovoltaic technologies. The findings have specific implications for the design of quantum dot based photovoltaic devices, and other optoelectronic applications. In this final section a brief discussion on the outlook of this work is presented.

Of specific interest was the study of the electron transfer from the 1S(e) electron state of CdTe to that of CdSe. In order for these materials to be suitable for solar energy applications, this transfer process needs to be competitive with carrier cooling which can occur as fast as ~20-50 ps in CdTe. It was found that charge carrier separation in Cd-based heteromaterial quantum rods occurs on the 400 fs timescale and faster, more than 5-10 times faster than the fastest cooling processes. Additionally, a transfer process on the timescale of the excitation pulse in these experiments, typically ~45-60 fs, was observed which has been attributed to direct optical electron transfer. Consequently, charge carrier separation rates are sufficiently competitive with carrier cooling to make these materials effective for uses in solar cells. Considering the poor power conversion efficiencies that have been observed, both in experiments presented here and reported in the literature, in contrast to the high electron separation efficiencies, the remaining challenge in producing production level solar cells is the optimization of interfacing with these materials and bulk electrodes.

Secondly, the use of nucleic acids as surface stabilizing ligands provides a potentially suitable means to construct ordered arrays of different quantum dots and effective interfacing to electrodes where DNA chemistry is well established. Work on the specific binding chemistry shows that at physiological pH values, GTP selectively stabilizes particles but that under elevated pH values, where better PLQEs are observed, less ligand specificity is present.

A number of important questions are raised as a result of the presented work. Firstly, from a theoretical point of view, a detailed examination of the forward electron transfer inverted-region behavior in hQRs should provide a meaningful validation of Marcus theory. With reorganization energies below 50 meV, quantum dots are acutely capable of exploring this non-intuitive behavior. In order to concretely provide these results, improvements in the experimental control over the electron transfer reorganization energy and driving force need to be made as such control is presently missing and has limited our examination of the problem so far.

The continued exploration of the photon energy conversion capabilities of these materials is a rapidly evolving field. Firstly, experiments into removing high temperature annealing chemistry will be necessary to maintain controlled quantum confinement. One way to accomplish this is the use of small electron donating ligands that can cross link particles together as well as bind them strongly to the surface of an electrode. Additionally, hybrid structures, with either polymer interfaces or other semiconductor electrode surfaces, such as TiO_2 are a potential platform to consider. Studies on these platforms are rapidly appearing in the literature, but work to put the performance in context of the fundamental capabilities of these devices is critical. To this end, time-

resolved studies provide meaningful insight into carrier transfer dynamics. With a small number of additional modifications to the typical pump-probe spectroscopy described in Chapter 2, time-resolved dynamics can be extracted from solid-state samples as well as from the solution phase materials currently being characterized. In this manner, the characterization of charge injection into electrodes can be studied, and a more complete understanding of the carrier behavior can be constructed.

Some of the simple modifications that are necessary and currently underway include the reorganization of the detection system to reflectance mode detection instead of a transmission mode detection as well as moving the probe capabilities further into the infrared. By probing further into the infrared, out to > 5000 nm specifically (<200 meV), intra-band transitions in the valence band and conduction band can be studied as has been done to elucidate electron injection dynamics in dye-sensitized architectures. To generate a probe pulse in the mid-IR is a straightforward extension of the dual non-collinear optical parametric amplifier used for pump-pulse generation. Wavelengths out to about 2.5 μm can be obtained directly by isolating the idler signal from traditional parametric amplification, or by building an IR specific OPA. For wavelengths further into the mid-IR, a difference frequency generation scheme can be used where the signal and idler are refocused into a $AgGaS_2$ crystal making available probe pulses from ~2.5 μm to almost 10 μm.

Broader Outlook

While the potential effects of a fossil fuel dependent energy economy over the next 20-50 years are sobering, the efforts currently being undertaken around the world offer quite a bit of hope. The work presented in this dissertation is a small fraction of the many

different directions that scientists are pursuing. As highlighted in Chapter 1 and further in the Appendix, there is a substantial amount of energy available from both solar and geothermal sources in addition to the more easily accessible biofuel, nuclear and wind sources; more than enough to maintain and support a modernized economy. From great challenges come great rewards. The vast efforts in energy generation currently being undertaken are likely to offer fundamental breakthroughs in the understanding of novel material capabilities as well as technological development. While the exact effects of a carbon-fuel dependent population will play out over the next century, it is likely that economic and environmental pressures will bring about the changes that are necessary.

New and rapid developments in water splitting catalysis, photon energy conversion and hydrogen storage promise a CO_2-free energy source. Additionally, the development of fuel-cell technologies promise more efficiency in the use of chemical fuels. It may turn out that semiconductor quantum dots will not factor into these solutions as photon energy conversion in devises based on the novel materials continues to be inefficient. However, the studies here indicate that fundamental charge carrier separation kinetics are more than sufficient for collecting absorbed photon energy. What remains is the development of the technologies to interface and extract the collected energy. The latter manifests a broader problem left to tackle by the scientific community as bottom-up growth of nanostructured materials continues to refine into a mature science accessible by broader technologies.

6 Appendix

In this appendix, a brief introduction to the broader motivation for the work in this dissertation is presented. A look at the global energy demand is described along with a projection of future demand based on current trends in economic development, population growth and improvements in energy intensity. Furthermore, the scale of the energy consumption is put into context of the availability of different renewable energy sources specifically focusing on solar energy.

Motivation

During the last 5 years since I first began the work in this dissertation, the global energy demand and corresponding implications of fossil fuel consumption have become recognized as an international problem with political, economic and environmental implications. The engineering and scientific communities have been challenged to dramatically improve access to renewable and sustainable energy supplies to fuel a rapidly expanding global economy in place of conventional fossil fuel sources.

In 2005, the world consumed about 4.73 x 10^{20} J (473 EJ) of energy, with the US responsible for almost 25% of that consumption at 1.1 x 10^{20} (110 EJ).[152, 153] This consumption corresponds to an average yearly burn rate of 15.4 TW globally and 3.4 TW by the U.S.[a] Significantly, both in the United States and internationally, about 85% of

[a] Burn rates are calculated as the average power output necessary to provide the consumed annual energy. It is calculated as total energy, *E,* divided by the number of seconds in 1 year

the total energy consumed is fossil fuel based. Coal and natural gas each account for 26% of that fraction with petroleum accounting for the final 47%. Historically, the fraction based on fossil fuels has remained around 85% since the early-1980s, having declined from over 90% in the third quarter of the 20th century. Without significant technological improvements in other forms of energy production and utilization, this value is not expected to decline significantly in the foreseeable future.

To gauge an estimate on what the future energy demand will be, a simple projection can be constructed based on the historical values of three contributing factors and their average growth rates.[8, 154, 155]

$$E' = N \cdot \frac{GDP}{N} \cdot \frac{E'}{GDP} \tag{6.1}$$

Here, E' is the annual rate of energy consumption, N is the sample population, and GDP is the sample's gross domestic product. The term E'/GDP is known as the energy intensity and represents how much energy is consumed per unit of GDP and is therefore a measure of how efficiently countries use energy. While the global population and GDP on average increase over an extended time period, the energy intensity typically declines as technologies become more energy efficient. Applying a continuous growth model, the projected annual change in energy consumption is a linear combination of each term's respective rates of change.[156]

According to the U.S. Census Bureau[157] the average global population is currently increasing at ~1.2% annually and at a projected average of 0.9% over the next 50 years.

(365d/y·24h/d·60m/h·60s/m). So 473 EJ equals $473 \times 10^{18}/(365 \cdot 24 \cdot 60 \cdot 60) = 1.54 \times 10^{13}$ W, or 15.4 TW of average power and TW-yr of energy.

Estimates of the global GDP/N[158] show an increase of 1.26% in 2008, and 1.8% overall during the last decade. The United States GDP growth rate has been about 1.7% per capita over the past decade and -0.25% in 2008.[158] For the sake of projections, annual growth rates slightly less than the decade average can be assumed at ~1.6% globally. The amount adjusted for the global market is to account for the slight slowdown in economic development in developing countries over the next 50+ years. Presently, China and India have extremely rapid developing economies at 8.7% and 5.2% respectively.[158] Lastly, around the world energy intensity has approximately declined at an average rate of just less than 1% annually going into 2005,[159] and is expected to continue at this rate for the near future.[154] Importantly, however, in the U.S. and other large economies the energy intensity has been declining at an average of almost 2% for the last decade.[158] From these values, projections for the total energy demand for 2030 and 2050 based on equation 6.1 can be calculated and are presented below in Figure 6.1.

From the discussion above, energy demand in the US is expected to grow at a moderate rate of approximately 0.7%. This leads to a conservative estimate of a 20% increase in energy demand from 3.4 TW-yr to 4.0 TW-yr by 2030 and a 37% increase to 4.6 TW-yr by 2050. Comparably, the global picture is more dramatic. Energy demand is expected to increase at a rate of 1.5-1.7% annually. At this pace the total energy burn rate will grow from 15.4 TW in 2005 to 24 TW by 2030 and approximately double by

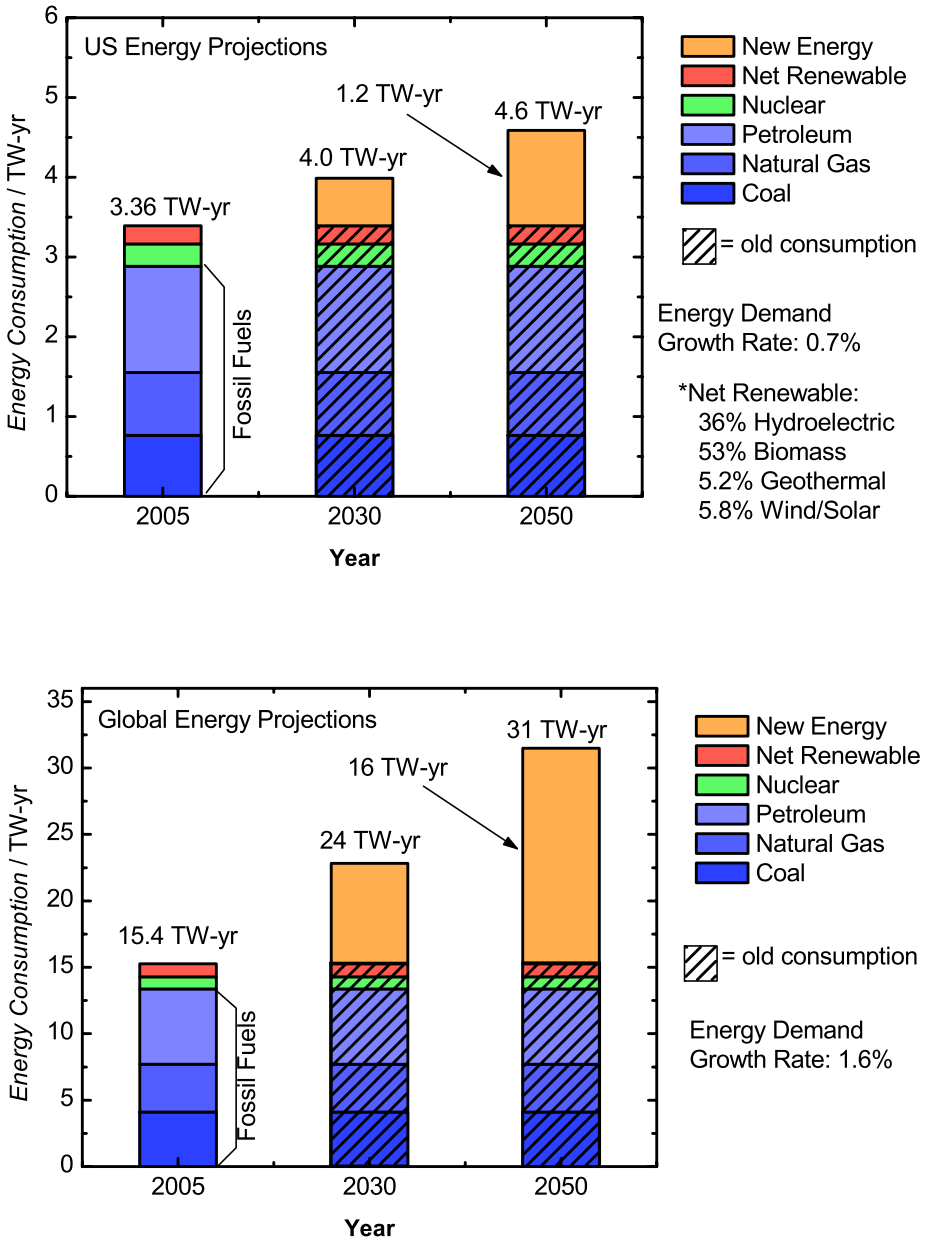

Figure 6.1: Plots showing the projected energy demand for the United States (upper) and globally (lower) for 2030 and 2050 based on a simple consumption analysis. The global demand for energy is projected to double by 2050 from 15.4 TW-yr to 31 TW-yr at current market conditions. The source of this energy is critically important economically and environmentally. (2005 data from the Energy Information Administration at the U.S. Department of Energy[153])

2050 to 31 TW. These projections, based on a relatively fundamental model, agree well with the projections from the U.S. Department of Energy of 23.3 TW by 2030 (695 GBtu) based on a more sophisticated market analysis.[160]

To understand the origin of the large growth in energy demand, it is elucidative to make an examination of the energy consumed per capita as a function of the GDP per capita for developed and developing nations.[158] This comparison, made in Figure 6.2 on page 146, shows that the U.S. has historically used about twice the amount of energy for relatively the same per capita GDP as most of the other developed economies of the world, particularly Japan and countries in the European Union. Only more northern countries such as Iceland, Norway and Canada consume relatively more energy than the U.S per person for a given per capita income value. While the U.S. presently consumes a disproportionate amount of energy, its projected increase in consumption is not as dramatic as the global increase. The U.S. fraction of the projected "New Energy" needed in 2050 is less than 10%. Furthermore, the growth of the rest of the developed nations also is relatively small. Largely this is a function of two terms in equation 6.1. The population of the U.S. is only about 5% of the total world population and the GDP per capita is increasing at a relatively steady (not immediately accounting for late 2008), but marginal rate. In contrast, the economies of India and China are growing rapidly as noted earlier and combined they make up 37% of the global population.

Both India and China currently consume less than 2 kW-hr of energy per person and have an average GDP per capita of < $4000 USD (adjusted to year 2000 values), however they are quickly developing toward having economies on the order of the E.U.

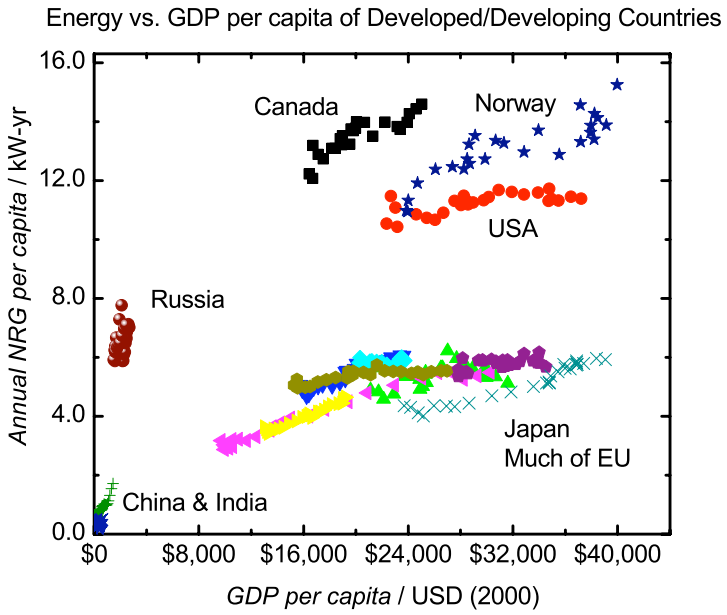

Figure 6.2: Comparison of the historical energy per capita of select developed/developing nations as a function of the GDP per capita. This figure shows that on average citizens in the U.S. consume about twice the amount of energy per $US (adjusted to yr 2000 value) than many nations in the European Union. In contrast, the rapidly developing economies of China and India show that their energy consumption and economic wealth have yet to reach the levels of a modern "developed" nation (raw data from the DOE[153] and USDA[158])

and United States. This rapid economic development coupled with their large populations make India and China the largest consumers of the projected "New Energy." Under closer examination, between 1997 and 2007 the total historical energy consumption by the U.S., Europe, and Japan, increased at a rate of 0.6%, 0.8% and 0.6%, respectively.[153] In contrast, China's energy consumption grew at a rate of 7.2% while India's grew at a slightly slower 4.7%. Neither of these growth rates is sustainable over the long term but it is expected that the economies of China and India are going to continue to expand toward the GDP per capita values enjoyed by the rest of the

developed world. Along with this growth will come the increased consumption of energy, which accounts for most of the increase in global demand over the next 20 to 40 years.

Given this projection of a considerable increase in demand over the next half century, it is imperative to consider where this energy will come from. First, to put into perspective how much energy an additional 10 or 16 TW is, a modern nuclear power plant provides about 1 GW of power. At this rate, if all the power for the additional 9 TW needed by 2030 were to be provided by a nuclear plant, 1.07 new plants would need to be built every day for the next 21 years. Similarly, if all the additional power for the 16 TW needed by 2050 were to be provided by wind turbines, then 22% of all usable land and coasts around the world would need to be developed and covered in wind farms as recent estimates put a total of 72 TW of available wind energy globally.[161] A more generous estimate gives the total potential wind energy of 190 TW, still only 12-fold larger than current energy demand.[162] In practice, both of these technologies currently are in commercial production for electrical power only, which accounts for only 13% of the total average power used (1.7 TW of 15.4 TW) in 2005[153] not accounting for losses, but they illustrate clearly the scale of the task at hand.

The projections on energy demand are valid if only the projected economic growth can be sustained by relatively inexpensive and easily available energy. The cheapest and most accessible energy source currently being used is fossil fuel sources. Based on estimates from the United Nations Development Program's World Energy Assessment, there are roughly 200 years worth of petroleum based resources, 400 years of natural gas, and ~700 years of coal in proven conventional and unconventional reserves, as well as estimated resources, at current consumption rates.[163] As estimates of additional

natural gas resources and coal resources push the overall available fuels to much higher levels[8] it is expected that fossil fuels will be able to support the projected economic development if no competitive alternative exists.

Consumption of fossil fuels at the rates currently needed to sustain a modern economy, while possible, pose an important potential risk. The emission of anthropogenic CO_2 by burning carbon-based fuels has lead to the rapid increase in concentration of atmospheric CO_2.[164] Historically, over the past 600,000 years specifically, atmospheric CO_2 levels have oscillated between 210 and 300 ppm.[165, 166] Presently the atmospheric concentration is about 380 ppm, a value not seen in measured history. At modest assumptions of a decline in carbon intensity (amount of carbon emitted per unit energy) over the next century, the total concentration would still more than double.[8, 154]

Some impacts of the increase in anthropogenic CO_2 are already being seen. Specifically surface and ocean temperatures rises of about 0.6 °C over the past century have been measured as well as a considerable increase in ocean levels.[164] The projected impacts of the continued increase in anthropogenic CO_2 is debatable, but a number of models from the Intergovernmental Panel on Climate Changes (IPCC) has projected a temperature increase of 0.4 °C over the next 20 years and from 1 to 3 °C by the end of the century.[164] The projected impacts of the increase in anthropogenic green house gasses has been explored in great detail by the IPCC and made available in their most recent Synthesis Report.[164]

While the politics of what developed and developing countries should do to mitigate, if at all, the projected impacts is debatable, it is clear that in order to sustain the modern

global economy a source of energy that is either carbon-neutral or carbon-free needs to be developed. A number of traditional alternatives are available, each with different costs of implementation, including biofuel sources, hydroelectric power, wind farming, and solar energy (photovoltaic and solar-thermal). Table 6.1 summarizes the estimated global capacity for these sources as well as their unit cost of implementation compared to the roughly 3¢ it costs to deliver traditional fossil fuel based power.[2]

A suitable short term solution that has been emphasized in the early part of this last decade is the use of biomass based fuels which are net carbon-neutral[167-169] This source is roughly a direct substitute for liquid fossil fuels and therefore requires little additional technological development. However, biomass growth is essentially a specific type of solar powered fuel cell where the energy from the sun is converted into carbon-carbon bonds in the form of sugars and other biomass. It has been estimated that the total solar

Table 6.1: Comparison of the total theoretical annual power capacity and current cost estimates of different renewable energy sources.[161, 163, 170] The average cost of new energy from fossil fuel sources is included for comparison.[2]

Energy Source	Theoretical Power Availability (TW-yr)	Energy Costs ($/kW-hr)
Biomass	92	0.03 – 0.12
Hydropower	4.6	0.02 – 0.10
Wind Energy	72	0.03 – 0.10
Ocean Energy	235	0.04 – 0.20
Solar Energy	120,000	0.25 – 1.60
Geothermal	4,400,000	0.02 – 0.10
Fossil Fuel		0.03 – 0.05

power conversion efficiency of the photosynthetic process is only 3-4%, prior to any form of plant processing to make the material usable as liquid fuels.[1] The limited efficiency is largely the result of the limited spectral response of photosystem I and II, P700 and P680 respectively, to the edge of the visible spectrum. Additionally, because of the limited amount of land that can be allocated for fuel production and still a sustainable amount of food crops, the total estimated capacity for fuel production is only about 90 TW-yr.[170] For these reasons, while biofuel production is likely a short-term solution, the long term global energy demands will require a new approach, one that is preferably carbon-free or is capable of having a nominal anthropogenic CO_2 output and can be scaled beyond the current projected development.

7 References/Notes

1. Zhu, X.-G.; Long, S. P.; Ort, D. R., What is the maximum efficiency with which photosynthesis can convert solar energy into biomass? *Current Opinion in Biotechnology* **2008,** *19* (2), 153-159.

2. Lewis, N. S., Toward Cost-Effective Solar Energy Use. *Science* **2007,** *315* (5813), 798-801.

3. Nozik, A. J., Quantum dot solar cells. *Physica E: Low-dimensional Systems and Nanostructures* **2002,** *14* (1-2), 115-120.

4. Shockley, W.; Queisser, H. J., Detailed Balance Limit of Efficiency of p-n Junction Solar Cells. *J. Appl. Phys.* **1961,** *32* (3), 510-519.

5. Lin, Y.; Zhou, S.; Liu, X.; Sheehan, S.; Wang, D., TiO2/TiSi2 Heterostructures for High-Efficiency Photoelectrochemical H2O Splitting. *J. Am. Chem. Soc.* **2009,** *131* (8), 2772-2773.

6. Kanan, M. W.; Nocera, D. G., In Situ Formation of an Oxygen-Evolving Catalyst in Neutral Water Containing Phosphate and Co2+. *Science* **2008,** *321* (5892), 1072-1075.

7. Soper, J. D.; Kryatov, S. V.; Rybak-Akimova, E. V.; Nocera, D. G., Proton-Directed Redox Control of O-O Bond Activation by Heme Hydroperoxidase Models. *J. Am. Chem. Soc.* **2007,** *129* (16), 5069-5075.

8. Lewis, N. S.; Nocera, D. G., Powering the planet: Chemical challenges in solar energy utilization. *PNAS* **2006,** *103* (43), 15729-15735.

9. Kanan, M. W.; Surendranath, Y.; Nocera, D. G., Cobalt-phosphate oxygen-evolving compound. *Chem. Soc. Rev.* **2009,** *38* (1), 109-114.

10. Betley, T. A.; Wu, Q.; Van Voorhis, T.; Nocera, D. G., Electronic Design Criteria for O-O Bond Formation via Metal-Oxo Complexes. *Inorg. Chem.* **2008,** *47* (6), 1849-1861.

11. Hu, X.; Cossairt, B. M.; Brunschwig, B. S.; Lewis, N. S.; Peters, J. C., Electrocatalytic hydrogen evolution by cobalt difluoroboryl-diglyoximate complexes. *Chem. Comm.* **2005,** (37), 4723-4725.

12. Hu, X.; Brunschwig, B. S.; Peters, J. C., Electrocatalytic Hydrogen Evolution at Low Overpotentials by Cobalt Macrocyclic Glyoxime and Tetraimine Complexes. *J. Am. Chem. Soc.* **2007,** *129* (29), 8988-8998.

13. Du, P.; Knowles, K.; Eisenberg, R., A Homogeneous System for the Photogeneration of Hydrogen from Water Based on a Platinum(II) Terpyridyl Acetylide Chromophore and a Molecular Cobalt Catalyst. *J. Am. Chem. Soc.* **2008,** *130* (38), 12576-12577.

14. Connolly, P.; Espenson, J. H., Cobalt-catalyzed evolution of molecular hydrogen. *Inorg. Chem.* **1986,** *25* (16), 2684-2688.

15. Wilson, A. D.; Newell, R. H.; McNevin, M. J.; Muckerman, J. T.; Rakowski DuBois, M.; DuBois, D. L., Hydrogen Oxidation and Production Using Nickel-Based Molecular Catalysts with Positioned Proton Relays. *J. Am. Chem. Soc.* **2006,** *128* (1), 358-366.

16. Wilson, A. D.; Fraze, K.; Twamley, B.; Miller, S. M.; DuBois, D. L.; Rakowski DuBois, M., The Role of the Second Coordination Sphere of [Ni(PCy2NBz2)2](BF4)2 in Reversible Carbon Monoxide Binding. *J. Am. Chem. Soc.* **2008,** *130* (3), 1061-1068.

17. DuBois, M. R.; DuBois, D. L., The roles of the first and second coordination spheres in the design of molecular catalysts for H2 production and oxidation. *Chem. Soc. Rev.* **2009,** *38* (1), 62-72.

18. Appel, A. M.; DuBois, D. L.; Rakowski DuBois, M., Molybdenum-Sulfur Dimers as Electrocatalysts for the Production of Hydrogen at Low Overpotentials. *J. Am. Chem. Soc.* **2005,** *127* (36), 12717-12726.

19. Alivisatos, A. P., Birth of a Nanoscience Building Block. *ACS Nano* **2008,** *2* (8), 1514-1516.

20. Rossetti, R.; Nakahara, S.; Brus, L. E., Quantum size effects in the redox potentials, resonance Raman spectra, and electronic spectra of CdS crystallites in aqueous solution. *J. Chem. Phys.* **1983,** *79* (2), 1086-1088.

21. Brus, L. E., Electron-electron and electron-hole interactions in small semiconductor crystallites: The size dependence of the lowest excited electronic state. *J. Chem. Phys.* **1984,** *80* (9), 4403-4409.

22. Bawendi, M. G.; Steigerwald, M. L.; Brus, L. E., The Quantum Mechanics of Larger Semiconductor Clusters ("Quantum Dots"). *Ann. Rev. Phys. Chem.* **1990,** *41* (1), 477.

23. Norris, D. J.; Bawendi, M. G., Measurement and assignment of the size-dependent optical spectrum in CdSe quantum dots. *Phys. Rev. B* **1996,** *53* (24), 16338.

24. Norris, D. J.; Sacra, A.; Murray, C. B.; Bawendi, M. G., Measurement of the size dependent hole spectrum in CdSe quantum dots. *Phys. Rev. Lett.* **1994,** *72* (16), 2612.

25. Weller, H., Quantized Semiconductor Particles: A novel state of matter for materials science. *Adv. Mater.* **1993,** *5* (2), 88-95.

26. El-Sayed, M. A., Small Is Different: Shape-, Size-, and Composition-Dependent Properties of Some Colloidal Semiconductor Nanocrystals. *Acc. Chem. Res.* **2004,** *37* (5), 326-333.

27. Murray, C. B.; Kagan, C. R.; Bawendi, M. G., SYNTHESIS AND CHARACTERIZATION OF MONODISPERSE NANOCRYSTALS AND CLOSE-PACKED NANOCRYSTAL ASSEMBLIES. *Ann. Rev. Mater. Sci.* **2000,** *30* (1), 545.

28. Clapp, A. R.; Medintz, I. L.; Mattoussi, H., Förster Resonance Energy Transfer Investigations Using Quantum-Dot Fluorophores. *ChemPhysChem* **2006,** *7* (1), 47-57.

29. Klimov, V. I., Spectral and Dynamical Properties of Multiexcitons in Semiconductor Nanocrystals. *Ann. Rev. Phys. Chem.* **2007,** *58* (1), 635-673.

30. Kuno, M., An overview of solution-based semiconductor nanowires: synthesis and optical studies. *Physical Chemistry Chemical Physics* **2008,** *10* (5), 620-639.

31. Klimov, V., *Semiconductor and Metal Nanocrystals: Synthesis and Electronic and Optical Properties*. Marcel Dekker, Inc.: New York, 2004.

32. Kamat, P. V., Quantum Dot Solar Cells. Semiconductor Nanocrystals as Light Harvesters. *J. Phys. Chem. C* **2008,** *112* (48), 18737-18753.

33. Henglein, A., Small-particle research: physicochemical properties of extremely small colloidal metal and semiconductor particles. *Chem. Rev.* **1989,** *89* (8), 1861-1873.

34. Medintz, I. L.; Uyeda, H. T.; Goldman, E. R.; Mattoussi, H., Quantum dot bioconjugates for imaging, labelling and sensing. *Nature Materials* **2005,** *4* (6), 435-446.

35. Alivisatos, A. P., Perspectives on the Physical Chemistry of Semiconductor Nanocrystals. *J. Phys. Chem.* **1996,** *100* (31), 13226-13239.

36. Rossetti, R.; Brus, L., Electron-hole recombination emission as a probe of surface chemistry in aqueous cadmium sulfide colloids. *J. Phys. Chem.* **1982,** *86* (23), 4470-4472.

37. Kalyanasundaram, K.; Borgarello, E.; Duonghong, D.; Michael Grätzel, Cleavage of Water by Visible-Light Irradiation of Colloidal CdS Solutions; Inhibition of Photocorrosion by RuO. *Angew. Chem. Int. Ed.* **1981,** *20* (11), 987-988.

38. Rossetti, R.; Ellison, J. L.; Gibson, J. M.; Brus, L. E., Size effects in the excited electronic states of small colloidal CdS crystallites. *J. Chem. Phys.* **1984,** *80* (9), 4464-4469.

39. Bawendi, M. G.; Kortan, A. R.; Steigerwald, M. L.; Brus, L. E., X-ray structural characterization of larger CdSe semiconductor clusters. *J. Chem. Phys.* **1989,** *91* (11), 7282-7290.

40. Alivisatos, A. P.; Harris, A. L.; Levinos, N. J.; Steigerwald, M. L.; Brus, L. E., Electronic states of semiconductor clusters: Homogeneous and inhomogeneous broadening of the optical spectrum. *J. Chem. Phys.* **1988,** *89* (7), 4001-4011.

41. Murray, C. B.; Norris, D. J.; Bawendi, M. G., Synthesis and characterization of nearly monodisperse CdE (E = sulfur, selenium, tellurium) semiconductor nanocrystallites. *J. Am. Chem. Soc.* **1993,** *115* (19), 8706-8715.

42. Dabbousi, B. O.; Rodriguez-Viejo, J.; Mikulec, F. V.; Heine, J. R.; Mattoussi, H.; Ober, R.; Jensen, K. F.; Bawendi, M. G., (CdSe)ZnS Core/Shell Quantum Dots: Synthesis and Characterization of a Size Series of Highly Luminescent Nanocrystallites. *J. Phys. Chem. B* **1997,** *101* (46), 9463-9475.

43. Peng, X.; Schlamp, M. C.; Kadavanich, A. V.; Alivisatos, A. P., Epitaxial Growth of Highly Luminescent CdSe/CdS Core/Shell Nanocrystals with Photostability and Electronic Accessibility. *J. Am. Chem. Soc.* **1997,** *119* (30), 7019-7029.

44. Gao, M.; Kirstein, S.; Mohwald, H.; Rogach, A.; Kornowski, A.; Eychmuller, A.; Weller, H., Strongly Photoluminescent CdTe Nanocrystals by Proper Surface Modification. *J. Phys. Chem. B* **1998,** *102* (43), 8360-8363.

45. Klimov, V. I.; McBranch, D. W., Femtosecond 1P-to- 1S Electron Relaxation in Strongly Confined Semiconductor Nanocrystals. *Phys. Rev. Lett.* **1998,** *80* (18), 4028-4031.

46. Klimov, V. I.; McBranch, D. W.; Leatherdale, C. A.; Bawendi, M. G., Electron and hole relaxation pathways in semiconductor quantum dots. *Phys. Rev. B* **1999,** *60* (19), 13740-.

47. Klimov, V. I., Optical Nonlinearities and Ultrafast Carrier Dynamics in Semiconductor Nanocrystals. *J. Phys. Chem. B* **2000,** *104* (26), 6112-6123.

48. Caruge, J. M.; Chan, Y.; Sundar, V.; Eisler, H. J.; Bawendi, M. G., Transient photoluminescence and simultaneous amplified spontaneous emission from multiexciton states in CdSe quantum dots. *Phys. Rev. B* **2004,** *70* (8), 085316.

49. Schaller, R. D.; Agranovich, V. M.; Klimov, V. I., High-efficiency carrier multiplication through direct photogeneration of multi-excitons via virtual single-exciton states. *Nature Physics* **2005,** *1* (3), 189-194.

50. Schaller, R. D.; Petruska, M. A.; Klimov, V. I., Effect of electronic structure on carrier multiplication efficiency: Comparative study of PbSe and CdSe nanocrystals. *Appl. Phys. Lett.* **2005,** *87* (25), 253102.

51. Ellingson, R. J.; Beard, M. C.; Johnson, J. C.; Yu, P.; Micic, O. I.; Nozik, A. J.; Shabaev, A.; Efros, A. L., Highly Efficient Multiple Exciton Generation in Colloidal PbSe and PbS Quantum Dots. *Nano Lett.* **2005,** *5* (5), 865-871.

52. Murphy, J. E.; Beard, M. C.; Norman, A. G.; Ahrenkiel, S. P.; Johnson, J. C.; Yu, P.; Micic, O. I.; Ellingson, R. J.; Nozik, A. J., PbTe Colloidal Nanocrystals: Synthesis, Characterization, and Multiple Exciton Generation. *J. Am. Chem. Soc.* **2006,** *128* (10), 3241-3247.

53. Nair, G.; Geyer, S. M.; Chang, L.-Y.; Bawendi, M. G., Carrier multiplication yields in PbS and PbSe nanocrystals measured by transient photoluminescence. *Phys. Rev. B* **2008,** *78* (12), 125325-10.

54. Wei, G.; Shiu, K.-T.; Giebink, N. C.; Forrest, S. R., Thermodynamic limits of quantum photovoltaic cell efficiency. *Appl. Phys. Lett.* **2007,** *91* (22), 223507-3.

55. Brus, L. E., A simple model for the ionization potential, electron affinity, and aqueous redox potentials of small semiconductor crystallites. *J. Chem. Phys.* **1983,** *79* (11), 5566-5571.

56. Manna, L.; Scher, E. C.; Alivisatos, A. P., Synthesis of Soluble and Processable Rod-, Arrow-, Teardrop-, and Tetrapod-Shaped CdSe Nanocrystals. *J. Am. Chem. Soc.* **2000,** *122* (51), 12700-12706.

57. Peng, X.; Manna, L.; Yang, W.; Wickham, J.; Scher, E.; Kadavanich, A.; Alivisatos, A. P., Shape control of CdSe nanocrystals. *Nature* **2000,** *404* (6773), 59-61.

58. Gur, I.; Fromer, N. A.; Geier, M. L.; Alivisatos, A. P., Air-Stable All-Inorganic Nanocrystal Solar Cells Processed from Solution. *Science* **2005,** *310* (5747), 462-465.

59. Zhao, X. K.; Baral, S.; Rolandi, R.; Fendler, J. H., Semiconductor particles in bilayer lipid membranes. Formation, characterization, and photoelectrochemistry. *J. Am. Chem. Soc.* **1988,** *110* (4), 1012-1024.

60. Johnston, K. W.; Pattantyus-Abraham, A. G.; Clifford, J. P.; Myrskog, S. H.; MacNeil, D. D.; Levina, L.; Sargent, E. H., Schottky-quantum dot photovoltaics for efficient infrared power conversion. *Appl. Phys. Lett.* **2008,** *92* (15), 151115-3.

61. Koleilat, G. I.; Levina, L.; Shukla, H.; Myrskog, S. H.; Hinds, S.; Pattantyus-Abraham, A. G.; Sargent, E. H., Efficient, Stable Infrared Photovoltaics Based on Solution-Cast Colloidal Quantum Dots. *ACS Nano* **2008,** *2* (5), 833-840.

62. Kongkanand, A.; Tvrdy, K.; Takechi, K.; Kuno, M.; Kamat, P. V., Quantum Dot Solar Cells. Tuning Photoresponse through Size and Shape Control of CdSe-TiO2 Architecture. *J. Am. Chem. Soc.* **2008,** *130* (12), 4007-4015.

63. Wang, C.; Shim, M.; Guyot-Sionnest, P., Electrochromic Nanocrystal Quantum Dots. *Science* **2001,** *291* (5512), 2390-2392.

64. Robel, I.; Subramanian, V.; Kuno, M.; Kamat, P. V., Quantum Dot Solar Cells. Harvesting Light Energy with CdSe Nanocrystals Molecularly Linked to Mesoscopic TiO_2 Films. *J. Am. Chem. Soc.* **2006,** *128* (7), 2385-2393.

65. Huynh, W. U.; Dittmer, J. J.; Alivisatos, A. P., Hybrid Nanorod-Polymer Solar Cells. *Science* **2002,** *295* (5564), 2425-2427.

66. Klem, E. J. D.; MacNeil, D. D.; Levina, L.; Sargent, E. H., Solution Processed Photovoltaic Devices with 2% Infrared Monochromatic Power Conversion Efficiency: Performance Optimization and Oxide Formation. *Adv. Mater.* **2008,** *20* (18), 3433-3439.

67. Dooley, C. J.; Dimitrov, S. D.; Fiebig, T., Ultrafast Electron Transfer Dynamics in CdSe/CdTe Donor-Acceptor Nanorods. *J. Phys. Chem. C* **2008,** *112* (32), 12074-12076.

68. Winfree, E.; Liu, F.; Wenzler, L. A.; Seeman, N. C., Design and self-assembly of two-dimensional DNA crystals. *Nature* **1998,** *394* (6693), 539-544.

69. Liu, F.; Sha, R.; Seeman, N. C., Modifying the Surface Features of Two-Dimensional DNA Crystals. *J. Am. Chem. Soc.* **1999,** *121* (5), 917-922.

70. Chan, W. C.; nbsp; W.; Nie, S., Quantum Dot Bioconjugates for Ultrasensitive Nonisotopic Detection. *Science* **1998,** *281* (5385), 2016-2018.

71. Alivisatos, P., The use of nanocrystals in biological detection. *Nature Biotechnology* **2004,** *22* (1), 47-52.

72. Kim, S.; Lim, Y. T.; Soltesz, E. G.; De Grand, A. M.; Lee, J.; Nakayama, A.; Parker, J. A.; Mihaljevic, T.; Laurence, R. G.; Dor, D. M.; Cohn, L. H.; Bawendi, M. G.; Frangioni, J. V., Near-infrared fluorescent type II quantum dots for sentinel lymph node mapping. *Nature Biotechnology* **2004,** *22* (1), 93-97.

73. Dooley, C. J.; Rouge, J.; Ma, N.; Invernale, M.; Kelley, S. O., Nucleotide-stabilized cadmium sulfide nanoparticles. *J. Mater. Chem.* **2007,** *17* (17), 1687-1691.

74. Hinds, S.; Taft, B. J.; Levina, L.; Sukhovatkin, V.; Dooley, C. J.; Roy, M. D.; MacNeil, D. D.; Sargent, E. H.; Kelley, S. O., Nucleotide-Directed Growth of Semiconductor Nanocrystals. *J. Am. Chem. Soc.* **2006,** *128* (1), 64-65.

75. Raytchev, M.; Mayer, E.; Amann, N.; Wagenknecht, H.-A.; Fiebig, T., Ultrafast Proton-Coupled Electron-Transfer Dynamics in Pyrene-Modified Pyrimidine Nucleosides: Model Studies towards an Understanding of Reductive Electron Transport in DNA. *ChemPhysChem* **2004,** *5* (5), 706-712.

76. Raytchev, M.; Pandurski, E.; Buchvarov, I.; Modrakowski, C.; Fiebig, T., Bichromophoric Interactions and Time-Dependent Excited State Mixing in Pyrene Derivatives. A Femtosecond Broad-Band Pump-Probe Study. *J. Phys. Chem. A* **2003,** *107* (23), 4592-4600.

77. Kovalenko, S. A.; Dobryakov, A. L.; Ruthmann, J.; Ernsting, N. P., Femtosecond spectroscopy of condensed phases with chirped supercontinuum probing. *Phys. Rev. A* **1999,** *59* (3), 2369.

78. Ekvall, K.; van der Meulen, P.; Dhollande, C.; Berg, L. E.; Pommeret, S.; Naskrecki, R.; Mialocq, J. C., Cross phase modulation artifact in liquid phase transient absorption spectroscopy. *J. Appl. Phys.* **2000,** *87* (5), 2340-2352.

79. Lorenc, M.; Ziolek, M.; Naskrecki, R.; Karolczak, J.; Kubicki, J.; Maciejewski, A., Artifacts in femtosecond transient absorption spectroscopy. *App. Phys. B* **2002,** *74* (1), 19-27.

80. Alfano, R. R., *The Supercontinuum Laser Source*. Springer: New York, 1989.

81. Alfano, R. R.; Shapiro, S. L., Observation of Self-Phase Modulation and Small-Scale Filaments in Crystals and Glasses. *Phys. Rev. Lett.* **1970,** *24* (11), 592-596.

82. Brodeur, A.; Chin, S. L., Band-gap dependence of the ultrafast white-light continuum. *Phys. Rev. Lett.* **1998,** *80* (20), 4406-4409.

83. Gaeta, A. L., Catastrophic collapse of ultrashort pulses. *Phys. Rev. Lett.* **2000,** *84* (16), 3582-3585.

84. Ward, H.; Berge, L., Temporal shaping of femtosecond solitary pulses in photoionized media. *Phys. Rev. Lett.* **2003,** *90* (5), art. no. 053901.

85. Rothenberg, J. E., Space-Time Focusing - Breakdown of the Slowly Varying Envelope Approximation in the Self-Focusing of Femtosecond Pulses. *Opt. Lett.* **1992,** *17* (19), 1340-1342.

86. Bloembergen, N., The Influence of Electron Plasma Formation on Superbroadening in Light Filaments. *Opt. Commun.* **1973,** *8* (4), 285-288.

87. Buchvarov, I.; Trifonov, A.; Fiebig, T., Toward an understanding of white-light generation in cubic media—polarization properties across the entire spectral range. *Opt. Lett.* **2007,** *32* (11), 1539-1541

88. Raytchev, M. *DNA on the femtosecond, picosecond and nanosecond time scale -- a spectroscopic study*. Boston College, Boston, 2006.

89. Trifonov, A. Advancing and developing experimental methodologies for studying ultrafast photoinduced processes in liquid solutions. Boston College, Boston, 2005.

90. Gunes, S.; Fritz, K. P.; Neugebauer, H.; Sariciftci, N. S.; Kumar, S.; Scholes, G. D., Hybrid solar cells using PbS nanoparticles. *Solar Energy Materials and Solar Cells* **2007,** *91* (5), 420-423.

91. Plass, R.; Pelet, S.; Krueger, J.; Gratzel, M.; Bach, U., Quantum Dot Sensitization of Organic-Inorganic Hybrid Solar Cells. *J. Phys. Chem. B* **2002,** *106* (31), 7578-7580.

92. Cozzoli, P. D.; Pellegrino, T.; Manna, L., Synthesis, properties and perspectives of hybrid nanocrystal structures. *Chem. Soc. Rev.* **2006,** *35* (11), 1195-1208.

93. Zhou, Y.; Li, Y.; Zhong, H.; Hou, J.; Ding, Y.; Yang, C.; Li, Y., Hybrid nanocrystal/polymer solar cells based on tetrapod-shaped CdSexTe1−x nanocrystals. *Nanotechnology* **2006,** (16), 4041.

94. Mayer, A. C.; Scully, S. R.; Hardin, B. E.; Rowell, M. W.; McGehee, M. D., Polymer-based solar cells. *Materials Today* **2007,** *10* (11), 28-33.

95. Coakley, K. M.; McGehee, M. D., Conjugated Polymer Photovoltaic Cells. *Chem. Mater.* **2004,** *16* (23), 4533-4542.

96. Gunes, S.; Neugebauer, H.; Sariciftci, N. S., Conjugated Polymer-Based Organic Solar Cells. *Chem. Rev.* **2007,** *107* (4), 1324-1338.

97. Chou, P.-T.; Chen, C.-Y.; Cheng, C.-T.; Pu, S.-C.; Wu, K.-C.; Cheng, Y.-M.; Lai, C.-W.; Chou, Y.-H.; Chiu, H.-T., Spectroscopy and Femtosecond Dynamics of Type-II CdTe/CdSe Core-Shell Quantum Dots. *ChemPhysChem* **2006,** *7* (1), 222-228.

98. Chen, C.-Y.; Cheng, C.-T.; Yu, J.-K.; Pu, S.-C.; Cheng, Y.-M.; Chou, P.-T.; Chou, Y.-H.; Chiu, H.-T., Spectroscopy and Femtosecond Dynamics of Type-II CdSe/ZnTe Core-Shell Semiconductor Synthesized via the CdO Precursor. *J. Phys. Chem. B* **2004,** *108* (30), 10687-10691.

99. Wargnier, R.; Baranov, A. V.; Maslov, V. G.; Stsiapura, V.; Artemyev, M.; Pluot, M.; Sukhanova, A.; Nabiev, I., Energy Transfer in Aqueous Solutions of Oppositely Charged CdSe/ZnS Core/Shell Quantum Dots and in Quantum Dot-Nanogold Assemblies. *Nano Lett.* **2004,** *4* (3), 451-457.

100. Rogach, A. L.; Franzl, T.; Klar, T. A.; Feldmann, J.; Gaponik, N.; Lesnyak, V.; Shavel, A.; Eychmuller, A.; Rakovich, Y. P.; Donegan, J. F., Aqueous Synthesis of Thiol-Capped CdTe Nanocrystals: State-of-the-Art. *J. Phys. Chem. C* **2007,** *111* (40), 14628-14637.

101. Guo, J.; Yang, W.; Wang, C., Systematic Study of the Photoluminescence Dependence of Thiol-Capped CdTe Nanocrystals on the Reaction Conditions. *J. Phys. Chem. B* **2005,** *109* (37), 17467-17473.

102. Gross, D.; Susha, A. S.; Klar, T. A.; Da Como, E.; Rogach, A. L.; Feldmann, J., Charge Separation in Type II Tunneling Structures of Close-packed CdTe and CdSe Nanocrystals. *Nano Lett.* **2008,** *8* (5), 1482-1485.

103. Koole, R.; Liljeroth, P.; deMelloDonega, C.; Vanmaekelbergh, D.; Meijerink, A., Electronic Coupling and Exciton Energy Transfer in CdTe Quantum-Dot Molecules. *J. Am. Chem. Soc.* **2006,** *128* (32), 10436-10441.

104. Cameron, P. J.; Zhong, X.; Knoll, W., Monitoring the Covalent Binding of Quantum Dots to Functionalized Gold Surfaces by Surface Plasmon Resonance Spectroscopy. *J. Phys. Chem. C* **2007,** *111* (28), 10313-10319.

105. Talapin, D. V.; Nelson, J. H.; Shevchenko, E. V.; Aloni, S.; Sadtler, B.; Alivisatos, A. P., Seeded Growth of Highly Luminescent CdSe/CdS Nanoheterostructures with Rod and Tetrapod Morphologies. *Nano Lett.* **2007,** *7* (10), 2951-2959.

106. Milliron, D. J.; Hughes, S. M.; Cui, Y.; Manna, L.; Li, J.; Wang, L.-W.; Paul Alivisatos, A., Colloidal nanocrystal heterostructures with linear and branched topology. *Nature* **2004,** *430* (6996), 190-195.

107. Peng, Z. A.; Peng, X., Formation of High-Quality CdTe, CdSe, and CdS Nanocrystals Using CdO as Precursor. *J. Am. Chem. Soc.* **2001,** *123* (1), 183-184.

108. Nandivada, H.; Jiang, X.; Lahann, J., Click Chemistry: Versatility and Control in the Hands of Materials Scientists. *Adv. Mater.* **2007,** *19* (17), 2197-2208.

109. Jean-FranÁois Lutz, 1,3-Dipolar Cycloadditions of Azides and Alkynes: A Universal Ligation Tool in Polymer and Materials Science. *Angew. Chem. Int. Ed.* **2007,** *46* (7), 1018-1025.

110. Gian Cesare Tron, T. P., Richard A. Billington, Pier Luigi Canonico, Giovanni Sorba, Armando A. Genazzani,, Click chemistry reactions in medicinal chemistry: Applications of the 1,3-dipolar cycloaddition between azides and alkynes. *Medicinal Research Reviews* **2008,** *28* (2), 278-308.

111. Lutz, J.-F.; Bˆrner, H. G., Modern trends in polymer bioconjugates design. *Progress in Polymer Science* **2008,** *33* (1), 1-39.

112. Weisbrod, S. H.; Marx, A., Novel strategies for the site-specific covalent labelling of nucleic acids. *Chem. Comm.* **2008,** (44), 5675-5685.

113. Binder, W. H.; Sachsenhofer, R., lsquoClickrsquo Chemistry in Polymer and Material Science: An Update. *Macromolecular Rapid Communications* **2008,** *29* (12-13), 952-981.

114. Morten Meldal, Polymer "Clicking" by CuAAC Reactions. *Macromolecular Rapid Communications* **2008,** *29* (12-13), 1016-1051.

115. Binder, W. H.; Sachsenhofer, R.; Straif, C. J.; Zirbs, R., Surface-modified nanoparticles via thermal and Cu(I)-mediated "click" chemistry: Generation of luminescent CdSe nanoparticles with polar ligands guiding supramolecular recognition. *J. Mater. Chem.* **2007,** *17* (20), 2125-2132.

116. Voggu, R.; Suguna, P.; Chandrasekaran, S.; Rao, C. N. R., Assembling covalently linked nanocrystals and nanotubes through click chemistry. *Chem. Phys. Lett.* **2007,** *443* (1-3), 118-121.

117. Kumar, S.; Jones, M.; Lo, S.; Scholes, G., Nanorod Heterostructures Showing Photoinduced Charge Separation. *Small* **2007,** *3* (9), 1633-1639.

118. Halpert, J. E.; Porter, V. J.; Zimmer, J. P.; Bawendi, M. G., Synthesis of CdSe/CdTe Nanobarbells. *J. Am. Chem. Soc.* **2006,** *128* (39), 12590-12591.

119. Jones, M.; Kumar, S.; Lo, S. S.; Scholes, G. D., Exciton Trapping and Recombination in Type II CdSe/CdTe Nanorod Heterostructures. *J. Phys. Chem. C* **2008,** *112* (14), 5423-5431.

120. Peng, P.; Milliron, D. J.; Hughes, S. M.; Johnson, J. C.; Alivisatos, A. P.; Saykally, R. J., Femtosecond Spectroscopy of Carrier Relaxation Dynamics in Type II CdSe/CdTe Tetrapod Heteronanostructures. *Nano Lett.* **2005,** *5* (9), 1809-1813.

121. Braun, M.; Link, S.; Burda, C.; El-Sayed, M., Determination of the localization times of electrons and holes in the HgS well in a CdS/HgS/CdS quantum dot-quantum well nanoparticle. *Phys. Rev. B* **2002,** *66* (20), 205312-.

122. Yu, P.; Nedeljkovic, J. M.; Ahrenkiel, P. A.; Ellingson, R. J.; Nozik, A. J., Size Dependent Femtosecond Electron Cooling Dynamics in CdSe Quantum Rods. *Nano Lett.* **2004,** *4* (6), 1089-1092.

123. Xu, S.; Mikhailovsky, A. A.; Hollingsworth, J. A.; Klimov, V. I., Hole intraband relaxation in strongly confined quantum dots: Revisiting the "phonon bottleneck" problem. *Phys. Rev. B* **2002,** *65* (4), 045319-.

124. Hunsche, S.; Dekorsy, T.; Klimov, V.; Kurz, H., Ultrafast dynamics of carrier-induced absorption changes in highly-excited CdSe nanocrystals. *App. Phys. B* **1996,** *62* (1), 3-10.

125. Yu, W. W.; Qu, L.; Guo, W.; Peng, X., Experimental Determination of the Extinction Coefficient of CdTe, CdSe, and CdS Nanocrystals. *Chem. Mater.* **2003,** *15* (14), 2854-2860.

126. Anderson, N. A.; Lian, T., Ultrafast electron injection from metal polypyridyl complexes to metal-oxide nanocrystalline thin films. *Coord. Chem. Rev.* **2004,** *248* (13-14), 1231-1246.

127. Anderson, N. A.; Lian, T., ULTRAFAST ELECTRON TRANSFER AT THE MOLECULE-SEMICONDUCTOR NANOPARTICLE INTERFACE. *Ann. Rev. Phys. Chem.* **2005,** *56* (1), 491-519.

128. Asbury, J. B.; Anderson, N. A.; Hao, E.; Ai, X.; Lian, T., Parameters Affecting Electron Injection Dynamics from Ruthenium Dyes to Titanium Dioxide Nanocrystalline Thin Film. *J. Phys. Chem. B* **2003,** *107* (30), 7376-7386.

129. Jaskólski, W.; Bryant, G. W., Multiband theory of quantum-dot quantum wells: Dim excitons, bright excitons, and charge separation in heteronanostructures. *Phys. Rev. B* **1998,** *57* (8), R4237.

130. Scholes, G. D.; Jones, M.; Kumar, S., Energetics of Photoinduced Electron-Transfer Reactions Decided by Quantum Confinement. *J. Phys. Chem. C* **2007,** *111* (37), 13777-13785.

131. Marcus, R. A., Relation between charge transfer absorption and fluorescence spectra and the inverted region. *J. Phys. Chem.* **1989,** *93* (8), 3078-3086.

132. Mataga, N.; Chosrowjan, H.; Shibata, Y.; Yoshida, N.; Osuka, A.; Kikuzawa, T.; Okada, T., First Unequivocal Observation of the Whole Bell-Shaped Energy Gap Law in Intramolecular Charge Separation from S2 Excited State of Directly Linked Porphyrin-Imide Dyads and Its Solvent-Polarity Dependencies. *J. Am. Chem. Soc.* **2001,** *123* (49), 12422-12423.

133. Mataga, N.; Taniguchi, S.; Chosrowjan, H.; Osuka, A.; Kurotobi, K., Observations of the whole bell-shaped energy gap law in the intra-molecular charge separation (CS) from S_2 state of directly linked Zn-porphyrin-imide dyads: Examinations of wider range of energy gap ($-\Delta G_{CS}$) for the CS rates in normal regions. *Chem. Phys. Lett.* **2005,** *403* (1-3), 163-168.

134. Dimitrov, S. D.; Dooley, C. J.; Trifonov, A. A.; Fiebig, T., Femtosecond Probing of Optical Phonon Dynamics in Quantum-Confined CdTe Nanocrystals. *J. Phys. Chem. C* **2009,** *113* (10), 4198-4201.

135. Ellis, A. B.; Kaiser, S. W.; Wrighton, M. S., Optical to electrical energy conversion. Characterization of cadmium sulfide and cadmium selenide based photoelectrochemical cells. *J. Am. Chem. Soc.* **1976,** *98* (22), 6855-6866.

136. Gerischer, H., Electrochemical photo and solar cells principles and some experiments. *Journal of Electroanalytical Chemistry* **1975,** *58* (1), 263-274.

137. Istrate, E.; Hoogland, S.; Sukhovatkin, V.; Levina, L.; Myrskog, S.; Smith, P. W. E.; Sargent, E. H., Carrier Relaxation Dynamics in Lead Sulfide Colloidal Quantum Dots. *J. Phys. Chem. B* **2008,** *112* (10), 2757-2760.

138. Roberts, M. Electrochemical and spectroscopic studies of biomolecular complexes. Boston College, Chestnut Hill, 2008.

139. Sulfur powder was made into a stable colloidal mixture in high pH aqueous solution with agitation over 60 minutes. The yellow powder yielded a bright yellow solution in the otherwise clear KOH/Na2S mixture.

140. Special thanks needs to be given for the efforts of Dr. Dunwei Wang's group in helping me to perform these measurements allowing me the use of their potentiostat

141. Hossain, Z.; Huq, F., Studies on the interaction between Cd2+ ions and DNA. *J. Inorg. Biochem.* **2002,** *90* (3-4), 85-96.

142. Hossain, Z.; Huq, F., Studies on the interaction between Cd2+ ions and nucleobases and nucleotides. *J. Inorg. Biochem.* **2002,** *90* (3-4), 97-105.

143. Huq, F.; Peter, M. C. R., Interaction between NiCl2, and nucleobases, nucleosides and nucleotides. *J. Inorg. Biochem.* **2000,** *78* (3), 217-226.

144. Ma, N.; Dooley, C. J.; Kelley, S. O., RNA-Templated Semiconductor Nanocrystals. *J. Am. Chem. Soc.* **2006,** *128* (39), 12598-12599.

145. Green, M.; Taylor, R.; Wakefield, G., The synthesis of luminescent adenosine triphosphate passivated cadmium sulfide nanoparticles. *J. Mater. Chem.* **2003,** *13* (8), 1859-1861.

146. Green, M.; Smyth-Boyle, D.; Harries, J.; Taylor, R., Nucleotide passivated cadmium sulfide quantum dots. *Chem. Comm.* **2005,** (38), 4830-4832.

147. Jursenas, S.; Stepankevieius, V.; Strumskis, M.; Zukauskas, A., Carrier recombination in CdS nanocrystals under single-electron and high-density excitation. *Semiconductor Science and Technology* **1995,** *10* (3), 302-309.

148. Levina, L.; Sukhovatkin, V.; Musikhin, S.; Cauchi, S.; R. Nisman; Bazett-Jones, D. P.; Sargent, E. H., Efficient Infrared-Emitting PbS Quantum Dots Grown on DNA and Stable in Aqueous Solution and Blood Plasma. *Adv. Mater.* **2005,** *17* (15), 1854-1857.

149. Arakawa, H.; Ahmad, R.; Naoui, M.; Tajmir-Riahi, H.-A., A Comparative Study of Calf Thymus DNA Binding to Cr(III) and Cr(VI) Ions. EVIDENCE FOR THE GUANINE N-7-CHROMIUM-PHOSPHATE CHELATE FORMATION. *J. Biol. Chem.* **2000,** *275* (14), 10150-10153.

150. Spanhel, L.; Haase, M.; Weller, H.; Henglein, A., Photochemistry of colloidal semiconductors. 20. Surface modification and stability of strong luminescing CdS particles. *J. Am. Chem. Soc.* **1987,** *109* (19), 5649-5655.

151. Mahtab, R.; Rogers, J. P.; Murphy, C. J., Protein-Sized Quantum Dot Luminescence Can Distinguish between "Straight", "Bent", and "Kinked" Oligonucleotides. *J. Am. Chem. Soc.* **1995,** *117* (35), 9099-9100.

152. Energy Information Administration *Annual Energy Review 2007*; U.S. Department of Energy: Washington, DC, June 23, 2008.

153. Energy Information Administration *International Energy Annual 2006*; US Department of Energy: Washington, DC, 2008; p Table E.1.

154. Hoffert, M. I.; Caldeira, K.; Jain, A. K.; Haites, E. F.; Harvey, L. D. D.; Potter, S. D.; Schlesinger, M. E.; Schneider, S. H.; Watts, R. G.; Wigley, T. M. L.; Wuebbles, D. J., Energy implications of future stabilization of atmospheric CO2 content. *Nature* **1998,** *395* (6705), 881-884.

155. Kates, R., Population and consumption: What we know, what we need to know. *Environment* **2000,** *42*, 10-19.

156. This is done by writing each term as the future value term calculated by continuous growth at the described rates. That is, FV = PV*exp(n*rate) where n is the number of years to project to, FV is the future value and PV is the present valu.

157. U.S. Census Bureau International Data Base (IDB). http://www.census.gov/ipc/www/idb/.

158. U.S. Department of Agriculture International Macroeconomic Data Set 2008. http://www.ers.usda.gov/Data/Macroeconomics/.

159. Energy Information Administration *Annual Energy Outlook 2008*; US Department of Energy: Washington, DC, 2008.

160. Energy Information Administration *International Energy Outlook 2008*; US Department of Energy: Washington, DC, 2008; p Table E.1.

161. Archer, C. L.; Jacobson, M. Z., Evaluation of global wind power. *Journal of Geophysical Research* **2005,** *110*, D12110.

162. United Nations Development Program *World Energy Assessment Report: Energy and the Challenge of Sustainability*; United Nations: New York, 2003.

163. United Nations Development Program *World Energy Assessment Overview: 2004 Update*; United Nations: New York, 2004.

164. Intergovernmental Panel on Climate Change *Climate Change 2007, Synthesis Report Summary for Policymakers*; Intergovernmental Panel on Climate Change: Washington, DC, Forth Assessment Report, 2007.

165. Petit, J. R.; Jouzel, J.; Raynaud, D.; Barkov, N. I.; Barnola, J. M.; Basile, I.; Bender, M.; Chappellaz, J.; Davis, M.; Delaygue, G.; Delmotte, M.; Kotlyakov, V. M.; Legrand, M.; Lipenkov, V. Y.; Lorius, C.; Pepin, L.; Ritz, C.; Saltzman, E.; Stievenard, M., Climate and atmospheric history of the past 420,000 years from the Vostok ice core, Antarctica. *Nature* **1999,** *399* (6735), 429-436.

166. Siegenthaler, U.; Stocker, T. F.; Monnin, E.; Luthi, D.; Schwander, J.; Stauffer, B.; Raynaud, D.; Barnola, J.-M.; Fischer, H.; Masson-Delmotte, V.; Jouzel, J., Stable Carbon Cycle-Climate Relationship During the Late Pleistocene. *Science* **2005,** *310* (5752), 1313-1317.

167. President's Council of Advisors on Science and Technology *The Energy Imperative; Technology and the Role of Emerging Companies*; Executive Office of the President of the United States: 2006.

168. Goldemberg, J., Ethanol for a Sustainable Energy Future. *Science* **2007,** *315* (5813), 808-810.

169. Himmel, M. E.; Ding, S.-Y.; Johnson, D. K.; Adney, W. S.; Nimlos, M. R.; Brady, J. W.; Foust, T. D., Biomass Recalcitrance: Engineering Plants and Enzymes for Biofuels Production. *Science* **2007,** *315* (5813), 804-807.

170. United Nations Development Program, *World Energy Assessment: Energy and the Challenge of Sustainability*. 1 ed.; New York, 2000.